INVESTIGATION OF THE ELASTIC PROPERTIES OF $Rb_4LiH_3(SO_4)_4$ AS A FUNCTION OF TEMPERATURE AND PRESSURE

WENLONG WU

Investigation of the Elastic Properties of $Rb_4LiH_3(SO_4)_4$ as a Function of Temperature and Pressure

by

© WenLong Wu
B.Sc. (1988) Shandong Normal University

A thesis submitted to the
School of Graduate Studies
in partial fulfillment of the
requirements for the degree of
Master of Science.

Department of Physics and Physical Oceanography
Memorial University of Newfoundland

August 6, 2004

ST. JOHN'S NEWFOUNDLAND

Your file Votre référence
ISBN: 0-494-02392-9
Our file Notre référence
ISBN: 0-494-02392-9

Contents

Abstract

A high resolution acoustic interferometer is used to study the elastic properties of $Rb_4LiH_3(SO_4)_4$ as a function of temperature and pressure. The temperature and pressure ranges in our investigation were 4 K-300 K and 0 $kbar$-10 $kbar$, respectively. At ambient pressure, a phase transition at $T_c = 132 \pm 0.3$ K is observed using the sound velocity measurements as a function of temperature. At room temperature, the occurrence of a phase transition at a pressure of $P_c = 8.4 \pm 0.2$ $kbar$ is discovered through sound velocity measurements as a function of pressure. Attempt has also been made to distinguish the x and y direction in the monoclinic phase. The results turn out to be still equivalent along these two directions. Using the sound velocity measurements as a function of temperature under different pressures, the temperature-pressure phase diagram of $Rb_4LiH_3(SO_4)_4$ is derived. It is found that T_c increases rapidly with pressure at a rate of $19 \pm 1 K/kbar$. Using the sound velocity measurements, the temperature and pressure dependence of five of the seven independent elastic constants of $Rb_4LiH_3(SO_4)_4$ are obtained. To our knowledge, we are the first to investigate the elastic constants as a function of pressure. We observed that the elastic constant $(C_{11} - C_{12})/2$ shows incomplete softening at T_c or P_c. In the high symmetry phase, this elastic constant exhibits a nonlinear temperature or pressure dependence. A Landau model involving both temperature and pressure as external parameters is proposed. Our calculations agree well with our experimental results.

Our model predicts that the actual soft acoustic mode shows complete softening at T_c. It also predicts that the actual soft acoustic mode propagates along the direction away [110] by -5^0.

Acknowledgements

It is a pleasure to acknowledge my deepest appreciation and gratitude to my supervisor, Dr. Guy Quirion, for his guidance, patience and stimulating discussions throughout the course of this work. I would like to express my thanks to Dr. S. Curnoe, Dr. J. Lagowski and Dr. J. C. Lewis for their teaching and encouragement. I also acknowledge Mr. M. Clouter for offering me $Rb_4LiH_3(SO_4)_4$ crystals. I extend my thanks to other faculty members for their advice. I would like to thank Dr. I. A. Sergienko for the discussions in group theory. I am grateful to Fred Perry for the assistance in dealing with software problems. I would like to thank Bill Kieley from the machine shop for his service. I also thank Wayne Holly and Roger Guest for their services in supplying liquid helium and liquid nitrogen. I would like to thank Marek Bromberek and Mahmoud Abu-Kharma for their help in programming. I also thank Iram Munawar for the helpful discussions about Landau theory. I would also like to thank other graduate students for their help in my study and research. I am deeply appreciative of the financial support from the School of Graduate Studies at Memorial University of Newfoundland, the Physics department, and my supervisor.

I wish to thank my wife for her understanding and spiritual support during my stay in Canada. I also thank my parents for their support and guidance. I dedicate this thesis to my family.

List of Tables

List of Figures

Chapter 1

Introduction

Over the last few decades, due to their interesting physical properties and application potentials, ferroelastic crystals have been the subject of numerous theoretical and experimental studies. According to Aizu [1], ferroelastics has been defined as materials in which homogeneous stress may be used to order and switch the orientation of structural domains. Thus, ferroelastic crystals are analog to ferroelectric crystals where, in that case, the electric domains can be aligned by the application of a homogeneous electric field. While all ferroelectric crystals are known to be also ferroelastic, ferroelastic compounds are not necessarily ferroelectric at the same time [2]. Thus, the central physical feature of ferroelastic crystals is their lattice distortion associated with the occurrence of spontaneous strain in the ferroelastic phase. Moreover, when a stress is applied, hysteretic behavior of the macroscopic spontaneous strain is observed. This strain-stress hysteresis is one of the characteristics of ferroelastic crystals.

The properties of the ferroelastic materials have been exploited in many applications. As the domains in a ferroelastic can be made to shrink or expand by applying an uniaxial stress, single-domain crystal can be obtained as required by some appli-

cations, e.g. in nonlinear optics [59]. By applying uniaxial stress, one can also pole or switch the domain of a ferroelastic single crystal. This property has been used for creating periodically spaced domain walls in some ferroelastic crystals, and the spacing of the walls can be from 70 mirons to 0.5 micron [3]. The result is a tunable optical grating. The switchability of ferroelastic domains and the consequent mobility of the domain walls have additional applications [4]. Micropositioner with a memory, variable acoustic delay line, tailered domain patterns for resonator applications and focusing acoustic transducers, are some examples of potential applications. Near the phase transition, ferroelastic crystals also exhibit some interesting properties. For example, in the vicinity of the transition temperature a small stress can be used to induce a large strain which result in a large variation in the birefringence property of the crystal. This property has found application in acoustic-optic modulators [59]. Since for ferroelastic crystals, one of the acoustic velocity typically tends to zero as the transition temperature is approached, the modulation efficiency, which is inverse proportional to the acoustic velocity, is considerably high. The feature that some elastic constants show a strong temperature dependence near the transition temperature has been used in smart structures (materials or structures with the ability to respond in a pre-designed manner to changing environmental conditions) [59].

Although the existence of crystals with the stoichiometry $A_4LiH_3(BO_4)_4$, where $A = Rb,\ NH_4,\ K$ and $B = S,\ Se$, was reported more than a hundred years ago, their ferroelastic properties have been discovered only recently. That aroused the interest of scientists and consequently a large number of studies followed. However, till now, these investigations are focused on the understanding of the structure and properties of these crystals. The application of these crystals cannot be reasonably predicted until their properties are known. From the reported results, we know that at room temperature almost all these crystals are isomorphous and possessed the

tetragonal symmetry [5–7]. However, there was a disagreement about the actual symmetry group to which they should be ascribed. For $K_4LiH_3(SO_4)_4$, Electron Spin Resonance (ESR) investigations [8] led to the conclusion that the point group $4/m$ is the most likely. However, for $Rb_4LiH_3(SO_4)_4$ the inverted torsional pendulum and piezoelectric series resonance studies [9] and the Brillouin scattering studies [10] suggested that the prototype symmetry should be the point group $4mm$. Later investigations [6, 7, 11–16] finally reached a consensus and showed that this class of compounds has a room-temperature phase corresponding to the tetragonal point group 4. Moreover, at low temperatures most of these crystals undergo a structural phase transition from the tetragonal point group 4 to the monoclinic point group 2. In spite of their structure similarity, the transitions they undergo below room temperature usually show different features. For example, while the Brillouin scattering study [14] of $Rb_4LiH_3(SO_4)_4$ indicates that the transition at about 130 K is ferroelastic, the ferroelastic nature of the transition at 115 K in $K_4LiH_3(SO_4)_4$ was not confirmed [14]. Though both compounds $Rb_4LiH_3(SO_4)_4$ and $(NH)_4LiH_3(SO_4)_4$ undergo ferroelastic phase transitions, the temperature behavior of the soft elastic constants are believed to be different [6]. While the effective elastic constant for the soft mode in $(NH)_4LiH_3(SO_4)_4$ vanishes at T_c [16]. The soft mode in $Rb_4LiH_3(SO_4)_4$ shows incomplete softening at T_c [14]. To our knowledge, $Rb_4LiH_3(SO_4)_4$ is the only ferroelastic compound whose soft mode shows incomplete softening at T_c. Because of the unusual elastic properties displayed by $Rb_4LiH_3(SO_4)_4$, we choose this particular ferroelastic compound as our research object.

Despite the large number of investigations realized on $Rb_4LiH_3(SO_4)_4$, our knowledge about some of its properties is far from complete. The compound $Rb_4LiH_3(SO_4)_4$ was initially assumed to have the chemical formula corresponding to $LiRb_5(SO_4)_2 \cdot 1.5\ H_2SO_4$ [9, 10, 12, 17, 18]. However, the density value calculated

from X-ray data using this formula disagreed with the measured value [14]. The following chemical analyses led to its present form for which a better fit was obtained. So far four structural phase transitions have been observed for this crystal in the temperature range going from 4 K to 495 K. Piskunowicz et al. [19] reported that three structural transitions happened at 440, 454, and 470 K, respectively. These three phase transitions were later confirmed by Differential Thermal Analysis (DTA) study [20], however the observed transition temperatures (458 K, 470 K, and 490 K) are somewhat different from those reported by Piskunowicz et al [19].

Comparatively, the phase transition below room temperature is well studied, the transition temperature was found to be around 132 K [6, 10, 15, 17–19, 21]. Besides, it was already well established that the transition belongs to the second order (continuous transition). In conformity with this, neither latent heat nor thermal hysteresis has been observed in the transition [9, 10, 18, 19]. The ferroelastic character for this crystal is also known. In the low temperature phase, two kinds of birefringent domains has been observed by using a polarization microscope [9]. The domains are separated by mutually perpendicular walls in the planes (100) and (010). Such 90^0 domain structure was later confirmed by the observations conducted by Piskunowicz et al. [19] and Mielcarek et al. [22]. Moreover, the strain-stress hysteresis was also observed by applying normal stress along [100] or [010] directions [9, 18]. Given these facts, the phase below room temperature is undoubtedly ferroelastic. Since it was also found that the direction of the spontaneous electric polarization remain unchanged around 132 K [18], the transition is ferroelastic and non-ferroelectric.

In determining the symmetry of this crystal at room temperature, results obtained from different techniques used to be inconsistent. Brillouin scattering measurements [10, 17] suggested that the phase transition type is $4mm \rightarrow mm2$. This conclusion was corroborated by inverted torsional pendulum and piezoelectric series resonance

measurements [9] and the observations of domain walls [18]. However, the X-ray investigation [23] showed that $Rb_4LiH_3(SO_4)_4$ possesses the symmetry of space groups $P4_1$ or $P4_3$ at room temperature. The X-ray anomalous scattering and optical-activity measurements [11] further point out that $Rb_4LiH_3(SO_4)_4$ is consisted of 87% of laevorotatory crystal in space group $P4_1$ and 13% of dextrorotatory crystal in the space group $P4_3$. However, recent neutron scattering measurements [6] only confirmed the existence of space group $P4_1$ at room temperature. Despite the uncertainty about the existence of $P4_3$, given that the two space groups both possess the same point group symmetry, it is safe to say that the crystal belongs to the tetragonal point group 4 at room temperature. This assignment of the point group for the prototype phase was supported by ultrasonic velocity and dielectric permittivity measurements [12] and Brillouin scattering [14] and Raman scattering studies [15]. For such a prototype symmetry, the ferroelastic transition theory [24] requires that the low-temperature ordered phase to be monoclinic 2. However, direct evidences about the structure of the low-temperature phase are scarce and inconsistent. On the one hand, X-ray studies [23] suggested the presence of orthorhombic distortion in the low temperature phase. On the other hand, X-ray investigations reported by Zuniga et al. [11] show that the low temperature phase should belong to monoclinic space group $P2_1$ and point group 2. Very recent results, from neutron scattering measurements [6], support the conclusion of the latter group.

A ferroelastic phase transition is usually accompanied by the onset of spontaneous strains which in turn lead to anomalous temperature behavior on the elastic properties. Such variations have been observed in $Rb_4LiH_3(SO_4)_4$ by various types of experiments, however, the results are not fully consistent. For example, during a ferroelastic phase transition with a symmetry change $4 \rightarrow 2$, one expects to see the softening of the elastic constant C_{11} - C_{12} and C_{66}. However, in the inverted torsional

pendulum measurements, the appearance of a soft mode associated with the elastic constants C_{11} - C_{12} is observed [9]. According to the Brillouin scattering studies [10], only the elastic constant C_{66} gets softened while ultrasonic studies [12] show that both $C_{11} - C_{12}$ and C_{66} get softened. Despite this disagreement, there is a common feature that emerges, they all indicate incomplete softening.

So far several Landau theory models have been put forward by different research groups, however none of them can describe the overall elastic properties of $Rb_4LiH_3(SO_4)_4$. These models can be divided into two classes. One assumes that the spontaneous strain (or strains) is the order parameter of the Landau free energy, i.e. assuming that the transition corresponds to a proper ferroelastic transition [12, 14, 19]. The other assumes that the order parameter is not the strain but has the same symmetry as the spontaneous strain (or strains) [10, 21]. In this case, the transition is classified as a pseudo-proper ferroelastic transition. Though the proposed models agree qualitatively with some of the observations, their predictions are still not fully consistent with the measurements.

The aim of this project is to investigate the elastic properties of $Rb_4LiH_3(SO_4)_4$ as a function of both temperature and pressure, in the meantime, to verify if the softening of the effective elastic constant associated with the soft mode is indeed incomplete. This is realized via sound velocity measurements using an acoustic interferometer. These measurements also enable us to derive the temperature-pressure diagram of $Rb_4LiH_3(SO_4)_4$. The diagram covers the temperature range 4 K-300 K for pressures up to 7 $kbar$. Attempt has also been made to distinguish the x and y direction in the monoclinic phase. The result will reveal some properties of the domains which appear in this phase. In order to explain the experimental features, we also present a Landau model using both temperature and pressure as the external parameters. This model is based on the assumption that the observed ferroelastic phase transition has a

pseudoproper character. The validity of this model is verified using our experimental data. Unexpectedly, it predicts that the effective elastic constant associated with the soft mode shows complete softening at the transition.

The acoustic interferometer used in this project is very suitable for the investigation of the elastic properties of crystals. The advantage of this technique lies in its high resolution ($1ppm$), two or three order of magnitude greater than that of Brillouin scattering (its resolution is in the order of 1%). Consequently, our technique can detect small variation in sound velocity and, in some cases, discover phase transitions that have been missed by other techniques. Another advantage should be attributed to its versatility. With the same experimental set up, we can measure the sound velocity as a function of both temperature and pressure. However, the samples used in our measurements normally need to be larger in size than those used in X-ray scattering or Brillouin scattering. In this particular case, this requirement should not be considered as a disadvantage since large single crystals of $Rb_4LiH_3(SO_4)_4$ can be easily obtained.

Chapter 2

Crystalline Elasticity

As the aim of this project is to investigate the elastic properties of $Rb_4LiH_3(SO_4)_4$, we first introduce some essential background knowledge about crystalline properties, such as, the strain, stress and elastic constant tensors. Then we will discuss how the elastic energy can be obtained. Finally, we describe how the Christoffel equation is used in order to determine the relation between the velocity of some specific plane waves and the independent elastic constants of the crystal. A detailed discussion about the elastic properties of crystals can be found in the book "*Elastic Waves in Solids*" written by E. Dieulesaint and D. Royer [60].

2.1 Static Elasticity

2.1.1 Strain and Stress

Under the action of external forces, materials are generally deformed to some extent. Before discussing deformations in general, we first consider a simple case, the stretching of a string (one dimensional), see Fig. 2.1. Under the action of a force F, the string stretches. The section between M_0 and N_0 extends from the original length

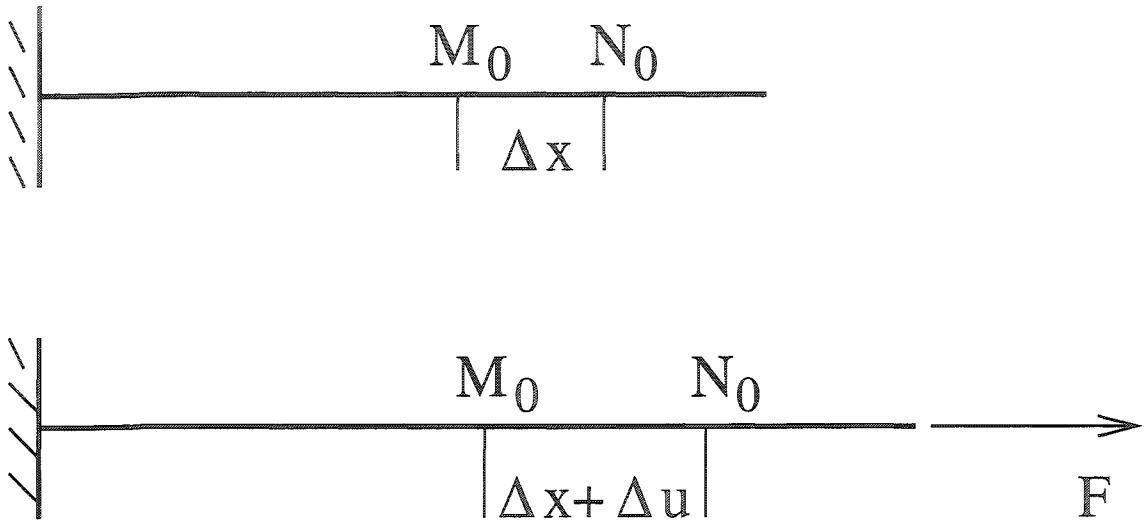

Figure 2.1: Deformation of a string. Under the action of a force F, the length increment for the portion Δx is Δu. The strain is described as the limit of the ratio $\Delta u/\Delta x$ when Δx goes to 0 [60].

Δx to $\Delta x + \Delta u$. The deformation of this section is then Δu and the deformation per unit length can be written as

$$e = \frac{\Delta u}{\Delta x} \tag{2.1}$$

which represents the strain. In the case of a two dimensional body, the deformations induced by external forces do not necessarily involve only the variations in length but also some angular distortions, as shown in Fig. 2.2. The variations in length along x-axis and y-axis are represented by the quantities e_{xx} (or e_{11}) and e_{yy} (or e_{22}), respectively, while the angular distortions or shear deformations are represented by the quantities e_{xy} (or e_{12}) and e_{yx} (or e_{21}). These four quantities constitute a 2×2 second-rank tensor, which is often expressed in the form of a matrix. Due to similar considerations, the deformations of a three dimensional body induced by external forces are described by a 3×3 strain tensor. Its nine elements can be arranged in a

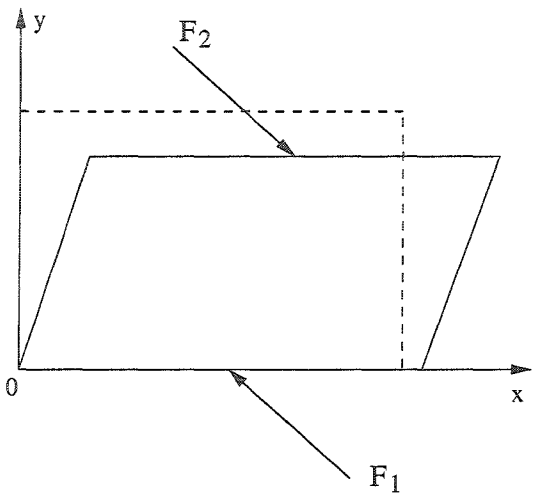

Figure 2.2: The deformations of a two dimensional body under the action of forces F_1 and F_2. Under the action of F_1 and F_2, the lengths along both x-axis and y-axis change, so did the angle between two points of the body with respect to the origin 0.

3×3 matrix as following

$$(e_{ij}) = \begin{pmatrix} e_{11} & e_{12} & e_{13} \\ e_{21} & e_{22} & e_{23} \\ e_{31} & e_{32} & e_{33} \end{pmatrix} \tag{2.2}$$

where (e_{ij}) represents the strain tensor with i, j running from 1 to 3. Its diagonal components are a measurement of the extensions along the three axes of an orthogonal reference frame associated with the crystal axes. The off-diagonal components describe the shear deformations of the medium. For small deformations, which are considered here, the strain components can be expressed as [60]

$$e_{ij} = \frac{1}{2}\left[\frac{\partial u_i}{\partial x_j} + \frac{\partial u_j}{\partial x_i}\right] \tag{2.3}$$

where e_{ij} is the component of the strain tensor in the i-th row and j-th column and u_i (u_j) is the i-th (j-th) component of the displacement $\vec{u}$ of the point where the

deformation is observed. From Eq. 2.3, we see that the element of the strain tensor remains invariant under the interchange of indices i and j, i.e.

$$e_{ij} = e_{ji} \tag{2.4}$$

In other words, for small deformations the strain tensor is symmetric and can be rewritten as

$$(e_{ij}) = \begin{pmatrix} e_{11} & e_{12} & e_{13} \\ e_{12} & e_{22} & e_{23} \\ e_{13} & e_{23} & e_{33} \end{pmatrix} \tag{2.5}$$

where the number of independent strain components reduces to 6.

The force acting on a unit area in the solid is defined as the stress. There are nine stress components T_{11}, T_{12}, T_{13}, T_{21}, T_{22}, T_{23}, T_{31}, T_{32}, T_{33}. The nine components form a second-rank tensor called the stress tensor (T_{ij}), where $i, j = 1, 2, 3$. The component T_{ij} represents a force applied in the i direction acting on a unit area normal to the j-axis. The number of independent stress components is reduced from nine to six based on the following considerations. Let's consider an elementary cube which remains in static equilibrium under the action of stress T_{ij}, see Fig. 2.3. The force applied to the upper face in the x-direction corresponds to the stress component T_{xy} or T_{12}. As required by the equilibrium condition, the force applied to the bottom in the negative x-direction must also be T_{12} since the magnitude of these two forces are equal. Similarly, the forces applied to the right and left faces of the cube in the y-direction correspond to T_{21}. As the cube is in static equilibrium, the condition that the total torque must be zero requires that $T_{12} = T_{21}$. Generalizing this result, we have that

$$T_{ij} = T_{ji} \tag{2.6}$$

and, as for the strain tensor, the stress tensor is also symmetric.

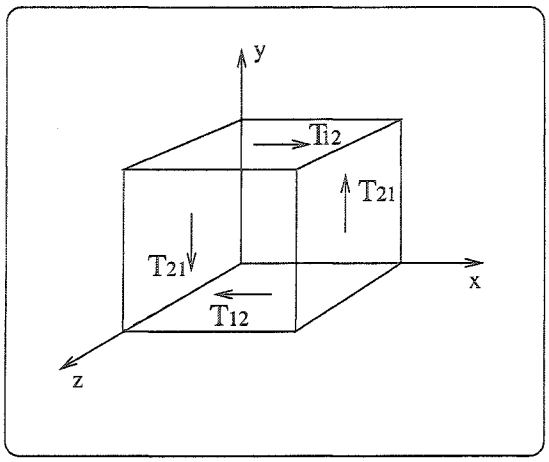

Figure 2.3: For a body in equilibrium, the net force acting on that body must vanish. The total torque acting on that body must also vanish, so that $T_{12} = T_{21}$ [61].

2.1.2 Elastic Constants

A medium is said to be elastic, if it returns to its initial state after the external forces are removed. In an elastic material, for sufficiently small deformations, the strain is directly proportional to the stress. In this linear limit, the relation between stress T and strain e is adequately described by the generalized Hooke's law:

$$T_{ij} = C_{ijkl} \cdot e_{kl} \qquad i,\ j,\ k,\ l = 1,\ 2,\ 3 \tag{2.7}$$

where repeated indices are implicitly summed over (Einstein convention), so that the coefficients C_{ijkl} represent the components of a fourth-rank tensor called elastic stiffness tensor. As each index in C_{ijkl} runs from 1 to 3, the elastic stiffness tensor has 81 components. However, as the stress tensor and the strain tensor are both symmetric, the elastic constants must have the properties

$$C_{ijkl} = C_{jikl}; \qquad C_{ijkl} = C_{ijlk}\ . \tag{2.8}$$

Based on these symmetry properties, the elastic stiffness tensor has a maximum of 36 independent components instead of 81. Using Eq. 2.3, these symmetries also allow

us to express Hooke's law Eq. 2.7 in terms of the displacements:

$$T_{ij} = C_{ijkl} \frac{\partial u_l}{\partial x_k} \tag{2.9}$$

The symmetry properties Eq. 2.8 also enable us to label the independent elastic moduli of the elastic stiffness tensor by only two indices. In the standard Voigt notation, the correpondence shown here is used:

$$\begin{aligned} (11) &\leftrightarrow 1 & (22) &\leftrightarrow 2 & (33) &\leftrightarrow 3 \\ (23) = (32) &\leftrightarrow 4 & (31) = (13) &\leftrightarrow 5 & (12) = (21) &\leftrightarrow 6\,. \end{aligned} \tag{2.10}$$

So that the 36 independent constants can be arranged in a 6×6 matrix,

$$C_{\alpha\beta} = C_{ijkl} \tag{2.11}$$

with $\alpha \leftrightarrow (ij)$, $\beta \leftrightarrow (kl)$, where α and β range from 1 to 6. This so-called matrix notation can be extended to the stress and strain tensors. The 6×6 elastic constant matrix is symmetric based on the following thermodynamic consideration. From the first law of thermodynamics, we know that the internal energy variation per unit volume is

$$dU = \delta W + \delta Q \tag{2.12}$$

where δQ is the heat received per volume and δW is the work done to that volume. However, during a change in strain de_{ik}, the work done by the external forces can be expressed as

$$\delta W = T_{ik}\, de_{ik} \tag{2.13}$$

and for a reversible transformation, the second law of thermodynamics tell us

$$\delta Q = T\, dS \tag{2.14}$$

where T is the absolute temperature and S the entropy. Therefore,

$$dU = T_{ik}\ de_{ik} + T\ dS \tag{2.15}$$

and

$$T_{ik} = \left(\frac{\partial U}{\partial e_{ik}}\right)_S . \tag{2.16}$$

From the Hooke's law Eq. 2.7, we also know that

$$C_{ijkl} = \left(\frac{\partial T_{ij}}{\partial e_{kl}}\right); \qquad C_{klij} = \left(\frac{\partial T_{kl}}{\partial e_{ij}}\right) . \tag{2.17}$$

Inserting 2.16 into them, we obtain

$$C_{ijkl} = \left(\frac{\partial^2 U}{\partial e_{ij}\ \partial e_{kl}}\right)_S = C_{klij} \tag{2.18}$$

or

$$C_{\alpha\beta} = C_{\beta\alpha} . \tag{2.19}$$

The above property reduces the number of independent elastic constants to 21, as shown hereunder.

$$C_{\alpha\beta} = \begin{pmatrix} C_{11} & C_{12} & C_{13} & C_{14} & C_{15} & C_{16} \\ C_{12} & C_{22} & C_{23} & C_{24} & C_{25} & C_{26} \\ C_{13} & C_{23} & C_{33} & C_{34} & C_{35} & C_{36} \\ C_{14} & C_{24} & C_{34} & C_{44} & C_{45} & C_{46} \\ C_{15} & C_{25} & C_{35} & C_{45} & C_{55} & C_{56} \\ C_{16} & C_{26} & C_{36} & C_{46} & C_{56} & C_{66} \end{pmatrix} \tag{2.20}$$

This elastic constant tensor corresponds to the triclinic symmetry wherein the only symmetry operation is the identity operation.

For crystals of higher symmetry, this number may be reduced further using their symmetry properties which require that some elastic constants must be zero or equal

to each other. Under symmetry operations, the atoms in the crystal recover its original configuration and, therefore all its physical properties should remain unchanged including the elastic stiffness tensor associated with that crystal. However, as these symmetry operations are equivalent to a series of transformations of the reference frame, they will result in the transformation of the elastic tensor of the crystal. Before we discuss the transformation property of a fourth-rank tensor, let's first consider a simple case, the transformation of a first-rank tensor or vector. Taking the position vector $\mathbf{r}$ for example, under a rotation of the Cartesian reference frame, the three components of $\mathbf{r}$ (x_1, x_2, x_3) are transformed as

$$\begin{pmatrix} x_1' \\ x_2' \\ x_3' \end{pmatrix} = \begin{pmatrix} \alpha_1^1 & \alpha_1^2 & \alpha_1^3 \\ \alpha_2^1 & \alpha_2^2 & \alpha_2^3 \\ \alpha_3^1 & \alpha_3^2 & \alpha_3^3 \end{pmatrix} \begin{pmatrix} x_1 \\ y_2 \\ z_3 \end{pmatrix} \tag{2.21}$$

where x_1', x_2', x_3' are the three components of $\mathbf{r}$ in the new frame, and the transformation matrix is called the α matrix. Using Einstein convention, the above transformation can be rewritten as

$$x_i' = \alpha_i^j \; x_j \; . \tag{2.22}$$

Other vectors, such as the velocity, obey the same transformation rule. Accordingly, a second-rank tensor obey the transformation rule of

$$T_{ij}' = \alpha_i^p \; \alpha_j^q \; T_{pq} \; . \tag{2.23}$$

and a fourth-rank tensor, such as the elastic moduli tensor, should transform under a change of the orthonormal reference frame according to

$$C_{ijkl} = \alpha_i^p \; \alpha_j^q \; \alpha_k^r \; \alpha_l^s \; C_{pqrs} \tag{2.24}$$

where $\alpha_i^p, \alpha_j^q, \alpha_k^r, \alpha_l^s$ are components of the transformation matrix of the frame. If the transformation corresponds to a symmetry operation, the invariance condition

requires that $C_{ijkl} = C_{pqrs}$, i.e.

$$C_{ijkl} = \alpha_i^p \; \alpha_j^q \; \alpha_k^r \; \alpha_l^s \; C_{ijkl} \; . \tag{2.25}$$

Thus all the elastic moduli vanish unless $\alpha_i^i \; \alpha_j^j \; \alpha_k^k \; \alpha_l^l = 1$. Taking the crystal $Rb_4LiH_3(SO_4)_4$ for example, its low symmetry phase belongs to monoclinic point group 2. Relative to the triclinic crystals, it possesses an additional symmetry, i.e. invariant under a 180^0 rotation around the z-axis. Given that the α matrix for this symmetry operation is

$$\alpha = \pm \begin{pmatrix} -1 & 0 & 0 \\ 0 & -1 & 0 \\ 0 & 0 & 1 \end{pmatrix} \tag{2.26}$$

the invariance condition implies that all components of the elastic stiffness tensor with odd number of index 3 (for which $\alpha_i^i \; \alpha_j^j \; \alpha_k^k \; \alpha_l^l = -1$) vanish. Therefore, the elastic moduli with indices 1113, 2213, 3313, 1312, 1123, 2223, 3323 and 2312, or those with subscripts of 15, 25, 35, 56, 14, 24, 34 and 46 in the Voigt notation (see relation 2.10) must be zero. Therefore, only 13 independent elastic constants are left for the monoclinic crystals:

$$C_{\alpha\beta} = \begin{pmatrix} C_{11} & C_{12} & C_{13} & 0 & 0 & C_{16} \\ C_{12} & C_{22} & C_{23} & 0 & 0 & C_{26} \\ C_{13} & C_{23} & C_{33} & 0 & 0 & C_{36} \\ 0 & 0 & 0 & C_{44} & C_{45} & 0 \\ 0 & 0 & 0 & C_{45} & C_{55} & 0 \\ C_{16} & C_{26} & C_{36} & 0 & 0 & C_{66} \end{pmatrix} \tag{2.27}$$

In the high symmetry phase, the crystal $Rb_4LiH_3(SO_4)_4$ has the symmetry of tetragonal point group 4. In addition to the symmetry of monoclinic point group 2, it acquires new symmetry, a 4-fold rotation symmetry around the z-axis (which is taken

along the c-axis of the crystal). Relative to the tensor of the monoclinic phase, the 4-fold symmetry, which is represented by the element C_4^1 (rotating 90^0 around z-axis), further reduces the number of independent elastic constants. Applying C_4^1 (counter clockwise), the coordinates transform as

$$\begin{pmatrix} x \\ y \\ z \end{pmatrix} \rightarrow \begin{pmatrix} y \\ -x \\ z \end{pmatrix} \tag{2.28}$$

hence the elastic constants transform as

$$C_{22} = C_{2222} \rightarrow C_{1111} = C_{11} \tag{2.29}$$

$$C_{23} = C_{2233} \rightarrow C_{1133} = C_{13} \tag{2.30}$$

$$C_{55} = C_{1313} \rightarrow C_{2323} = C_{44} \tag{2.31}$$

$$C_{26} = C_{2212} \rightarrow -C_{1121} = -C_{16} \tag{2.32}$$

$$C_{36} = C_{3312} \rightarrow -C_{3321} = -C_{36} = 0\ . \tag{2.33}$$

$$\tag{2.34}$$

As a result, the independent elastic constants for the tetragonal phase are reduced to 7, as shown below

$$C_{\alpha\beta} = \begin{pmatrix} C_{11} & C_{12} & C_{13} & 0 & 0 & C_{16} \\ C_{12} & C_{11} & C_{13} & 0 & 0 & -C_{16} \\ C_{13} & C_{13} & C_{33} & 0 & 0 & 0 \\ 0 & 0 & 0 & C_{44} & 0 & 0 \\ 0 & 0 & 0 & 0 & C_{44} & 0 \\ C_{16} & -C_{16} & 0 & 0 & 0 & C_{66} \end{pmatrix} . \tag{2.35}$$

2.1.3 Elastic Energy

The energy provided by the external forces during the deformation is stored in the medium as elastic energy. In the approximation of the Hooke's law (recall the expression for the energy of a stretched spring), this energy can be written as

$$U = \frac{1}{2}\, C_{\alpha\beta}\, e_\alpha\, e_\beta \tag{2.36}$$

where the indices α, β range from 1 to 6. The energy U is called the elastic potential energy, it stands for the internal energy variation per unit volume. Using Eq. 2.36, the elastic energy for the tetragonal phase of $Rb_4LiH_3(SO_4)_4$ is found to be

$$\begin{aligned} F(e_i) &= \tfrac{1}{2}\, C_{11}\, (e_1^2 + e_2^2) + \tfrac{1}{2}\, C_{44}\, (e_4^2 + e_5^2) + \tfrac{1}{2}\, C_{33}\, e_3^2 + \tfrac{1}{2}\, C_{66}\, e_6^2 \\ &+ C_{12}\, e_1\, e_2 + C_{13}\, (e_1 + e_2)\, e_3 + C_{16}\, (e_1 - e_2)\, e_6 \end{aligned} \tag{2.37}$$

which will be referred to in chapter 5.

2.2 Plane Wave Propagation

Unlike liquids, solids can sustain shear deformations and, therefore can transmit both longitudinal and transverse waves. Moreover, in an anisotropic medium, such as a crystal, normally three different waves can propagate in a given direction. However, in most cases, none of these waves is purely longitudinal or transverse. Consequently, the three waves one observed in a given direction are often referred as quasi-longitudinal, fast quasi-transverse and slow quasi-transverse wave. The polarizations of these three waves are always mutually orthogonal.

The properties of the three waves come from the equation of motion which is the result of Newton's second law and the Hooke's law. The force density of stressed material is [60]

$$f_i = \frac{\partial T_{ij}}{\partial x_j} \tag{2.38}$$

which gives rise to the acceleration $\partial^2 u_i/\partial t^2$ for the unit volume mass ρ, where u_i is the i-th component of the displacement $\vec{u}$. According to Newton's second law, the equation of motion for an elastic medium can be written as

$$\rho \frac{\partial^2 u_i}{\partial t^2} = \frac{\partial T_{ij}}{\partial x_j} . \tag{2.39}$$

Making use of Eq. 2.9, the equation of motion becomes

$$\rho \frac{\partial^2 u_i}{\partial t^2} = C_{ijkl} \frac{\partial^2 u_l}{\partial x_j \partial x_k} \tag{2.40}$$

which represents a set of wave equations for which the plane wave function

$$u_i = u_{0i} \, e^{i(\mathbf{k}\cdot\mathbf{r}-\omega t)} \qquad i = 1, \ 2, \ 3 \tag{2.41}$$

is a proper solution. Here, $\mathbf{k}$ represents the wave vector, ω is the frequency, and u_{0i} is the wave polarization (i.e. the particle displacement direction). Inserting Eq. 2.41 into Eq. 2.40 and putting $u_{0i} = \delta_{il} \, u_{0l}$, we obtain

$$(\rho \, \omega^2 \, \delta_{il} - C_{ijkl} \, k_j \, k_k) \, u_{0l} = 0 \tag{2.42}$$

Dividing Eq. 2.42 by k^2, it takes the form

$$(\rho \, v^2 \, \delta_{il} - C_{ijkl} \, n_j \, n_k) \, u_{0l} = 0 \tag{2.43}$$

where $v = \omega/k$ is the phase velocity, and n_j, n_k are the cosine direction of $\mathbf{k}$ with respect to the axes of x, y, z. The equation above is the well-known Christoffel equation. After introducing a second rank tensor

$$\Gamma_{il} = \ C_{ijkl} \, n_j \, n_k \tag{2.44}$$

the Christoffel equation becomes

$$(\Gamma_{il} - \rho \, v^2 \, \delta_{il}) \, u_{0l} = 0 \, . \tag{2.45}$$

This shows that the polarization u_{0l} is an eigenvector of the propagation tensor Γ_{il} with eigenvalue ρv^2. Therefore, for a given propagation direction, the velocities of the waves can be found by solving the secular equation:

$$\left|\Gamma_{il} - \rho v^2 \delta_{il}\right| = 0 \ . \tag{2.46}$$

It will generally give three different velocities which correspond to the three waves propagating in this direction. As the elements of the Γ_{il} tensor contain the elastic constants, the wave velocities are thus related to the independent elastic constants of the crystal. The polarization for each wave can be determined by searching for the eigenvector of the propagation tensor using Eq. 2.45. For convenience, the propagation directions are usually chosen to be along the crystallograghical axes or its bisectors so that the Christoffel equation can be easily solved. For illustration, let consider waves propagating along the z direction. In this case, the cosine directions are $n_1 = 0$, $n_2 = 0$, $n_3 = 1$ and the propagation tensor Γ_{il} can be written as $\Gamma_{il} = C_{i33l}$, or

$$\Gamma_{il} = \begin{pmatrix} C_{55} & C_{45} & C_{35} \\ C_{45} & C_{44} & C_{34} \\ C_{35} & C_{34} & C_{33} \end{pmatrix} \tag{2.47}$$

For most crystals, this tensor can be further simplified. Taking the tetragonal phase of $Rb_4LiH_3(SO_4)_4$ for example, we know that $C_{35} = C_{34} = C_{45} = 0$ and $C_{44} = C_{55}$. Therefore,

$$\Gamma_{il} = \begin{pmatrix} C_{44} & 0 & 0 \\ 0 & C_{44} & 0 \\ 0 & 0 & C_{33} \end{pmatrix} \tag{2.48}$$

As the matrix of the tensor Γ_{il} is already diagonalized, finding the eigenvalues is

straightforward

$$\lambda_1 = C_{33}, \qquad \lambda_2 = \lambda_3 = C_{44} \tag{2.49}$$

As the eigenvalue of the propagation tensor is equal to ρv^2, the velocities for the three waves propagating in this direction can be expressed in terms of the elastic constants as

$$v_1 = \sqrt{\frac{C_{33}}{\rho}} \qquad v_2 = v_3 = \sqrt{\frac{C_{44}}{\rho}} \tag{2.50}$$

Substituting λ_1, λ_2, λ_3 into Eq. 2.45, their corresponding eigenvectors (or the polarizations) are found to be

$$u_1 \rightarrow (0,\ 0,\ 1) \quad u_2 \rightarrow (0,\ 1,\ 0) \quad u_3 \rightarrow (1,\ 0,\ 0) \tag{2.51}$$

where the eigenvectors have been normalized. It is easy to see that the polarization $u_1 \rightarrow (0,\ 0,\ 1)$ of the first wave is parallel to the wave vector (the z-direction) and, therefore belongs to the longitudinal mode. The polarizations of the other two waves are perpendicular to the wave vector and, consequently belong to the transverse modes. The velocities and modes of the sound waves propagating along [100], [010] and [110] for both phases of $Rb_4LiH_3(SO_4)_4$ can be determined in the same way and the results are given in Table 2.1. For clarity, the long expressions for ρv^2 corresponding to the modes $L[110]$ and $T_y[110]$ in the monoclinic phase are left out, where L and T represent longitudinal and transverse, while the subscripts represent the direction of polarization for a direction of propagation given in the bracket. As shown in Table 2.1, the elastic constants can be obtained from measuring velocities along different crystal directions. We also see that, in order to get the independent elastic constants for the tetragonal phase, we need to measure the modes $L[100]$, $T_y[100]$, $T_z[100]$, $L[001]$, $L[110]$, $T_{[\bar{1}10]}[110]$.

Direction	Mode	tetragonal	monoclinic
..	L	$\frac{1}{2}\left(C_{11}+C_{66}+\sqrt{(C_{11}-C_{66})^2+4C_{16}^2}\right)$	$\frac{1}{2}\left(C_{11}+C_{66}+\sqrt{(C_{11}-C_{66})^2+4C_{16}^2}\right)$
[100]	T_y	$\frac{1}{2}\left(C_{11}+C_{66}-\sqrt{(C_{11}-C_{66})^2+4C_{16}^2}\right)$	$\frac{1}{2}\left(C_{11}+C_{66}-\sqrt{(C_{11}-C_{66})^2+4C_{16}^2}\right)$
..	T_z	C_{44}	C_{55}
..	L	$\frac{1}{2}\left(C_{11}+C_{66}+\sqrt{(C_{11}-C_{66})^2+4C_{16}^2}\right)$	$\frac{1}{2}\left(C_{22}+C_{66}-\sqrt{(C_{22}-C_{66})^2+4C_{26}^2}\right)$
[010]	T_x	$\frac{1}{2}\left(C_{11}+C_{66}-\sqrt{(C_{11}-C_{66})^2+4C_{16}^2}\right)$	$\frac{1}{2}\left(C_{22}+C_{66}+\sqrt{(C_{22}-C_{66})^2+4C_{26}^2}\right)$
..	T_z	C_{44}	C_{44}
..	L	C_{33}	C_{33}
[001]	T_x	C_{44}	$\frac{1}{2}\left(C_{44}+C_{55}+\sqrt{(C_{44}-C_{55})^2+4C_{45}^2}\right)$
..	T_y	C_{44}	$\frac{1}{2}\left(C_{44}+C_{55}-\sqrt{(C_{44}-C_{55})^2+4C_{45}^2}\right)$
..	L	$\frac{1}{2}\left(C_{11}+C_{66}+\sqrt{(C_{12}+C_{66})^2+4C_{16}^2}\right)$	..
[110]	$T_{[\bar{1}10]}$	$\frac{1}{2}\left(C_{11}+C_{66}-\sqrt{(C_{12}+C_{66})^2+4C_{16}^2}\right)$	..
..	T_z	C_{44}	$\frac{1}{2}(C_{44}+2C_{45}+C_{55})$

Table 2.1: The ρv^2 as a function of the elastic constants in the tetragonal (4) and monoclinic (2) phases, where L is longitudinal, T_j is transverse wave with polarization along the j-direction. For clarity, long expressions for the modes L and $T_{[\bar{1}10]}$ along [110] are omitted.

Chapter 3

Experimental Setup

Acoustic measurements play an important role in the investigation of the elastic properties of crystals. One of the most useful techniques is the pulse echo method. In this chapter, we will describe how the ultrasonic velocity can be measured using the standard pulse echo method. However, this method does not always have sufficient sensitivity to detect changes in the sound velocity close to a phase transition. Thus, we will also present how it is possible to achieve resolution as high as a few parts per million using an experimental technique called acoustic interferometer. Moreover, as one of the goals of this project is to study the pressure effect on the elastic properties of $Rb_4LiH_3(SO_4)_4$, the procedure of applying and measuring the pressure will also be presented here.

3.1 Crystal Structure of $Rb_4LiH_3(SO_4)_4$

The $Rb_4LiH_3(SO_4)_4$ crystals were grown in the Crystal Physics Laboratory of Adam Mickiewicz University, Poland [14]. Their chemical composition was determined by atomic spectroscopy (Li^+, Rb^+) and chemical analysis (SO_4^{2-}) [21]. The structure

consists of tetrahedral sulphate groups arranged together with Rb atoms on layers stacked perpendicularly to the c-tetragonal axis. The four Rb atoms and SO_4 groups are distributed on two consecutive layers. The Li atoms are intercalated every two layers and are surrounded by tetrahedra of O atoms [11]. At room temperature the crystals belong to space group $P4_1$ of the tetragonal system. The unit cell contains four layers of $Rb_4LiH_3(SO_4)_4$ molecules, see Fig. 3.1. After rotating 90^0 around the axis and moving up $\frac{1}{4}c$, the crystal recovers its original configuration. In the low temperature phase, the second- and the fourth-layer molecules are slightly displaced from their tetragonal position. The symmetry operation becomes a 180^0 rotation followed by a $\frac{1}{2}c$ translation along the axis. That means that the crystal possesses the symmetry of space group $P2_1$. The lattice parameters, determined by X-ray measurements [11], correspond to $a = 7.615\ (2)\ \mathring{A}$, $c = 29.458\ (6)\ \mathring{A}$ with a density of 2.81 g/cm^3.

3.2 Sound Velocity Measurements

As stated previously, the independent elastic constants of a material can be derived from sound velocity measurements. However, in order to obtain all the independent elastic constants, these measurements must be realized along some specific directions for different acoustic modes. For crystals $Rb_4LiH_3(SO_4)_4$, we need to perform these measurements at least along [100], [001], [110] and [011] directions. Thus, a series of samples with parallel faces perpendicular to the crystallographic axes and the bisectors of these axes were prepared. The samples used in our measurements were cut from large colorless and transparent single crystals. In order to get a good signal, two opposite faces of the sample were polished using silicon carbide to the degree that they became smooth and parallel to each other. After all these operations, the

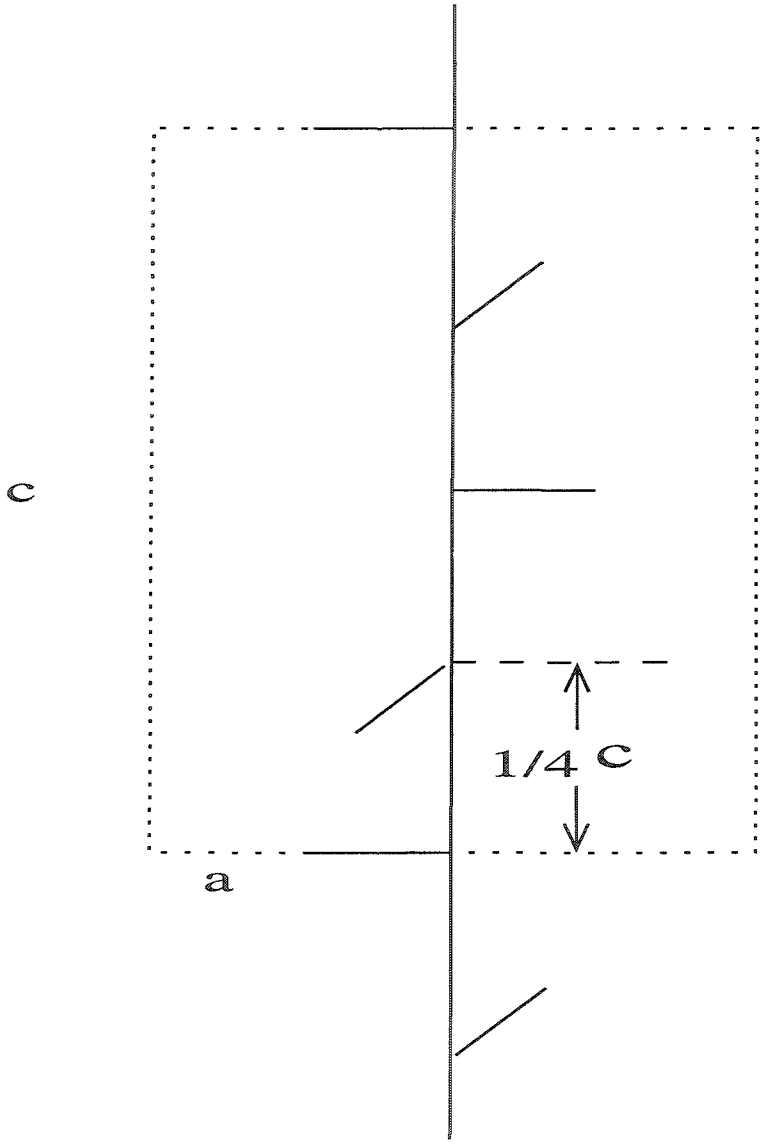

Figure 3.1: An illustration of the symmetry of $Rb_4LiH_3(SO_4)_4$ at room temperature. Here the horizontal bars represent the $Rb_4LiH_3(SO_4)_4$ molecules. The vertical line represents the screw axis. The parallelogram represents the unit cell.

sample dimensions were approximately $5mm \times 5mm \times 3mm$. The orientations of the samples has been checked using polarized light. Since $Rb_4LiH_3(SO_4)_4$ is a birefringence crystal with optic axis along c-axis, the polarization of a linearly polarized light will normally be modified after the light passes through this crystal. When this crystal is put between two polarizers with their transmission axes rotated 90^0, as the crystal is rotated around its z-axis, no significant variation in the intensity of the transmitted light is observed. However, if the crystal is rotated around the x-axis (or y-axis), a large change in the intensity of the transmitted light is observed every time the crystal is rotated by 90^0. This method was used for all samples to confirm their orientations.

The sound velocity can be measured using the standard pulse-echo method, as illustrated in Fig. 3.2. The tiny device bonded on the top surface of the sample is a transducer which consists essentially of a thin piezoelectric crystal and two electrodes. As an oscillating electrical field is applied to the electrodes, the transducer mechanically vibrates at the same frequency due to the piezoelectric effect. Thus, in this standard approach, a pulsed radio frequency signal induces an ultrasonic pulse in the crystal, and subsequently the ultrasonic pulse travels back and forth between the crystal's extremities owing to reflection at the boundaries. Each time that the sound wave returns to the transducer, a small fraction of its mechanical energy is converted into electrical signal (inverse piezoelectric effect). If the acoustic attenuation is not too large, this process will repeat several times, and a multi-echo pattern can be observed on an oscilloscope, as depicted in Fig. 3.2. In this reflection configuration, the time Δt for a round trip can be determined by measuring the time between two consecutive echoes. Since the length L of the sample along which the wave is propagating is normally measured before mounting the transducer, the calculation of the

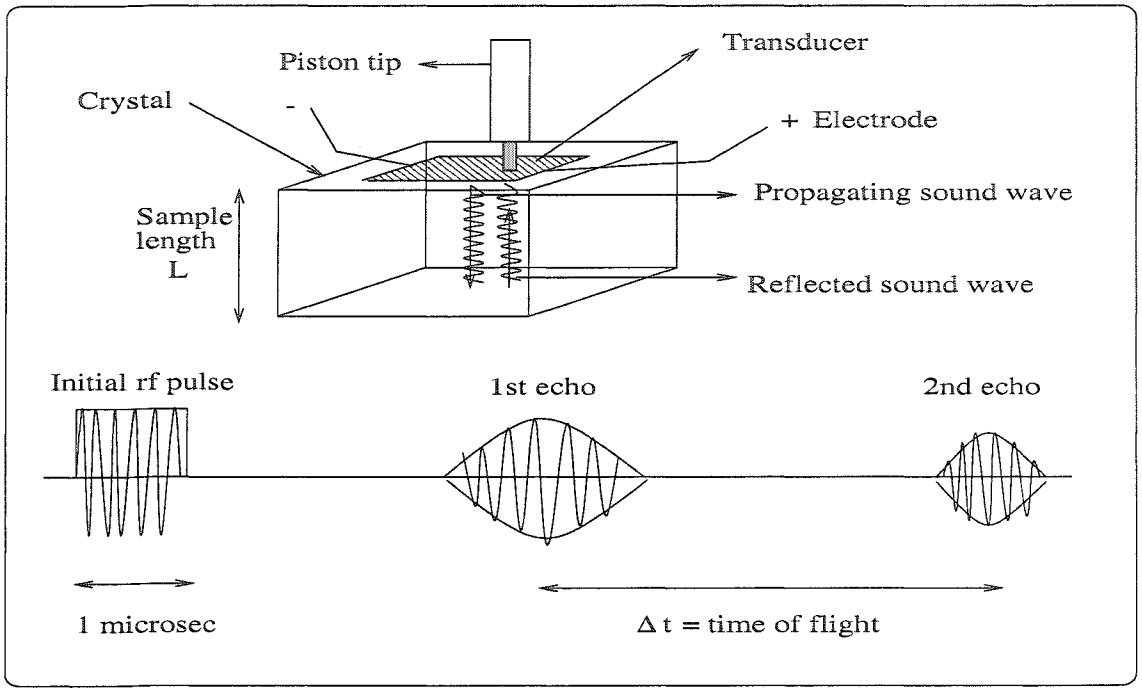

Figure 3.2: A pulsed rf signal is sent to the transducer. Several electrical pulses come out. The reflection configuration and consecutive echoes are shown here. Here the piston tip is used to produce a gentle force on the transducer due to a small compressed spring, also shown in Fig. 3.6.

velocity is then given by

$$v = \frac{2L}{\Delta t} . \tag{3.1}$$

The typical length of samples used in these experiments is between 3 mm and 5 mm which gives a time of flight between $1\mu s$ and $3\mu s$. Considering that the uncertainties on the sample's length and the time of flight are $0.01mm$ and $0.01\mu s$, respectively, the resolution for the absolute velocity determination is normally around 0.5%. Thus, the standard pulse-method does not always have sufficient sensitivity to detect changes in the sound velocity close to a phase transition. In principle, the resolution can be improved by increasing the length of the crystal. But this method is limited by the finite space of the sample holder and the acoustic attenuation of the crystal. Even with this improvement, the resolution would still be in the order of 0.05%. So we need a new approach with higher resolution. We will see in the next section how it is possible to improve the resolution to a few parts per million by using a device called acoustic interferometer.

3.3 The Acoustic Interferometer

An acoustic interferometer can achieve a resolution as high as a few part per million by measuring the relative change in velocity $\Delta v/v$ instead of the absolute velocity. As shown in Fig.3.3, a continuous radio frequency signal, generated by a RF Synthesizer (6061*A Synthesized RF Generator*), is divided into two parts by a power splitter. The first part is used as the reference signal, the second part is sent to a gate (Gate 1) which cuts the signal into short pulses of about $1\mu s$ at a repetition rate of 1000 pulses per second. These electrical pulses arrive at the transducer after passing through a circulator. The main purpose of the circulator is to prevent any reflected signal from entering the synthesizer. As described in section 3.2, the transducer converts the elec-

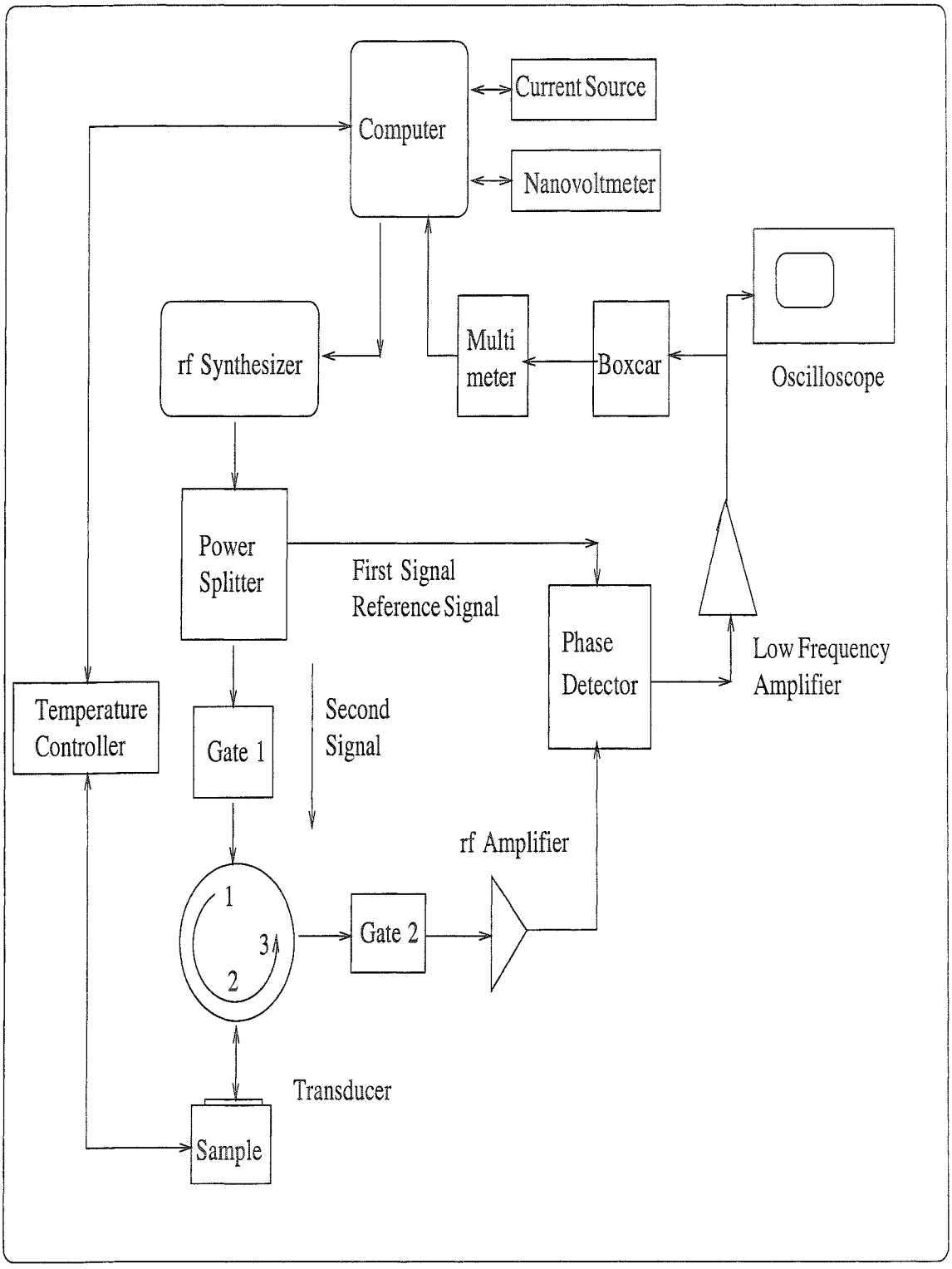

Figure 3.3: Block diagram of the acoustic interferometer.

trical pulse into mechanical vibrations and consequently produces an ultrasonic wave in the crystal. The sound wave gets reflected at each extremity of the crystal. Each time it reaches the transducer, a small portion of its mechanical energy is converted into electrical signal. Then this electrical multi-echo signal enters the circulator at position 2 and comes out at position 3. Before being amplified, the initial pulse is cut off from the echo pattern by a second gate (Gate 2) in order to prevent saturation of the low noise rf amplifier. The phase differences between the reference signal and the reflected signal are then compared using a phase detector, which gives a signal proportional to the phase difference. A typical multi-echo pattern one observes on the oscilloscope is shown in Fig. 3.4. In this particular case, we can see that the first, the third and the fourth echo are in phase, and that the second echo is out of phase. This figure also shows that the amplitude of the echo decreases with the time of flight. This is a result of the acoustic attenuation as the wave propagates in the crystal. The amplitude of one of these echoes (usually the first one) is measured using the boxcar, which is in fact measuring the phase difference between the reference signal and the echo. For the n-th echo, the phase difference Φ_n is

$$\Phi_n = 2\pi f \Delta t_n \tag{3.2}$$

where f is the frequency of the sound wave, i.e. the frequency of the electrical signal and Δt_n is the time of flight of the n-th echo. As the distance travelled by the n-th echo is $2nL$ (L is the length of the sample), Δt_n can be expressed as

$$\Delta t_n = \frac{2nL}{v} \, . \tag{3.3}$$

Combining the last expression with equation 3.2, we obtain an expression for the relative phase of the n-th echo which is given by

$$\Phi_n = \frac{4\pi nLf}{v} \, . \tag{3.4}$$

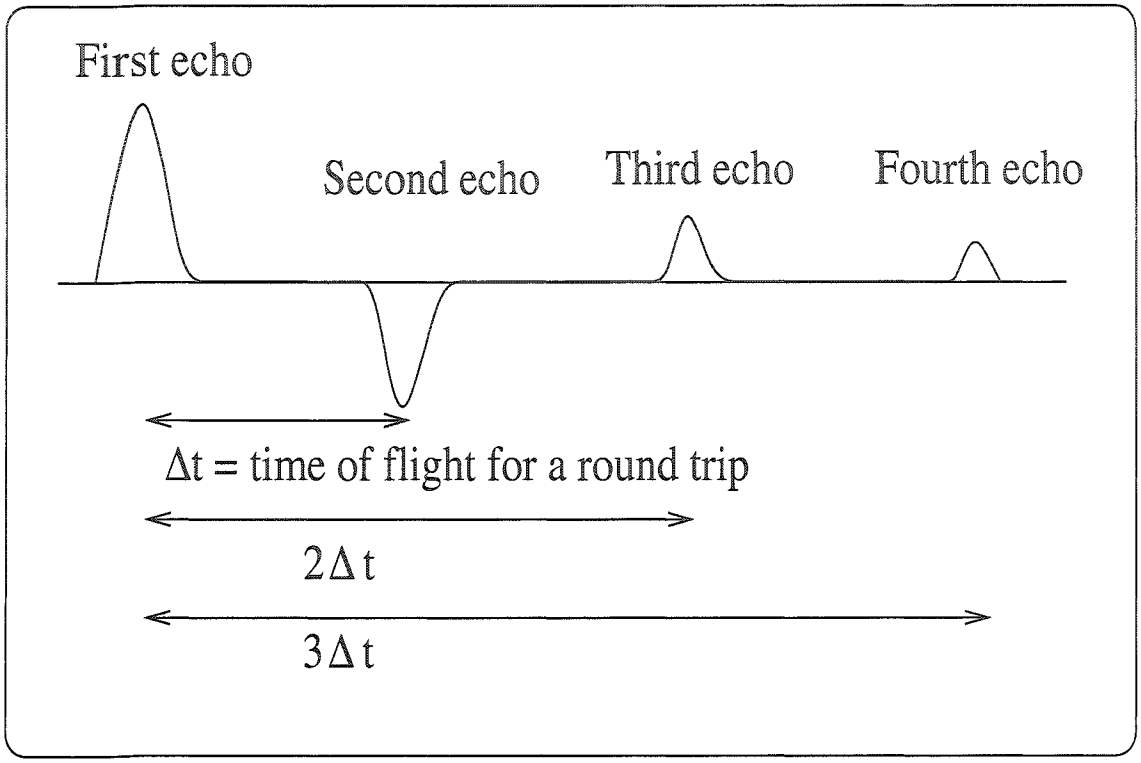

Figure 3.4: A typical multi-echo pattern on the Oscilloscope. The time Δt between the first and second echo is the time of flight for the sound wave to travel from the top to the bottom and back. The time between the first and the third is then $2\Delta t$, and so on.

From the equation 3.4, we can derive the expression for the relative phase change of the n-th echo

$$\frac{\Delta\Phi_n}{\Phi_n} = \frac{\Delta f}{f} + \frac{\Delta L}{L} - \frac{\Delta v}{v} \,. \tag{3.5}$$

The last expression shows that any phase variation caused by external parameters (the change in temperature T, the change in pressure P, and so on) can be offset by adjusting the frequency of the electrical signal. In fact, we can keep $\Delta\Phi$ being equal to zero, thus the relative change in the sound velocity can be expressed in terms of

the relative change in the frequency $\Delta f/f$ as well as the relative change in the length of the crystal $\Delta L/L$:

$$\frac{\Delta v}{v} = \frac{\Delta f}{f} + \frac{\Delta L}{L} . \tag{3.6}$$

For measurements as a function of temperature, the change of the sample's length ΔL can be easily estimated using the thermal expansion coefficient. It turns out that in most cases $\Delta L/L$ is an order of magnitude smaller than $\Delta v/v$. If we neglect the change in the crystal's length with temperature, the relative change in velocity can be approximated by

$$\frac{\Delta v}{v} \cong \frac{\Delta f}{f} . \tag{3.7}$$

Therefore, under the condition $\Delta\Phi = 0$, the relative change in velocity can be calculated from the frequency shift Δf and the frequency f. In this project, apart from investigating the temperature dependence of the sound velocity, we also study the effect of pressure on the velocity. In the later case, the variation of the sample's length can be found using the isothermal compressibility. The calculation shows that the relative change of the sample's length is negligible relative to that of the frequency. Thus, the method used in calculating the relative change in velocity caused by temperature can also be used for pressure. In both cases, the procedure is the same. Each time the Boxcar detects a phase difference, the computer adjusts the frequency of the Synthesizer in order to bring the phase difference back to zero. The computer is also used to record the frequencies, which are subsequently used to calculate the relative change in velocity. In this technique, the frequency stability of the synthesizer is really what ensures the high resolution of the interferometer. The frequency used in this experiment is normally around 30 MHz with frequency adjustment as small as 10 Hz. Consequently, a resolution as high as 1 part per million can be achieved using this technique.

3.4 The Pressure Cell and the Sample Holder

One of the gaols of this project is to derive the temperature-pressure phase diagram of $Rb_4LiH_3(SO_4)_4$. For this, we need to measure the temperature dependence of the sound velocities under different pressures. This was achieved by putting the sample-transducer assembly into a pressure cell. As shown in Fig. 3.5, the body of the pressure cell is a hollow cylinder, made of Cu-Be alloy so that it can sustain pressures up to 12 $kbar$. The teflon cell and the sample holder are placed in the chamber of the cylinder. After the obturator and the piston (plug) are introduced, the cell is closed by two screws. For the purpose of transmitting pressure, the teflon cell is filled with $3methyl-1-butanol$ solution. The advantage of this solution lies in its low freezing temperature. At ambient pressure, it has a freezing temperature of 123 K which is below the critical temperature ($T_c = 132\ K$) of the phase transition observed in $Rb_4LiH_3(SO_4)_4$ at ambient pressure. At pressure as high as 10 $kbar$, the freezing point of this solution is still well below the transition temperature of $Rb_4LiH_3(SO_4)_4$. This ensures that the pressure applied on the crystal is quasi-hydrostatic as long as the temperature is not well below T_c. The pressure is exerted by a hydraulic unit. Applying a force to the pusher, the Piston (Plug) will be pushed forward. As the liquid inside the Teflon cell is almost incompressible, hydrostatic pressure builds up in the compressed Teflon cell. At the desired pressure, the cap screw is tightened, and the hydrostatic pressure is locked inside the cell. In order to hold the sample and the transducer together a small sample holder is used. As shown in Fig.3.6, the transducer is held on the surface of the sample by the piston tip which produces a gentle force on the transducer due to a small compressed spring. To improve the coupling, the transducer is often bonded to the surface of the sample with a thin layer of glue. After the sample is mounted, the sample holder is connected to the obturator.

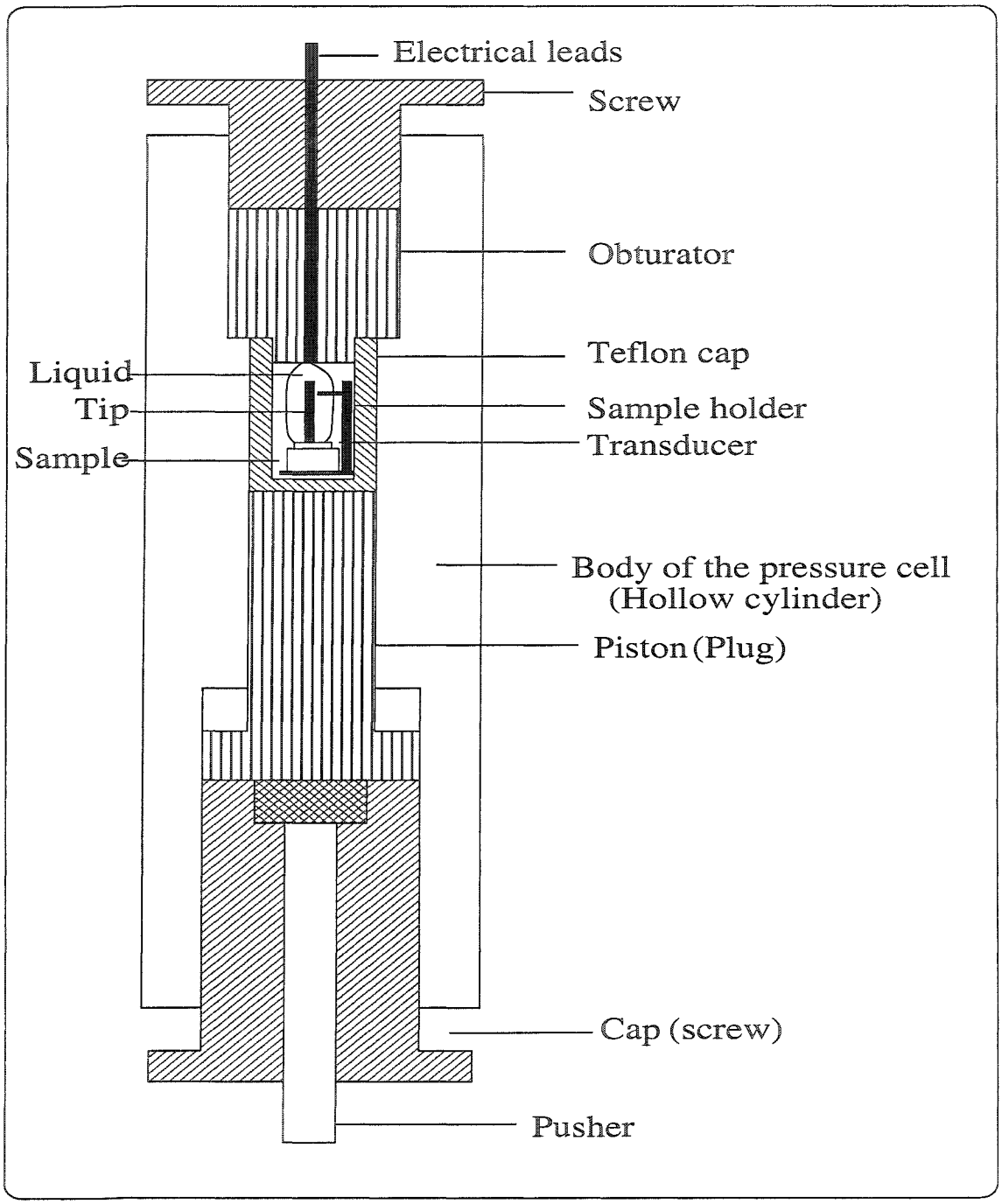

Figure 3.5: A schematic drawing of the pressure cell. The sample is immersed in a $3methyl-1-butanol$ solution contained in a teflon cell.

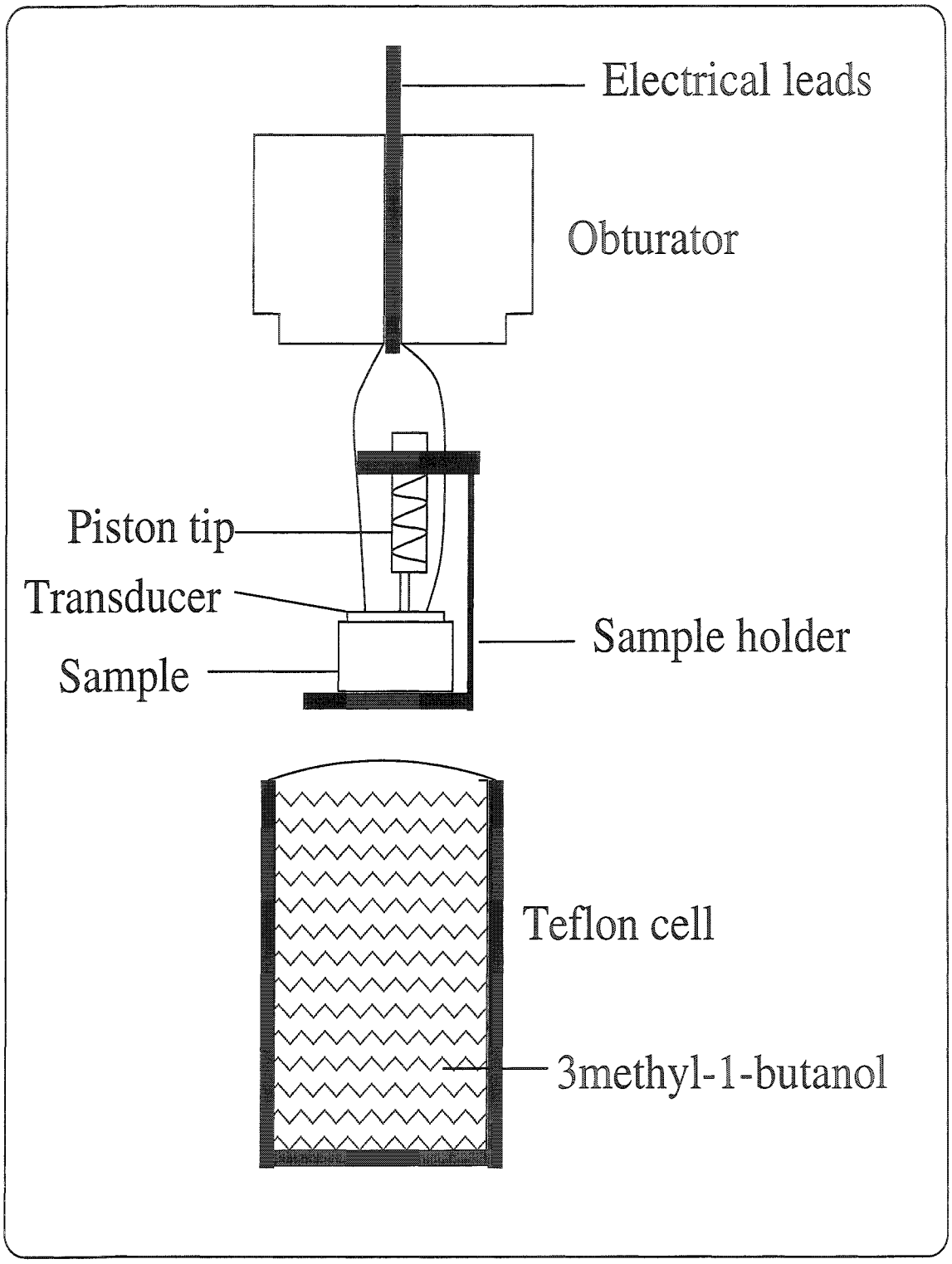

Figure 3.6: A close look at the sample holder and its structure.

The sample holder is then put into the 3methy-1-butanol solution contained in the Teflon cell. After that, the obturator bearing the teflon cell is introduced in the body of the pressure cell.

3.5 Pressure and Temperature Measurements

The pressure in the pressure cell is determined by measuring the resistance of the lead wire which is mounted next to the sample. To improve the accuracy of the measurement, a four contact configuration is adopted. The pressure dependence of the resistance of lead has been well studied [53, 67]. It is found that at temperature T the ratio $R(P,T)/R(0,T)$ (where R(P,T) and R(0,T) correspond to the lead wire resistances measured at pressures P and 0 *kbar*, respectively) is temperature independent [67]. Using the expression for the pressure as a function of the normalized resistance of the lead, pressures at various temperatures can be determined. It turned out that due to the thermal contractions of the different elements of the cell, the pressure in the pressure cell changes with temperature. At temperatures around 100 K, a pressure drop of a few *kbar* is often observed. A typical pressure-temperature curve is given in Fig. 3.7. From this curve, we see that the hydraulic pressure decreases with cooling till 125 K, at which the liquid in the Teflon cell freezes, then remains constant. In this particular case, we observed a pressure drop of 2 *kbar*. The pressure was measured using this method to an accuracy of 0.1 *kbar*.

In our experiment, the temperature is controlled and measured by a Lake Shore 340 temperature controller. Calibrated cernox resistors are used as the temperature sensors. For sound velocity measurements realized at ambient pressure, the sensor was mounted on the sample holder. However, for measurements as a function of pressure, the sensor was mounted on the outside wall of the pressure cell. The cooling or

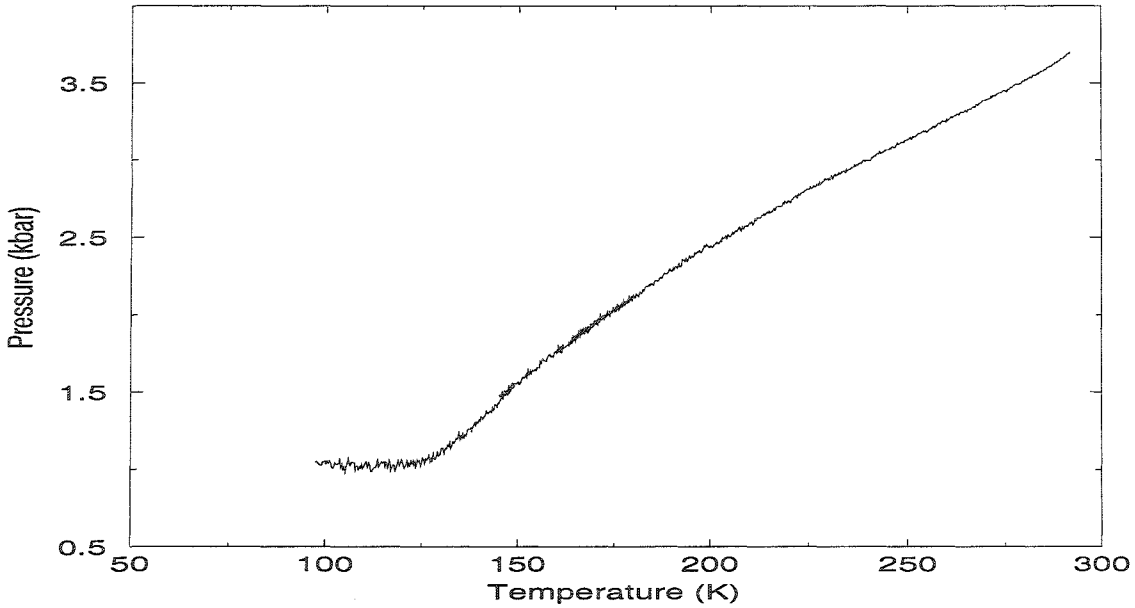

Figure 3.7: Pressure as a function of temperature. The pressure at room temperature is 3.7 *kbar*.

heating rate is regulated by the temperature controller through a heater located at the bottom of the cryostat. The temperature measurement in this experiment has an accuracy of 0.01 K.

Chapter 4

Experimental Results

The experimental goal of this project was to investigate the elastic properties of $Rb_4LiH_3(SO_4)_4$ as a function of temperature and pressure. Consequently, in order to determine as many independent elastic constants as possible, we measured the sound velocities of longitudinal and transverse waves propagating along specific crystallographic directions of single crystals of $Rb_4LiH_3(SO_4)_4$. In this chapter, we essentially present the results of sound velocity measurements realized as a function of temperature and pressure. From these measurements, five of the seven independent elastic constants of the high temperature phase (tetragonal structure) of $Rb_4LiH_3(SO_4)_4$ are obtained. We also derived the pressure-temperature phase diagram of $Rb_4LiH_3(SO_4)_4$ between 4 K and 300 K. The aim of this chapter is, therefore, to present the experimental results, a detailed analysis of the results will be presented in Chapter 5.

4.1 Sound Velocities and Elastic Constants at Ambient Pressure

In order to describe the elastic properties of $Rb_4LiH_3(SO_4)_4$, we need to determine all its independent elastic constants. As stated previously, the elastic constants can be obtained through a series of sound velocity measurements. As long as the crystal structure is known, the specific relations between the velocity and the independent elastic constants for any acoustic modes can be derived using the Christoffel equations (see Eq. 2.45). Thus, in general, the sound velocity can always be written as

$$v = \sqrt{\frac{C_{eff}}{\rho}} \tag{4.1}$$

where ρ represents the crystal density and C_{eff} stands for an effective elastic constant associated with the measured acoustic mode. At room temperature, as the crystal structure of $Rb_4LiH_3(SO_4)_4$ belongs to the tetragonal point group 4 [6], the effective elastic constants for some specific modes and directions correspond to the expressions given in Table 2.1. However, for this investigation, we limited our measurements to the modes and directions listed in Table 4.1. From Table 4.1, we immediately see that the elastic constants C_{33} is directly proportional to the square of the sound velocity of longitudinal mode propagating along the z-axis, $V_{L[001]}$. A similar observation stands for C_{44} which is associated with the velocity of transverse mode propagating along the x-axis with its polarization along the z-axis, $V_{Tz[100]}$. Unfortunately, the relations between the remaining elastic constants and velocities are not so straightforward. However, as C_{16} is known to be relative small [14, 21], we see that the velocity of the longitudinal mode propagating along the x-axis, $V_{L[100]}$, is dominated by C_{11} while the velocity of transverse mode polarized along y-axis, $V_{Ty[100]}$, should give a good estimate for C_{66}. Finally, using the obtained values for C_{11} and C_{66}, the elastic

Direction	Mode	Tetragonal
..	L	$\rho V^2_{L[100]} = \frac{1}{2}\left(C_{11} + C_{66} + \sqrt{(C_{11} - C_{66})^2 + 4C_{16}^2}\right)$
[100]	T_y	$\rho V^2_{Ty[100]} = \frac{1}{2}\left(C_{11} + C_{66} - \sqrt{(C_{11} - C_{66})^2 + 4C_{16}^2}\right)$
..	T_z	$\rho V^2_{Tz[100]} = C_{44}$
[001]	L	$\rho V^2_{L[001]} = C_{33}$
[110]	L	$\rho V^2_{L[110]} = \frac{1}{2}\left(C_{11} + C_{66} + \sqrt{(C_{12} + C_{66})^2 + 4C_{16}^2}\right)$
..	$T_{[\bar{1}10]}$	$\rho V^2_{T_{[\bar{1}10]}[110]} = \frac{1}{2}\left(C_{11} + C_{66} - \sqrt{(C_{12} + C_{66})^2 + 4C_{16}^2}\right)$

Table 4.1: Expressions of ρV^2 as a function of the elastic constants for the acoustic modes measured in this project. Note that these equations are only valid for the tetragonal structure. Here L represents longitudinal modes, T_j stands for transverse modes polarized along the j-direction. In this Table, $V_{L[100]}$ represents the velocity of longitudinal mode propagating along the x-axis and $V_{Ty[100]}$ represents the velocity of transverse mode propagating along the x-axis and polarized along the y-axis, and so on.

Direction	Mode	v (m/s)
..	L	3450 ± 30
[100]	T_y	1840 ± 20
..	T_z	1560 ± 20
..	L	3930 ± 30
[001]	T_x	1540 ± 20
..	T_y	1570 ± 20
..	L	3980 ± 60
[110]	$T_{[\bar{1}10]}$	1300 ± 10
..	T_z	1650 ± 20

Table 4.2: Sound velocities obtained at room temperature. The directions and modes were chosen according to Table 2.1. Here, L stands for longitudinal modes, and T_j represents transverse modes with its polarization along the j-direction.

constant C_{12} can then be derived from the velocity of transverse mode propagating along the [110] direction with its polarization perpendicular to the z-axis, $V_{T_{\bar{1}10}[110]}$. Thus, using our sound velocity measurements, listed in Table 4.2, along with the reported crystal density ($\rho = 2.81\ g/cm^3$) [14] of $Rb_4LiH_3(SO_4)_4$, it is possible to obtain some of the room temperature independent elastic constants. The elastic constants obtained in this project, along with results obtained by other groups [14, 21] are presented in Table 4.3. Our results agree particularly well with those reported by B. Mróz et al. [14] obtained via Brillouin scattering measurements. They also agree with those obtained by T. Breczewski et al. [21] except for C_{12} for which they obtained a significantly lower value. The fact that we were able to reproduce the published values for the elastic constants of $Rb_4LiH_3(SO_4)_4$ indicates that all samples used in

Elastic Constants	$10^{10}\ N/m^2$		
	This Work	Ref. [21]	Ref. [14]
C_{11}	3.34±0.06	3.26	3.30
C_{33}	4.34±0.07	4.08	4.17
C_{44}	0.68±0.01	0.67	0.70
C_{66}	0.95 ±0.02	1.01	1.02
C_{12}	2.39 ±0.08	1.40	2.40
C_{13}		0.54	
C_{16}		0.33	-0.10

Table 4.3: Elastic constants of $Rb_4LiH_3(SO_4)_4$ for the tetragonal structure at 295 K. For comparison, data obtained by two other groups are also presented.

this investigation were properly oriented.

4.1.1 Temperature Dependence of Sound Velocities

The temperature dependence of the sound velocity for all the modes listed in Table 4.1 has been investigated between 4 K and 300 K. In Fig. 4.1, we present the temperature dependence of the velocities of longitudinal modes propagating along [001] and [100], respectively. Along both directions, we observe a drop in the velocity at a temperature of $132.2 \pm 0.3\ K$. According to specific heat measurements and optical studies [18], this temperature corresponds to the occurrence of a second order ferroelastic transition in $Rb_4LiH_3(SO_4)_4$. This transition was initially described as a tetragonal to orthorhombic structural change corresponding to a $4mm \rightarrow mm2$ symmetry change [9, 10, 17]. However, recent x-rays measurements [11] seem to indicate

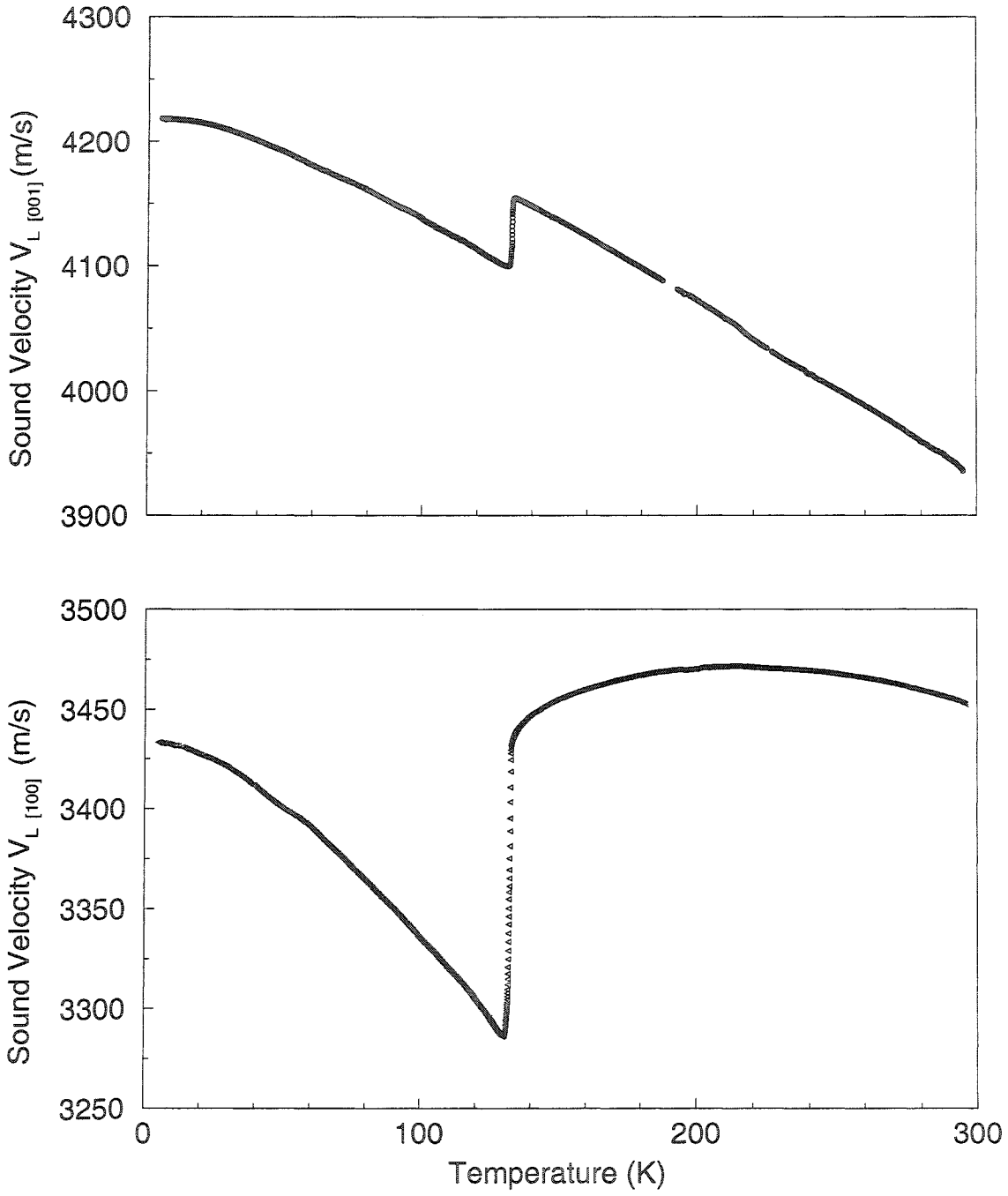

Figure 4.1: Temperature dependence of the sound velocity of longitudinal modes propagating along the z-axis ($V_{L[001]}$) and x-axis ($V_{L[100]}$), respectively.

that the low temperature phase is rather monoclinic and that a $4 \longrightarrow 2$ type symmetry change is a more appropriate designation. Our measurements also indicate that the sound velocity of longitudinal waves propagating along the z-axis ($L[001]$ mode) changes by 1.2% at the transition temperature, while it drops by 5% for longitudinal waves propagating along x-axis ($L[100]$ mode). At temperatures above the transition, the velocity increases almost linearly with cooling for the $L[001]$ mode. However, for the longitudinal mode propagating along the x-axis, the velocity shows a temperature dependence which is clearly nonlinear. Initially, it increases with cooling from room temperature and then decreases with further cooling. As we will see in Chapter 5, this unusual temperature dependence can be associated with a soft mode. In the low temperature phase, the velocities along both directions increase monotonically with cooling with no sign of any other phase transitions. Let add that results presented in Fig. 4.1 agree very well with those reported by Hempel et al. [12] and Breczewski et al. [21]. For example, for the $L[100]$ mode, our measurements of the magnitude of the velocity variation in the transition is comparable with the drop 5.6% observed by Breczewski et al. [21]. However, our results do not agree so well with Brillouin scattering measurements [14]. In that case, the velocity does not show any jump at the transition temperature. The fact that they failed to detect a velocity drop of 5% cannot be ascribed to their lower resolution of about 1%.

Among all the acoustic modes measured in this project, the one corresponding to transverse waves propagating along [110] and polarized perpendicularly to the z-axis shows the largest temperature dependence, see Fig. 4.2. In comparison with $L[100]$ mode, the velocity for this mode starts to decrease at a much higher temperature and decreases more rapidly. From 300 K to 140 K, the velocity decreases by about 50%. Due to the high acoustic attenuation near T_c, the signal is invariantly lost. For that reason, only measurements in the temperature range between 140 K and 300 K are

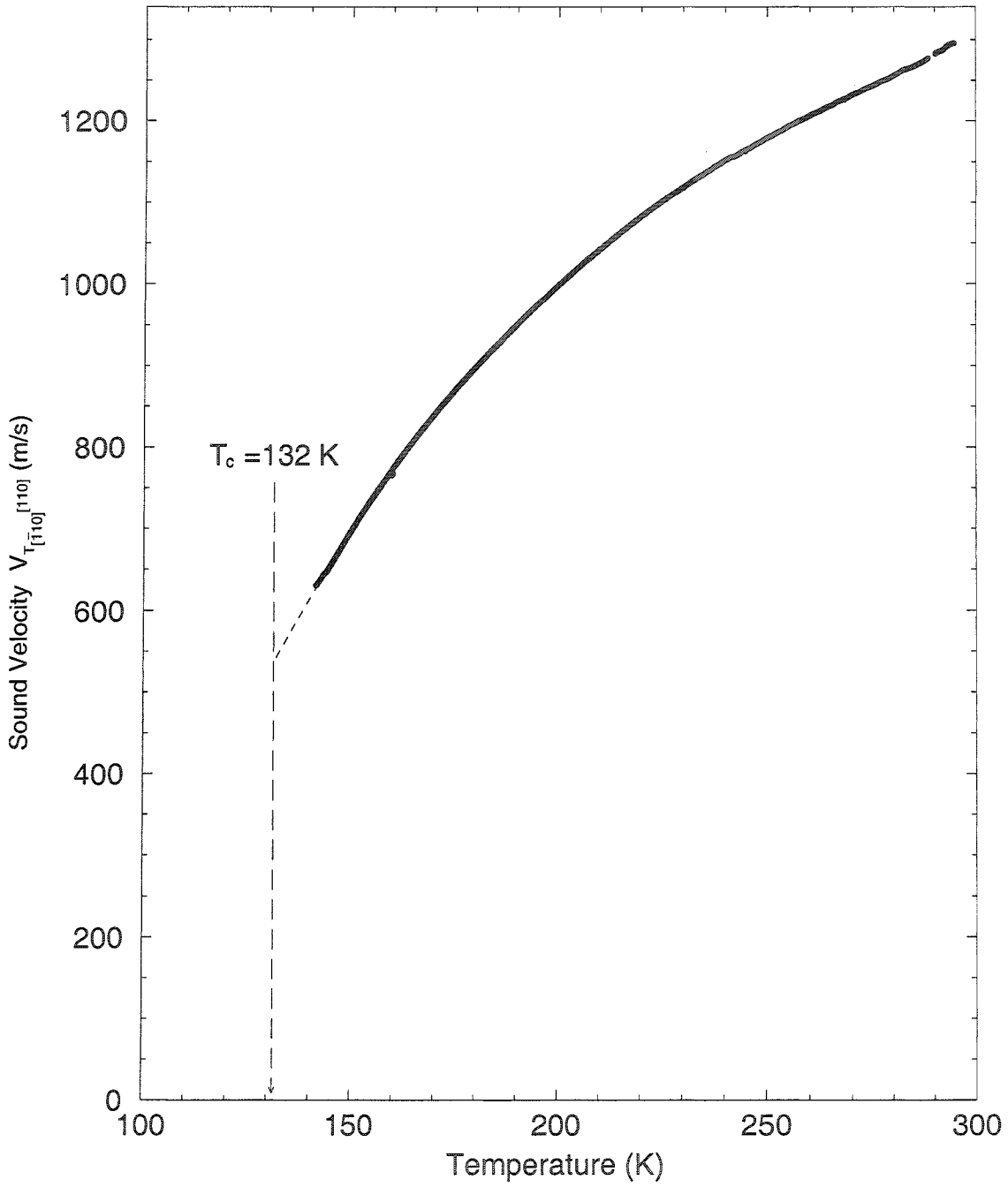

Figure 4.2: Temperature dependence of the sound velocity of transverse waves propagating along [110] with their polarization normal to the z-axis, $V_{T_{[\bar{1}10]}[110]}$.

presented in Fig. 4.2. For that particular mode, the rapid decrease in the velocity is obviously a precursor effect associated with the softening of a normal mode well above T_c. However, the velocity for this mode does not behave as a typical soft mode since it does not seem to decrease to zero at the transition temperature T_c. By extrapolating the velocity curve down to T_c, we find that the velocity at the transition temperature is approximately 540 m/s. Furthermore, the temperature dependence is nonlinear. All these observations are consistent with results reported by both Mróz et al. [14] and Breczewski et al. [21].

The temperature dependence of the velocities of two transverse modes, $Ty[100]$ and $Tz[100]$, are presented in Fig. 4.3. Both curves show an observable change in velocity at the transition temperature though the changes are considerably smaller. The curve for the $Ty[100]$ mode clearly shows a small variation in velocity at T_c (132 K), while for the $Tz[100]$ mode, it shows a slight increase in slope. Except in the vicinity of the transition, the velocity variations for both modes are typical. From 300 K to 4 K, the sound velocities $V_{Ty[100]}$ and $V_{Tz[100]}$ only increase by 3.8% and 4.7%, respectively. Again, let's mention that our sound velocity measurements for both modes are in good agreement with those obtained by Breczewski et al. [21].

Finally, we present in Fig. 4.4 the temperature dependence of the velocity of longitudinal modes propagating along [110] and [011], respectively. Again, both curves show a considerable jump at T_c. For the $L[011]$ mode, the drop in velocity is about 3.3% while for the $L[110]$ mode it is estimated to be no less than 2.4%. Above T_c, the velocities along both directions increase monotonically with cooling from room temperature. However, in the low temperature phase we could not obtain reproducible results for the $L[110]$ mode. That explains why only the results obtained at temperatures above T_c are presented. Comparatively, the measurements for the $L[011]$ mode are much better though the curve shows that the velocity for this mode reaches its

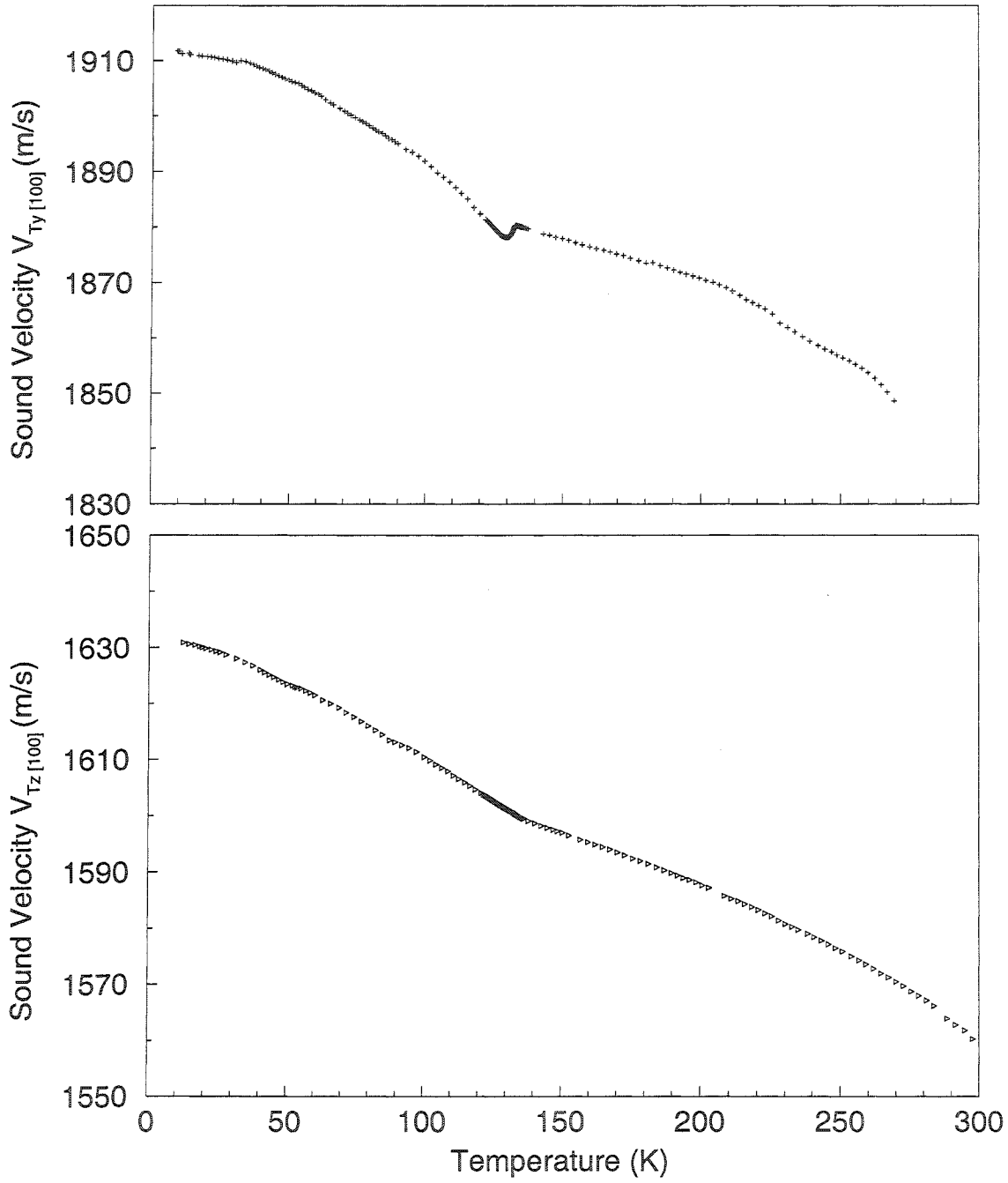

Figure 4.3: Temperature dependence of the sound velocity of transverse modes propagating along the x-axis with their polarizations along the y and z-axis, respectively ($V_{Ty[100]}$ and $V_{Tz[100]}$).

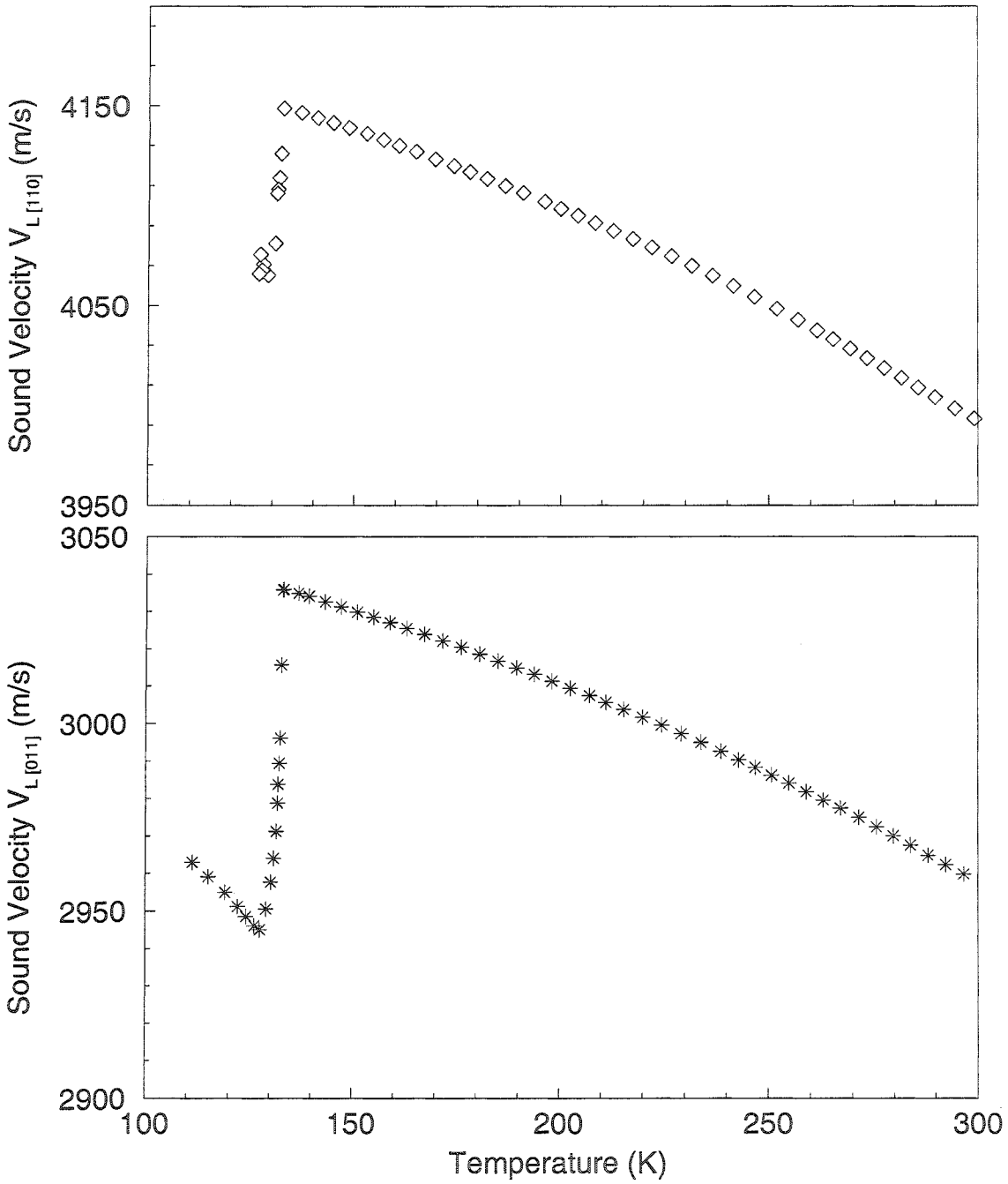

Figure 4.4: Temperature dependence of the sound velocities for longitudinal waves propagating along [110] and [011] directions, respectively ($V_{L[110]}$ and $V_{L[011]}$).

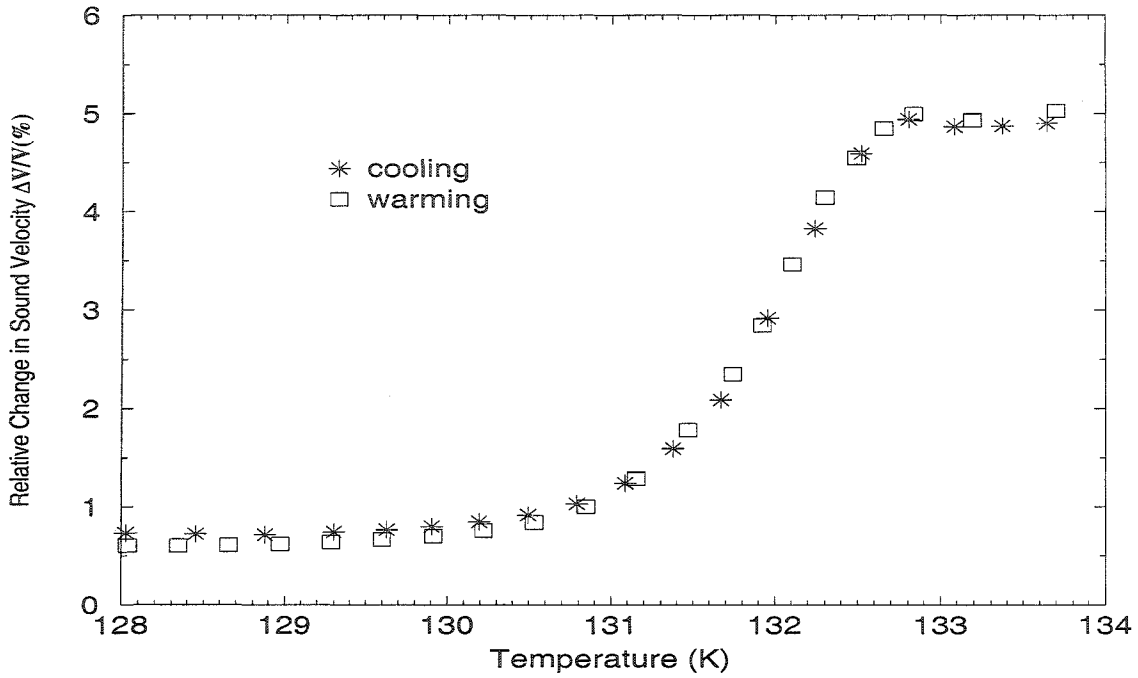

Figure 4.5: Thermal hysteresis measurements using the velocity of longitudinal mode propagating along the z-axis.

minimum at 127 K, well below T_c. Both of these two phenomena might be caused by twinning and domain stress effects in the monoclinic phase.

In order to confirm the nature of the transition, we compared in Fig. 4.5 the temperature dependence of the velocity $V_{L[100]}$ obtained during a cooling-heating cycle. As shown in Fig.4.5, we observe no thermal hysteresis. This observation confirms that the transition is indeed second order, consistent with the conclusion based on pyroelectric [18], dielectric [18] and specific heat measurements [12, 18].

It is well known that for crystals that have a tetragonal structure, the lattice parameter a and b are indistinguishable, i.e. the x-axis and the y-axis are equivalent. However, for crystals with a monoclinic structure, a is no longer equivalent to b, in another word, the x-axis is different from the y-axis. As stated previously, above and

below T_c, $Rb_4LiH_3(SO_4)_4$ single crystals have a tetragonal and monoclinic symmetry, respectively. In order to distinguish the x and y axes in the low symmetry phase, we measured, using the same sample, the temperature dependence of the velocity of longitudinal waves propagating along two orthogonal directions in the $a-b$ plane. The results presented in Fig. 4.6 show that both measurements coincide above T_c, which is consistent with the fact that the high temperature phase has a tetragonal symmetry. For the monoclinic phase, we expect to see a significant difference between both curves. On the contrary, the difference turns out to be trivially small. As we see from Fig. 4.6, even at a temperature 45 degrees below T_c, the velocities along both directions deviate by only 0.3%. According to optical studies [9], in the monoclinic phase two kinds of birefringent domains are observed. Moreover, these domains are separated by perpendicular walls lying in the (100) and (010) planes. If we assume that the two kinds of domains fill the crystal volume at the same ratio, we can understand why the sound velocity measurements along the x and y-directions remain almost identical. The same conclusion has been reached by Piskunowicz et al. [19] based on thermal expansion measurements.

4.1.2 Temperature Dependence of the Elastic Constants

Using the sound velocity measurements presented in section 4.1.1, the temperature dependence of five of the seven independent elastic constants of $Rb_4LiH_3(SO_4)_4$ have been determined. Making use of the temperature dependence of the sound velocities, we can, in principle, solve the set of equations listed in Table 4.1. From Table 4.1, we see that the elastic constants C_{33} and C_{44} can be obtained directly from their corresponding velocities. However, deriving C_{11} , C_{66} and C_{12} is much more difficult. However, as C_{16} is known to be almost temperature independent [14, 21], values for

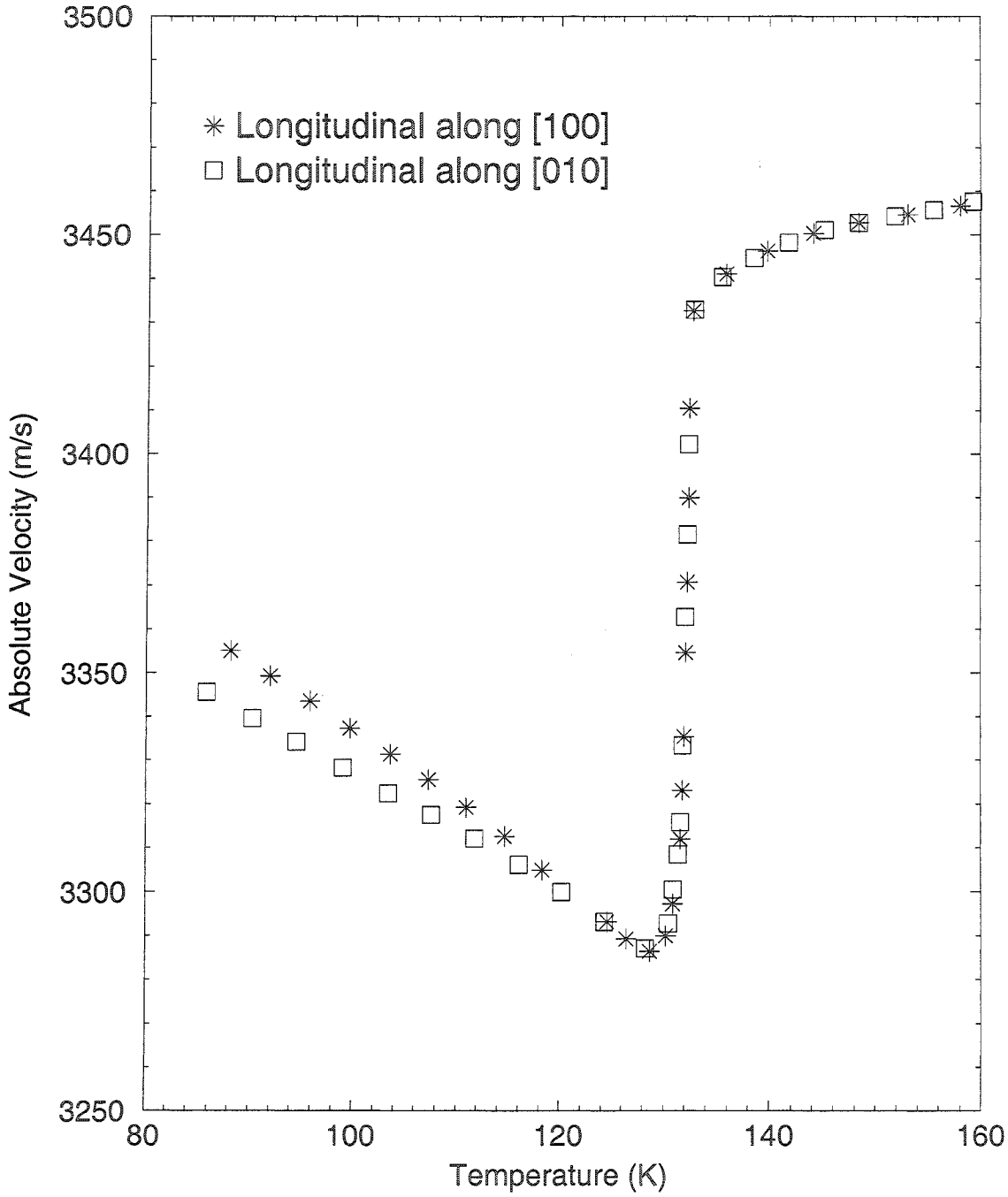

Figure 4.6: Temperature dependence of the sound velocities for longitudinal waves propagating along the two crystallographic axes a and b directions. In conformity with the convention, the coordinates axes x and y are set to be along a and b, respectively.

these three elastic constants can be estimated by using $V_{L[100]}$, $V_{Ty[100]}$ and $V_{T_{\bar{1}10}[110]}$. For instance, as C_{16} is relatively small, the velocity of the $L[100]$ mode is dominated by C_{11}, see Table 4.1. The temperature dependence of five independent elastic constants are presented in Fig. 4.7, where C_{16} has been assumed to be constant with the value of $0.33 \times 10^{10}\ N/m^2$ [21]. It should be noted that the elastic constants in the monoclinic phase are calculated using the Christoffel equations derived for the tetragonal phase. Therefore, they do not necessarily correspond to the elastic constants in the monoclinic phase. The results presented in Fig. 4.7 indicate that the elastic constant C_{33} increases almost linearly with cooling and shows a step-like variation of 3% at T_c (132 K). After that, it still increases linearly with further cooling down to 25 K. Clearly, the linear increase of C_{33} with cooling is a consequence of the normal thermal behavior of the corresponding acoustic phonons. For the elastic constant C_{11}, we see that it becomes soft at temperatures well above T_C. At the transition temperature, this elastic constant shows a relative change of 9 %, the largest relative variation observed for this crystal. In contrast, the variations of the elastic constants C_{44} and C_{66} are quite small. At T_c, C_{66} shows a very small variation while C_{44} shows a slight change in slope. Figure 4.7 also shows that the elastic constant C_{12} increases rapidly with cooling. As no good measurements can be used to calculate C_{12} below T_c, only the results obtained at temperatures above T_c are presented.

According to our sound velocity measurements, the mode that shows the largest variation in velocity above T_c is associated with transverse waves propagating along the [110] with a polarization normal to the z-axis ($V_{T_{[\bar{1}10]}[110]}$, Fig. 4.2). Considering that for the tetragonal structure, we have that

$$\rho V^2_{T_{[\bar{1}10]}[110]} = \frac{1}{2}\left(C_{11} + C_{66} - \sqrt{(C_{12} + C_{66})^2 + 4C_{16}^2}\right) . \tag{4.2}$$

Using the approximation, where $C_{16} = 0$, we immediately obtained that the effective

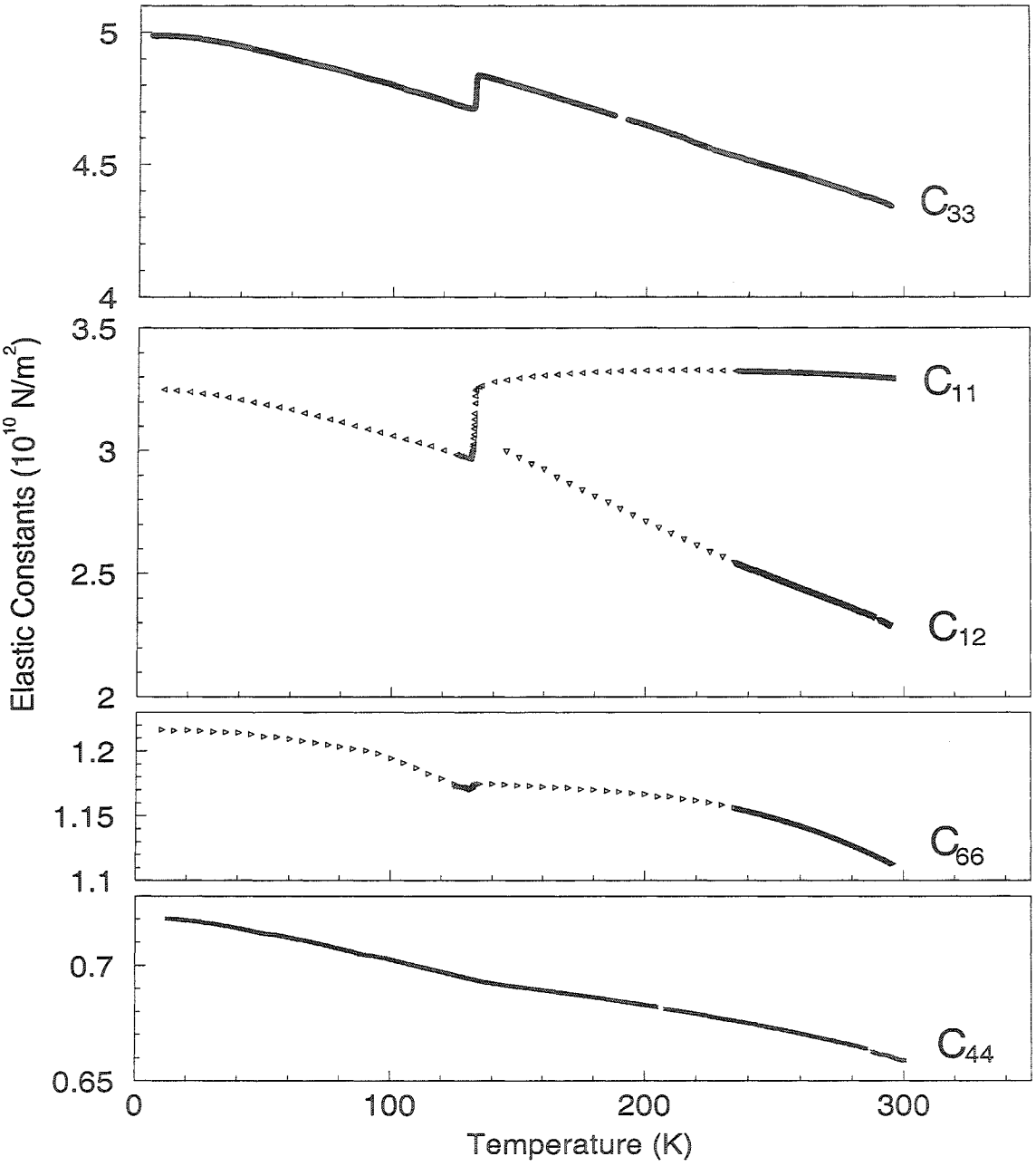

Figure 4.7: Temperature dependence of five of the seven independent elastic constants of the tetragonal phase for $Rb_4LiH_3(SO_4)_4$. Note that the values of the elastic constants in the monoclinic phase are not accurate since they are calculated using relations derived for the tetragonal phase.

elastic constants of the soft mode can be approximated by $(C_{11} - C_{12})/2$. For that reason, we present in Fig. 4.8 the temperature dependence of this elastic combination. As shown in Fig. 4.8, this elastic constant combination shows considerable softening well above T_c. From 300 K to 140 K, its value decreases by about 70%. However, this softening is incomplete because the elastic constant combination does not go to zero at the transition temperature. By extrapolating this curve to T_c (132 K), we find that the value of this elastic combination at T_c is 0.10×10^{10} N/m^2. Furthermore, we see that the temperature dependence of this elastic constant combination is nonlinear. This last observation might be an indication that this transition cannot be described as a proper ferroelastic phase transition. As we will see in Chapter 5, that this observation will be used as the foundation for our theoretical model.

4.2 Pressure Dependence of the Elastic Constants measured at Room Temperature

As point out in section 3.3, external parameters that can cause the structure of a crystal to change are not limited to temperature, the application of pressure P can also be used to induce a phase transition. To our knowledge, the effect of pressure on the properties of $Rb_4LiH_3(SO_4)_4$ have not been investigated yet. In this project, we measured the pressure dependence of the velocities using modes listed in Table 4.1. The effect of pressure on the velocities was studied using the pressure cell described in section 3.4. Using these velocity measurements realized at room temperature, we could calculate the pressure dependence of the elastic constants. Here, as well, we assume that C_{16} is constant ($C_{16} = 0.33 \times 10^{10}$ N/m^2) [21] so that the elastic constants C_{11}, C_{66} and C_{12} can be calculated using $V_{L[100]}$, $V_{Ty[100]}$ and $V_{T_{\bar{1}10}[110]}$. Thus, in this

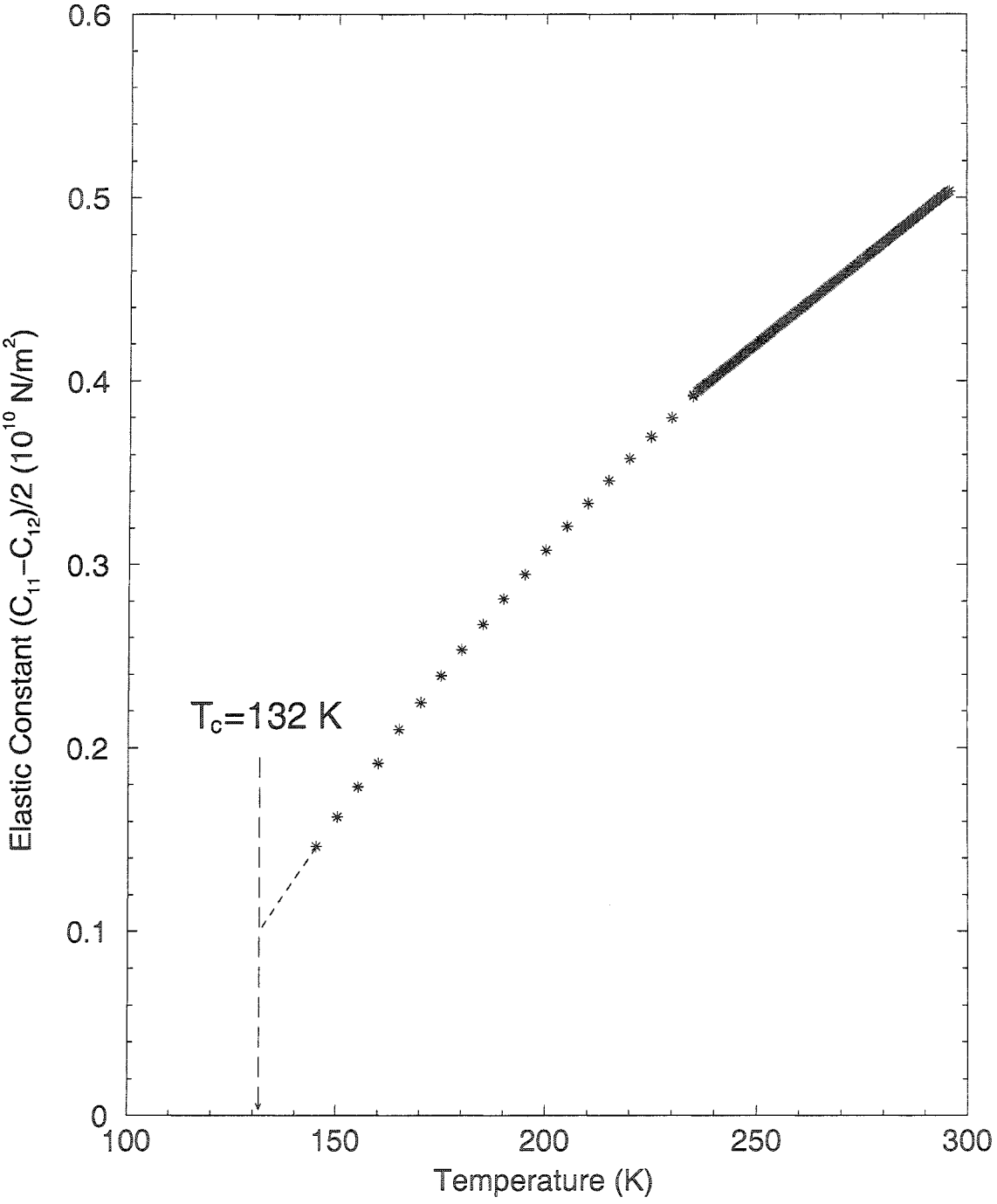

Figure 4.8: Temperature dependence of $(C_{11} - C_{12})/2$.

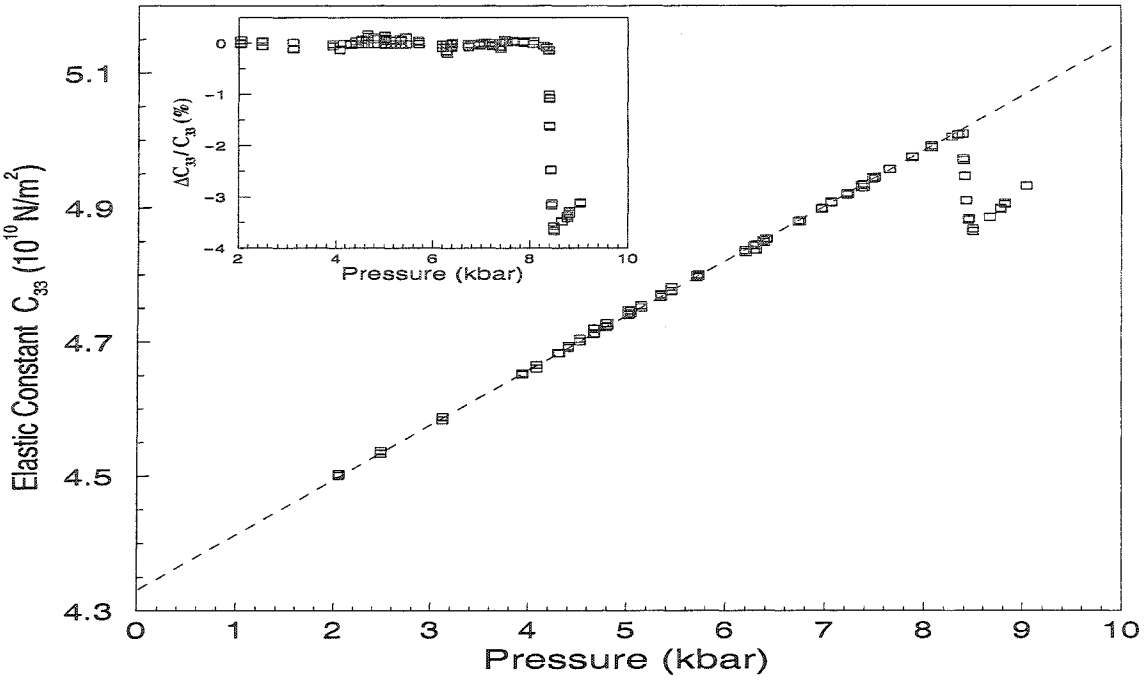

Figure 4.9: Pressure dependence of C_{33} at room temperature. The dashed line represents the linear extrapolation of the results of C_{33} at pressures below P_c.

section we present the pressure dependence of the elastic constants obtained at room temperature. Let add that the elastic constants in the monoclinic phase are calculated using the equations corresponding to the tetragonal phase. Therefore, they may not represent the elastic constants in the monoclinic phase.

We first present in Fig. 4.9 the pressure dependence of the elastic constant C_{33}. The curve clearly shows that C_{33} drops abruptly at a critical pressure of $P_c = 8.4\ kbar$. This rapid variation of 3.5% clearly indicates the occurrence of a phase transition. Based on the sound velocity measurements realized as a function of temperature, Fig. 4.1, we can assume that the transition observed at P_c corresponds to a $4 \longrightarrow 2$ symmetry change. Below P_c, the elastic constant C_{33} increases linearly with pressure at a rate of $0.08 \times 10^{10}\ N/m^2 \cdot kbar$. We can consider this variation to be typical

since for most crystals the elastic constants increase linearly with pressure, at least between 0 and 10 *kbar*. Significant nonlinear behavior are normally observed at higher pressures. Consequently, a linear extrapolation of the low pressure results can be used to evaluate the variations in the elastic constants which are strictly associated with the incidence of the phase transition. It is those variations that have to be compared to the theoretical predictions presented in Chapter 5. Thus, in the inset of Fig. 4.9 we present the variation of C_{33} produced by the phase transition. This variation is obtained by subtracting the linear extrapolation from the data presented in Fig. 4.9. As shown in the inset of Fig. 4.9, the effect of the transition on C_{33} is to produce a drop of 3.5% at P_c. Moreover, C_{33} increases with pressure at higher pressures.

The pressure dependence of C_{11} and C_{12} are presented in Fig. 4.10. Comparing with C_{33}, the elastic constant C_{11} shows a more pronounced jump at P_c. We also see that the precursor effect of the phase transition starts to affect C_{11} from pressures well below P_c. In this case, the linear extrapolation cannot be definitely determined using the low pressure results of C_{11}. For this reason, we assume that the linear extrapolation of C_{11} is similar to the one observed for C_{33}. Thus, the variation associated with the soft mode is obtained by subtracting a linear extrapolation derived from the results obtained on C_{33}. As shown in the inset, C_{11} gets softened at pressures well below P_c. At P_c, the phase transition causes a variation of 7% in the elastic constant. At pressures above P_c, the elastic constant begins to increase with pressure again. The curve for C_{12} shows that this elastic constant increases rapidly with pressure. From 0 *kbar* to 7.6 *kbar*, it increases by about 37%. Unfortunately, due to the limit of our sound velocity measurements, we could not derive the values of C_{12} at higher pressures. Among the elastic constants obtained in this project, two elastic constants, C_{11} and C_{33}, show significant variations around the transition, whether it is caused by temperature or by pressure. For comparison, we list in Table 4.2 their

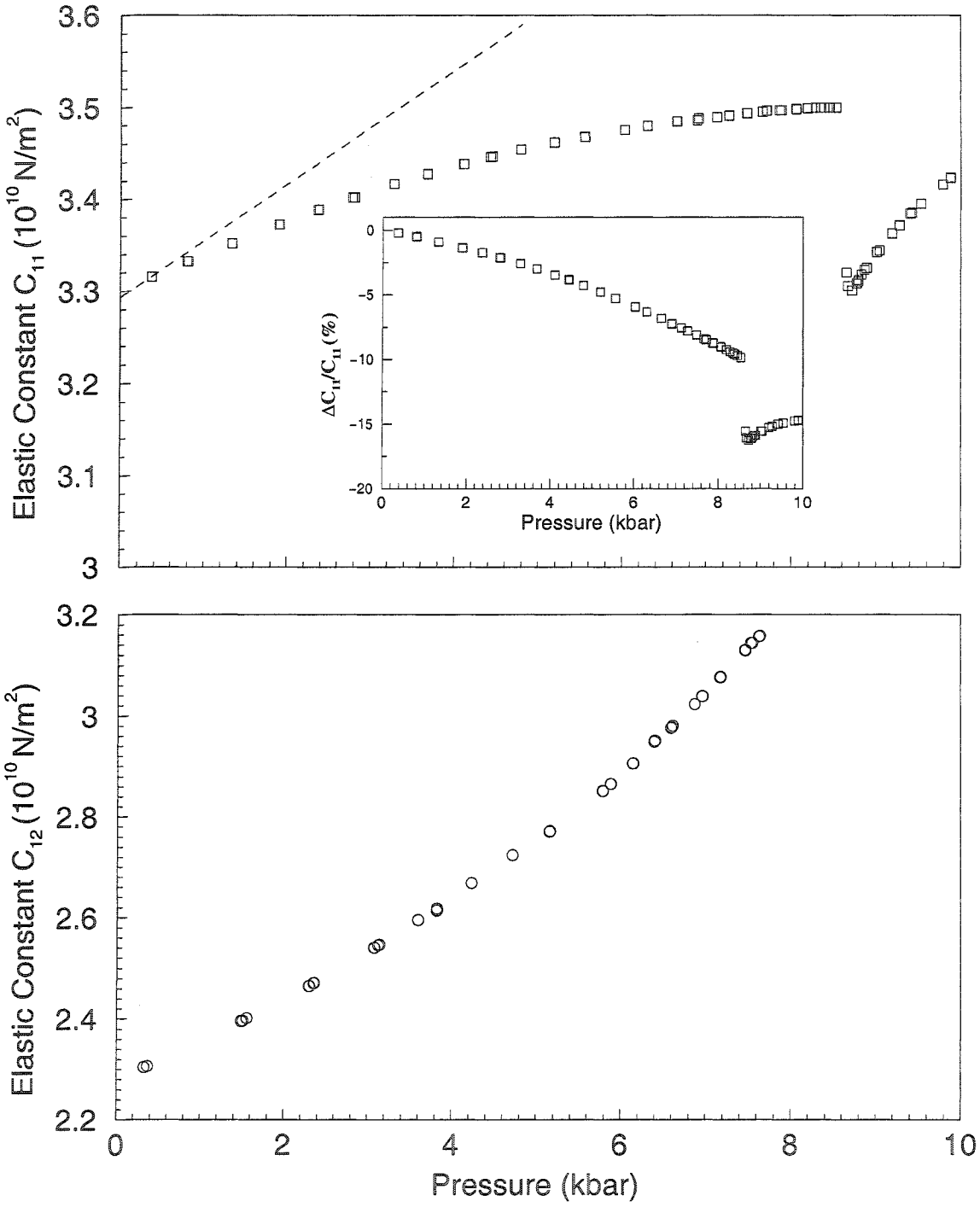

Figure 4.10: Pressure dependence of C_{11} and C_{12} at room temperature. The dashed line in the upper graph represents the linear extrapolation derived from the results obtained on C_{33}.

Parameters	C_{11}	C_{33}
Temperature	9%	3%
Pressure	7%	3.5%

Table 4.4: The variations of C_{11} and C_{33} at the transition caused by temperature and by pressure.

variations corresponding to both external parameters. As shown in Table 4.2, the magnitude of the variations are comparable.

Based on our sound measurements as a function of pressure, the velocity of transverse waves propagating along [110] with a polarization normal to the z-axis shows a strong pressure dependence below P_c, comparable with its temperature dependence above T_c (Fig. 4.2). As C_{16} is quite small [14, 21], from Table 4.1 we see that the effective elastic constant associated with the soft mode is approximately equal to $(C_{11} - C_{12})/2$. Consequently, we present in Fig. 4.11 the pressure dependence of $(C_{11} - C_{12})/2$. As we lost the signal at 7.6 *kbar*, when measuring the velocity for the mode $T_{[\bar{1}10]}[110]$, our calculation of $(C_{11} - C_{12})/2$ can only be extended up to that pressure. From Fig. 4.11, we see that $(C_{11} - C_{12})/2$ shows a large softening well below P_c. From 0 *kbar* to 7.6 *kbar*, its value decreases by about 70%. Extrapolating the curve to the critical pressure (8.4 *kbar*), it is found that at the critical pressure $(C_{11} - C_{12})/2$ is equal to $0.1 \times 10^{10}\ N/m^2$, which is the same as the value estimated from Fig. 4.8. This indicates that the softening of $(C_{11} - C_{12})/2$ is also incomplete in this case. Furthermore, we see that $(C_{11} - C_{12})/2$ shows a nonlinear dependence as a function of pressure. Both features further confirm that the observed transition is a pseudoproper ferroelastic phase transition.

Comparatively, the elastic constants C_{66} and C_{44} show a considerably weak pres-

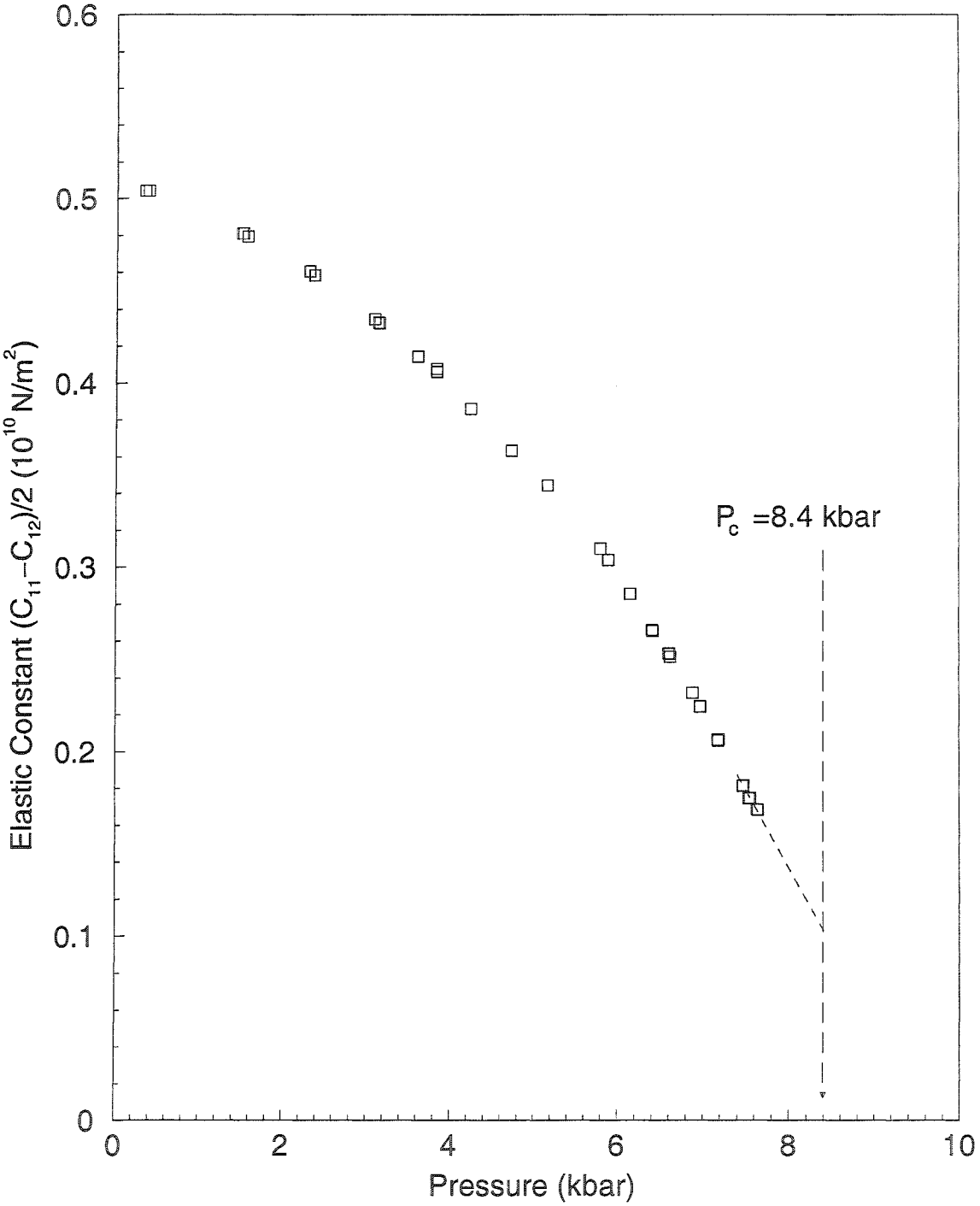

Figure 4.11: Pressure dependence of $(C_{11} - C_{12})/2$ for $Rb_4LiH_3(SO_4)_4$.

sure dependence, see Fig. 4.12. Nevertheless, they still undergo a considerable variation at the transition. At the critical pressure, the curves for C_{66} and C_{44} show a variation of 1.4% and an increase in the pressure dependence. Below P_c, both elastic constants increase linearly with pressure. Because the results below 2 *kbar* are not so good, the elastic constants corresponding to that pressure range are not presented. At pressures above P_c, they both increase with pressure, however, C_{66} increases with pressure considerably slower than C_{44} does.

4.3 Temperature-Pressure Phase Diagram

In order to derive the temperature-pressure phase diagram of $Rb_4LiH_3(SO_4)_4$, we measured the temperature dependence of the sound velocity at different pressures. The measurements have been realized using longitudinal waves propagating along the z-axis. This configuration has been chosen principally because the acoustic attenuation is small and that the transition temperature is easily observed. The temperature dependence of the sound velocities measured at different pressures is presented in Fig. 4.13. As the pressure in the cell decreases with cooling due to the thermal contractions, two pressures are given for each curve, the pressure measured at the room temperature and the pressure measured at the transition temperatures. The uncertainty on the pressure determination is estimated to be ± 0.2 *kbar*. The main feature of this figure is that the transition temperature shifts toward higher temperatures as the pressure increases. The curve at the bottom of the figure shows that at 6.6 *kbar* the transition temperature has been shifted to a value well above room temperature. Except for this one, all curves show a drop in velocity at the transition temperature. Though the magnitude of these drops differ a little from one to the other, no sign show that it has been damped by increasing the pressure. However, the shape of

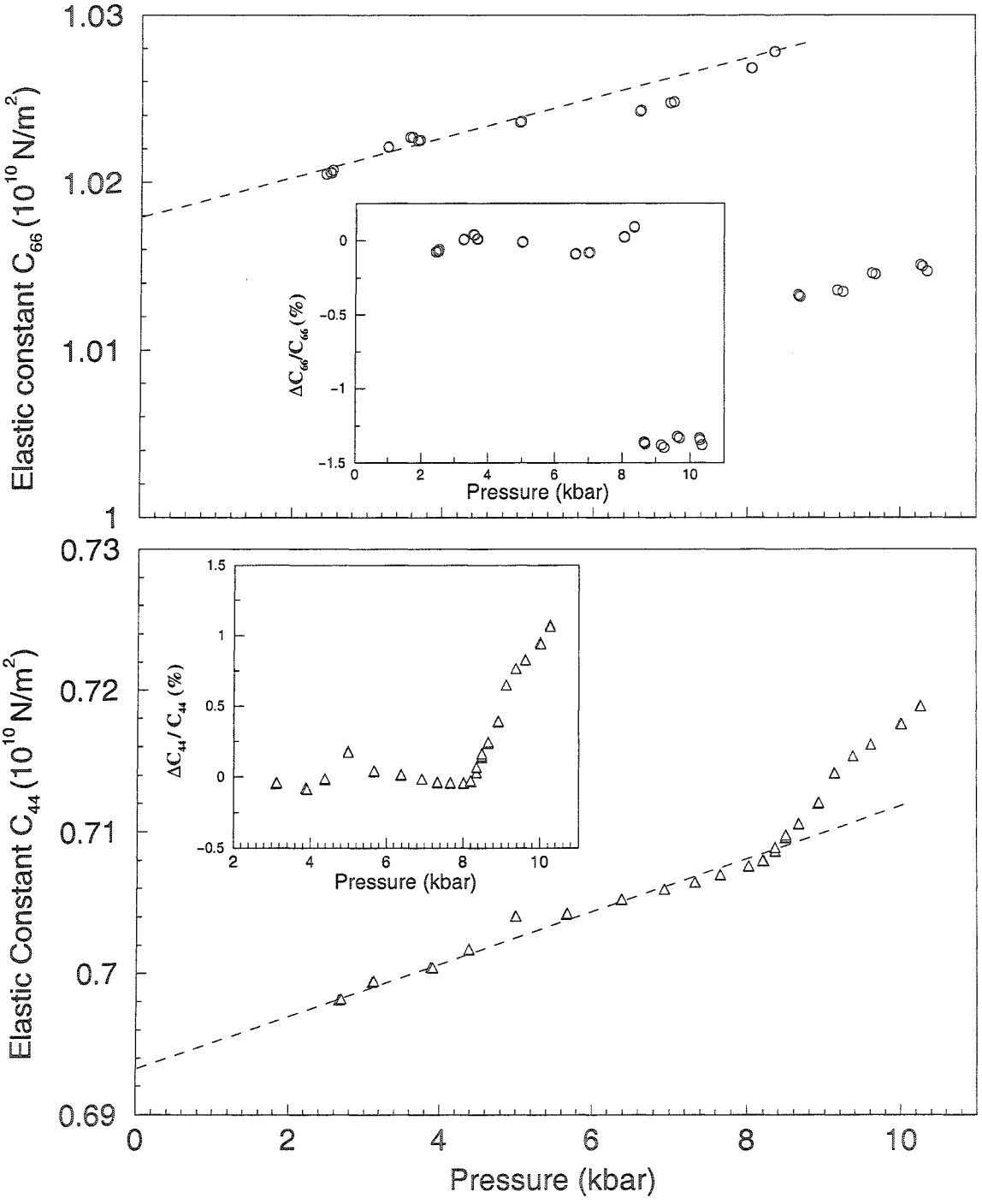

Figure 4.12: Pressure dependence of C_{66} and C_{44} for $Rb_4LiH_3(SO_4)_4$.

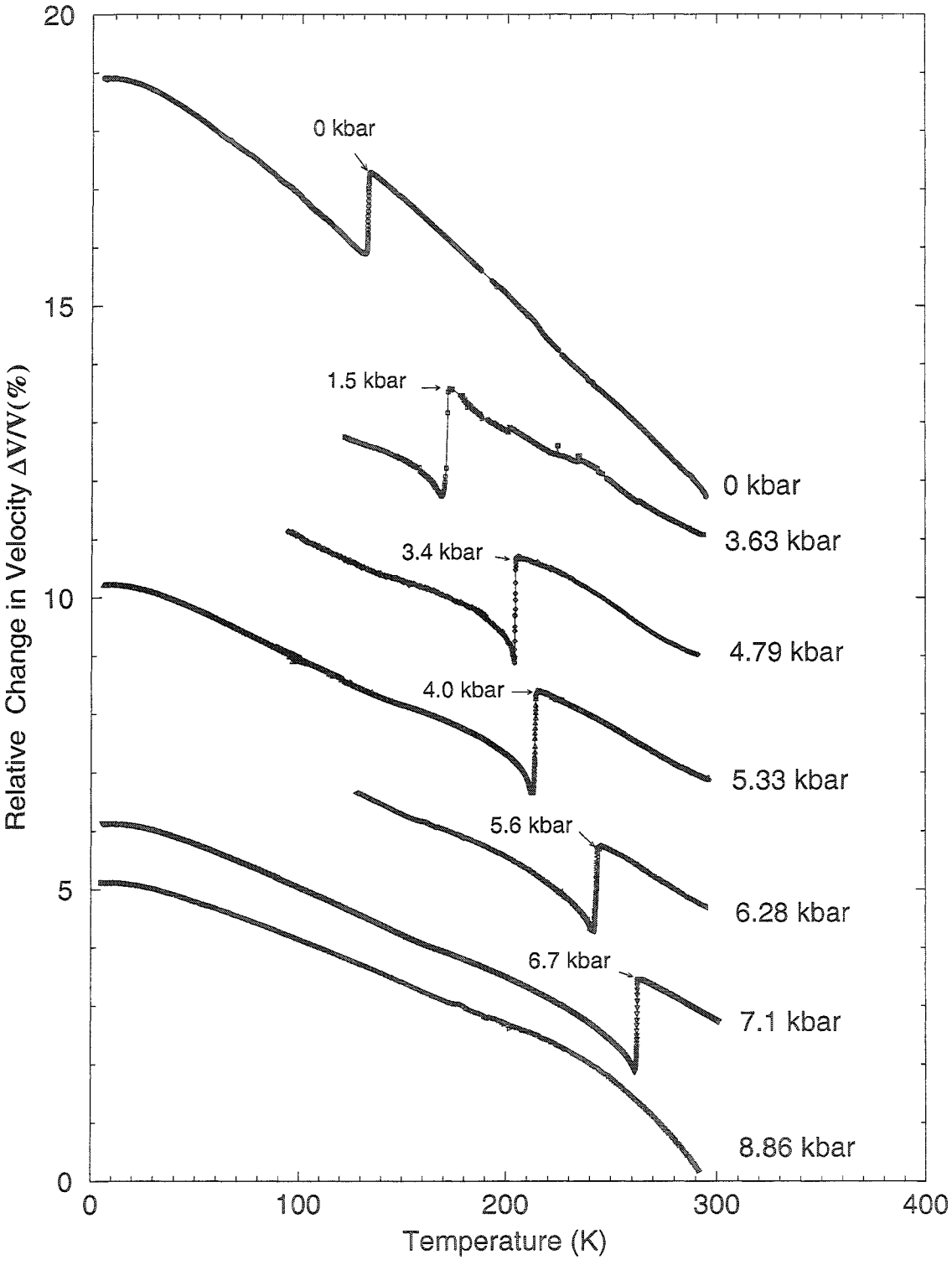

Figure 4.13: Temperature dependence of the sound velocity of longitudinal waves propagating along the z-axis at different pressures.

the curves around the minimum of the velocity does change with pressure. As this phase transition is a ferroelastic transition, that means that domains form in the low temperature phase. Consequently, the change in the shape of the curves in this phase might indicate that the domains pattern near the transition temperature is modified by pressure. The figure also shows that in the high temperature phase the slopes of the curves obtained at pressures larger than 1 *bar* are different from that corresponding to the ambient pressure. This is due to the fact that those measurements are not realized at constant pressure.

In Fig. 4.13, we present the critical temperatures obtained using cooling processes. Considering that the temperature sensor is mounted on the outside wall of the pressure cell, the transition temperatures obtained from these measurements are smaller than the real ones due to the temperature gradient. However, the difference is estimated to be less than 0.5 K. Using the results presented in Fig. 4.13, we can easily derive the temperature-pressure phase diagram, which is shown in Fig. 4.14. We identify two phases between 4 K and 300 K with pressure extending to 7 $kbar$. As shown in Fig. 4.14, the region above the curve corresponds to the monoclinic phase while the region below the curve corresponds to the tetragonal phase. The boundary of these two phases can be well represented by a linear relation. It shows that the transition temperature, T_c, increases rapidly with pressure at a rate of 19 ± 1 $K/kbar$.

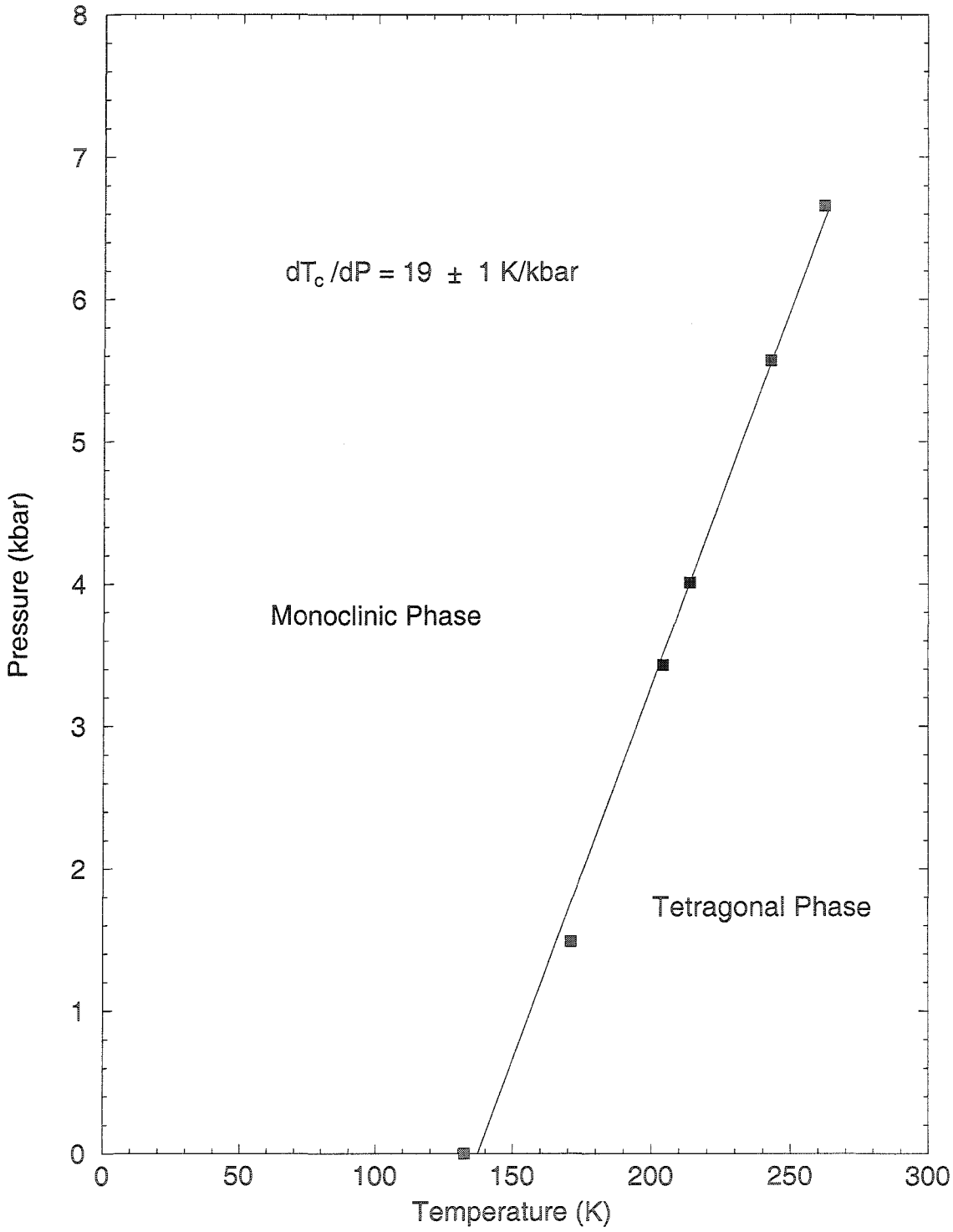

Figure 4.14: Temperature-pressure phase diagram for $Rb_4LiH_3(SO_4)_4$ crystals.

Chapter 5

Theoretical Model

Phase transitions can be analyzed using various types of theoretical methods. One of them, the Landau mean field theory, is a simple but powerful thermodynamic model by which many features associated with a phase transition can be described. So far, several Landau models [10, 12, 14, 19, 21] have been put forward intending to explain the phase transition observed for $Rb_4LiH_3(SO_4)_4$, however, none of them seem to be fully compatible with the experimental observations. For this reason, we dedicate this chapter to the elaboration of a Landau model consistent with the experimental results. In order to test our model, we compared the theoretical predictions with the elastic constants obtained as a function of temperature and pressure. Naturally, we begin this chapter by given a rudimentary description of the Landau mean field theory. A detailed development can be found in "The Landau Theory of Phase Transitions" written by J.C. Tolédanno et al. [65].

5.1 Phase Transition and Landau Theory

5.1.1 Phase Transition

A phase is characterized by thermodynamic quantities that include the volume V, pressure P, temperature T, and the Gibbs free energy G. When the free energy corresponds to a minimum, under some specified thermodynamic conditions, the phase associated with those conditions is normally stable. As temperature, pressure or any other external variable acting on a system is changed, the free energy of the system also changes. Whenever such variation in the free energy is associated with structural modifications, a phase transition is said to occur [63]. Depending on the type of modifications, the phase transition is normally classified as first, second, or higher order. This classification scheme is, in fact, based on which of the thermodynamic properties undergo a discontinuous variation at the critical temperature or pressure. In general, a transition is said to be of the same order as the lowest derivative of the Gibbs free energy that shows a discontinuous change at the critical temperature or pressure. From Thermodynamics, we know that the total derivative of the Gibbs free energy takes the form

$$dG = VdP - SdT \ . \tag{5.1}$$

Thus, from Eq. 5.1 we immediately obtain that the partial derivatives of the Gibbs energy give the volume

$$V = \left(\frac{\partial G}{\partial P}\right)_T \tag{5.2}$$

and the entropy

$$S = -\left(\frac{\partial G}{\partial T}\right)_P \ . \tag{5.3}$$

Hence, a phase transition is first order if a discontinuous change in the volume V or the entropy S is observed during the transition. From equation 5.2, we see that the

volume thermal expansivity α can be expressed in terms of the second derivatives of the Gibbs energy as

$$\alpha = \frac{1}{V}\left(\frac{\partial V}{\partial T}\right)_p = \frac{1}{V}\frac{\partial^2 G}{\partial P \partial T} . \tag{5.4}$$

Moreover, making use of $dQ = TdS$, the specific heat capacity at constant pressure C_P can be expressed as

$$C_P = T\left(\frac{\partial S}{\partial T}\right)_p = -T\left(\frac{\partial^2 G}{\partial T^2}\right)_P . \tag{5.5}$$

Thus, a phase transition is said to be second order if a discontinuity in the specific heat capacity C_p or the volume thermal expansivity α is observed [63]. Actually, many transitions are truly mixed order, exhibiting features of both first and second order.

5.1.2 Landau Theory

Landau theory is a macroscopic, thermodynamic theory which is extensively used to describe phase transitions without giving any information about the microscopic causes of the transition. It is applicable to phase transitions in which a symmetry change occurs whenever the point group of the low symmetry phase is a subgroup of the high symmetry phase. The theory is based on the introduction of an order parameter which is some quantity that differentiates both phases. When the order parameter takes on a value equal to zero, the crystal symmetry is that of the high symmetry phase. As soon as the order parameter takes on a nonzero value, the symmetry is reduced to that of the low symmetry phase [52]. What differentiates a first and a second order transition is that the order parameter varies continuously across the transition for a second order transition, while for the first order transition the order parameter jumps discontinuously at the critical temperature or pressure. Landau

assumes that the excess free energy G_e of the low temperature phase relative to the high temperature phase can be expanded in a power series of this order parameter Q, such that

$$G_e = \alpha_1 Q + \frac{1}{2}\alpha_2 Q^2 + \frac{1}{3}\alpha_3 Q^3 + \frac{1}{4}\alpha_4 Q^4 + \cdots \tag{5.6}$$

where the coefficients may depend on parameters such as temperature, pressure, etc.. The order parameter Q is zero in the high symmetry phase and scaled to unity in the low symmetry phase well below the transition temperature or pressure. Therefore, in the vicinity of the transition, the contribution of the higher degree terms to the free energy are considerably small. Depending on the nature of the phase transition, the expansion is sometime extended up to the sixth order term. Moveover, as we will see later, some terms in the power series should vanish as required by symmetry considerations.

As the transition studied in this project belongs to the second order type, our discussion about the application of Landau theory is limited to this type of transition. Since the order parameter varies continuously through the transition for this class of phase transitions, terms with the powers of Q greater than four in the expansion of the excess free energy can be neglected for conventional second order phase transitions. Moreover, considering that changing the sign of Q does not change the state of the body [63], the excess free energy G_e must also be invariant under that operation. Thus, all coefficients associated with an odd power in Q must be set to zero, such that the excess free energy reduces to

$$G_e = \frac{1}{2}\alpha_2 Q^2 + \frac{1}{4}\alpha_4 Q^4 \ . \tag{5.7}$$

As stated previously, a phase is stable only if the free energy corresponds to a minimum. Therefore, in order to have global stability, the coefficient α_4 must be positive. This ensures that as we increase Q to large values, the free energy increases. Using

that the free energy corresponds to a minimum, the conditions

$$\frac{\partial G_e}{\partial Q} = \alpha_2 Q + \alpha_4 Q^3 = 0 \tag{5.8}$$

$$\frac{\partial^2 G_e}{\partial Q^2} = \alpha_2 + 3\alpha_4 Q^2 > 0 \tag{5.9}$$

must be satisfied. As $Q = 0$ in the high symmetry phase, it follows from Eq. 5.9 that $\alpha_2 > 0$ in this phase. While in the low symmetry phase, owing that $Q > 0$ and $\alpha_4 > 0$, Eq. 5.8 leads to $\alpha_2 < 0$. Since α_2 changes sign across the transition point, Landau made the assumption that

$$\alpha_2 = a\ (T - T_0) \tag{5.10}$$

where a and T_0 are positive constants. Thus, the excess free energy takes the form

$$G_e = \frac{1}{2}a(T - T_0)Q^2 + \frac{1}{4}\alpha_4 Q^4\ . \tag{5.11}$$

A plot of G_e as a function of Q for various temperatures is given in Fig. 5.1. As shown in this graph, for $T \geq T_0$ the excess free energy is minimum at $Q = 0$, while for $T < T_0$ it reaches its minimum at $Q > 0$. Differentiating Eq. 5.11 with respect to Q and setting the derivative equal to zero shows that, at equilibrium

$$Q = 0, \qquad T > T_0 \tag{5.12}$$

$$Q = \sqrt{\frac{a}{\alpha_4}(T_0 - T)}, \qquad T < T_0 \tag{5.13}$$

The first solution corresponds to the high symmetry phase, while the second solution corresponds to the low symmetry phase. From the second solution, we see that T_0 corresponds to a critical temperature (T_c) at which the order parameter appears. Therefore, in the low temperature phase the order parameter are often expressed as

$$Q = \sqrt{\frac{a}{\alpha_4}(T_c - T)} \tag{5.14}$$

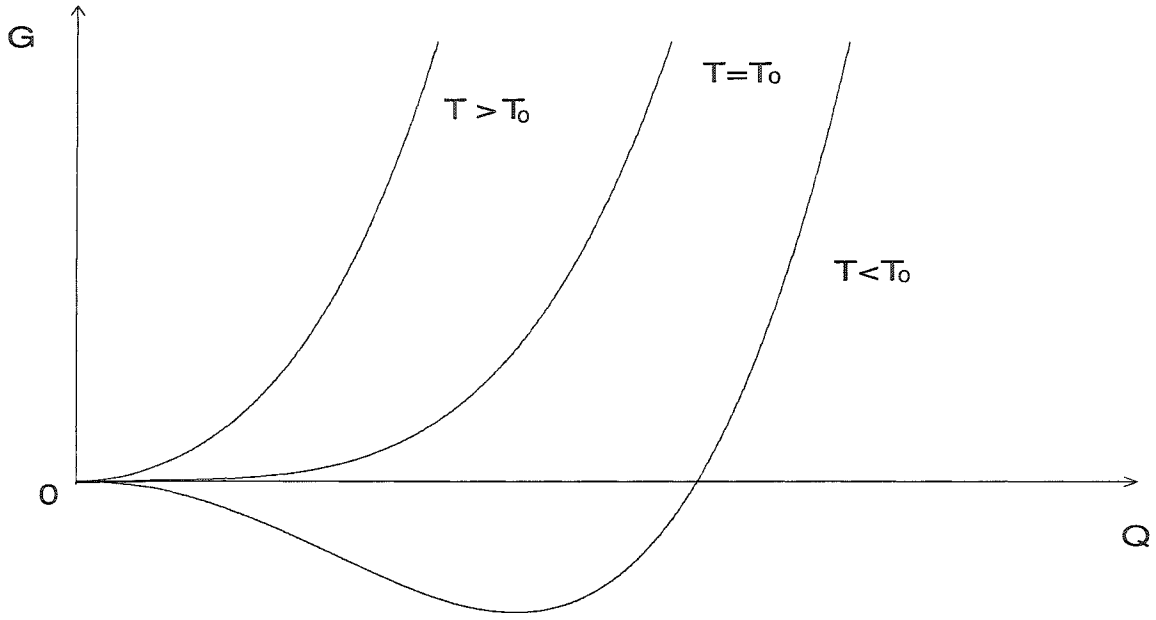

Figure 5.1: A schematic plot of the free energy G as a function of the order parameter Q for various temperatures (Eq. 5.11).

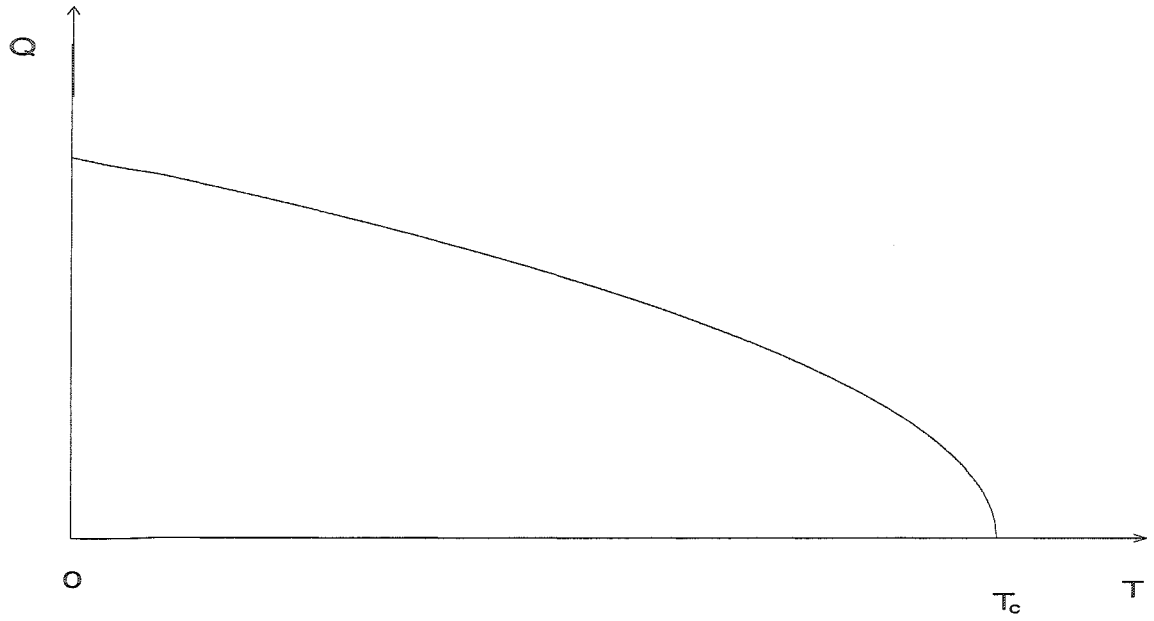

Figure 5.2: Order parameter as a function of temperature obtained from a mean field model (Eq. 5.12 and 5.13).

A typical curve of the order parameter against temperature is given in Fig. 5.2. From this figure, we see that the order appears at $T = T_c$ and its magnitude varies as the temperature further deceases.

5.1.3 Expansion of the Landau Model

So far, we have presented the free energy expansion in terms of the order parameter Q. Such an expansion is useful in order to derive a phase diagram, however, our goal is to derive the elastic constants from the free energy. Therefore, the free energy should include the elastic energy which arises from the appearance of spontaneous strains in the low temperature phase. These spontaneous strains can be obtained by considering the coupling between the strains and the order parameter. In that

case, the appropriate Landau free energy expansion can be expressed in the form of a convergent power series including several distinct contributions due to particular physical mechanisms, such that

$$F(Q, e_i, P) = F_1(Q) + F_2(e_i) + F_3(Q, e_j) + F_4(P, e_{kk}) \ . \tag{5.15}$$

The first term $F_1(Q)$ is the usual Landau free energy which depends on the Landau order parameter corresponding to Eq. 5.11. The second term $F_2(e_i)$ is the elastic energy while the third term $F_3(Q, e_j)$ takes into account the coupling between the order parameter and the strains. The last term $F_4(P, e_{kk})$ is related to the work done on the crystal by an external pressure P. Using this free energy, the elastic constants can be calculated using [33]

$$C_{mn} = \frac{\partial^2 F}{\partial e_m \partial e_n} - \frac{\partial^2 F}{\partial Q \partial e_m} \left(\frac{\partial^2 F}{\partial Q^2}\right)^{-1} \frac{\partial^2 F}{\partial e_n \partial Q} \ . \tag{5.16}$$

5.2 Landau Analysis of the Experimental Results

As mentioned in chapter 1, the phase transition we observed for $Rb_4LiH_3(SO_4)_4$ belongs to second order and the symmetry change through the transition is $4 \rightarrow 2$ [11]. As the point groups satisfy the group-subgroup relation, a Landau model can be used to describe the observed phase transition. Actually, several Landau models for this phase transition have already been presented by other groups [10, 12, 14, 19, 21]. However, none of them can satisfactorily explain the observed results. According to group theory, for a $4 \rightarrow 2$ type transition, the order parameter should have the same symmetry as the strain components $(e_1 - e_2)$ and e_6 [24]. If the order parameter coincides with the strains, the transition should be classified as a proper ferroelastic

transition, otherwise it corresponds to a pseudoproper ferroelastic transition. Among the models mentioned in this paragraph, those presented by the groups [12, 14, 19] are based on the assumption that the phase transition is a proper ferroelastic phase transition. These models cannot explain the variation of C_{11} observed at T_c. The models presented by the groups [10, 21] are based on the assumption that the phase transition has a pseudoproper character. These two models are not fully compatible with experimental observations either. The one proposed by [10] predicts that C_{66} gets softened (which is inconsistent with the experimental results, see Fig. 4.7). The other [21] does not consider the coupling terms involving e_3 and, therefore, cannot explain the variations observed on C_{33}.

During a proper ferroelastic transition, one normally observes a substantial elastic anomaly on one of the elastic constants, or a combination of elastic constants (soft elastic mode), which goes to zero as the transition point is approached from either side. Typically, for proper ferroelastic transitions this soft elastic mode varies linearly with temperature over a wide temperature range. However, our measurements indicate that the temperature dependence of $(C_{11} - C_{12})/2$ (see figure 4.8), which shows incomplete softening, does not display a well defined linear dependence. Consequently, based on this last observation, we will assume that the transition corresponds to a pseudoproper ferroelastic transition. Thus, the order parameter is a physical quantity that is different from the strains, however it must have the same symmetry as $(e_1 - e_2)$ and e_6 in order to describe a $4 \rightarrow 2$ symmetry change.

In writing the explicit form of the Landau free energy, we must take into account the symmetry properties of the crystal. As the atomic configuration of the crystal remains unaltered under a symmetry operation of the high symmetry phase, the free energy must also be invariant under the same symmetry operation. Thus, all terms considered in the free energy must be invariant under the symmetry operations of the

strains	e_1 (e_{xx})	e_2 (e_{yy})	e_3 (e_{zz})	e_4 (e_{yz})	e_5 (e_{xz})	e_6 (e_{xy})
C_4^1	e_2	e_1	e_3	$-e_5$	e_4	$-e_6$

Table 5.1: Transformations of the strains under the operation of the elements of point group 4.

high symmetry phase. In the case of $Rb_4LiH_3(SO_4)_4$, the point group for the high symmetry phase is 4 [11]. One of the symmetry operation that must be considered is C_4^1, which corresponds to a rotation of 90^0 relative to the z-axis. The symmetry properties of the spontaneous strains under the operation of C_4^1 are given in Table 5.1. As e_{11} transforms as a x^2 function, e_{22} as y^2, e_{33} as z^2, e_{44} as yz, e_{55} as xz and e_{66} as xy, the strains are sometimes written as e_{xx}, e_{yy}, e_{zz}, e_{yz}, e_{xz}, e_{xy}, respectively. Moreover, we know that the transformation of the order parameter Q under the operation of C_4^1 must be the same as e_6 or $(e_1 - e_2)$. Thus, the symmetry invariant form of the free energy associated with the order parameter is

$$F_1(Q) = \frac{1}{2}\,\alpha_2\,Q^2 + \frac{1}{4}\,\alpha_4\,Q^4 \tag{5.17}$$

where $\alpha_2 = a\,(T - T_0)$, as given previously. It is worthwhile to mention that the quadratic and quartic terms are always allowed by symmetry. From Eq. 2.1.3, we have that the elastic energy for the tetragonal phase (4) is

$$\begin{aligned} F_2(e_i) &= \tfrac{1}{2}\,C_{11}\,(e_1^2 + e_2^2) + \tfrac{1}{2}\,C_{44}\,(e_4^2 + e_5^2) + \tfrac{1}{2}\,C_{33}\,e_3^2 + \tfrac{1}{2}\,C_{66}\,e_6^2 \\ &+ C_{12}\,e_1\,e_2 + C_{13}\,(e_1 + e_2)\,e_3 + C_{16}\,(e_1 - e_2)\,e_6 \end{aligned} \tag{5.18}$$

where the elastic constants refer to their values at temperatures above T_c. It is easy to check that all terms in Eq. 5.18 are invariant with respect to C_4^1. The lower coupling terms must at least include

$$F_3(Q, e_j) = \beta\,Q\,(e_1 - e_2) + \gamma\,Q\,e_6 + \delta\,Q^2\,e_3 + \lambda\,Q^2\,(e_1 + e_2) \tag{5.19}$$

where the coefficients β, γ, δ, and λ are constants, whose values will be determined later. In this model, we only consider the dominant coupling terms. Based on the fact that C_{44} (or C_{55}) is slightly affected by the phase transition, we know that the coupling between the order parameter and the strain e_4 (or e_5) is negligible. That explains why e_4 and e_5 do not appear in the above expression. Since the order parameter Q has the same symmetry as the strains e_6 and $e_1 - e_2$, the two linear-linear coupling terms ($\beta\ Q\ (e_1 - e_2)$ and $\gamma\ Q\ e_6$) automatically transform like Q^2, and therefore are allowed by symmetry. From Table 5.1, we see that e_3 and $e_1 + e_2$ are invariant under the symmetry operation, so the last two quadratic-linear terms are also allowed. Finally, the work associated with an external pressure can be expressed as

$$F_4(P, e_{kk}) = P\ (e_1 + e_2 + e_3) \tag{5.20}$$

where P is the pressure and e_1, e_2, e_3 are strains affected by the hydrostatic pressure. It is easy to check that this expression is invariant under the symmetry operation as well. Combining these four expressions, we obtain the free energy,

$$\begin{aligned} F &= \tfrac{1}{2}\ \alpha_2\ Q^2 + \tfrac{1}{4}\ \alpha_4\ Q^4 \\ &+ \tfrac{1}{2}\ C_{11}\ (e_1^2 + e_2^2) + \tfrac{1}{2}\ C_{44}\ (e_4^2 + e_5^2) + \tfrac{1}{2}\ C_{33}\ e_3^2 + \tfrac{1}{2}\ C_{66}\ e_6^2 \\ &+ C_{12}\ e_1\ e_2 + C_{13}\ (e_1 + e_2)\ e_3 + C_{16}\ (e_1 - e_2)\ e_6 \\ &+ \beta\ Q\ (e_1 - e_2) + \gamma\ Q\ e_6 + \delta\ Q^2\ e_3 + \lambda\ Q^2\ (e_1 + e_2) \\ &+ P\ (e_1 + e_2 + e_3). \end{aligned} \tag{5.21}$$

which can be used to calculate the elastic constants and the strains associated with the phase transition. Under equilibrium conditions, we know that the free energy must correspond to a minimum. Therefore, we have that

$$\frac{\partial F}{\partial e_i} = 0 \tag{5.22}$$

where i ranges from 1 to 6. From these equations, we find that the strains in the low temperature phase can be expressed in terms of the order parameter Q and pressure

ζ	$C_{11} + C_{12}$
ε	$C_{11} - C_{12}$
b_1	$\beta\ C_{66}(2\ C_{13}^2 - \zeta\ C_{33}) + \gamma\ C_{16}\ (\zeta\ C_{33} - 2\ C_{13}^2)$
b_2	$\delta\ C_{13}\ (\varepsilon\ C_{66} - 2\ C_{16}^2) + \lambda\ C_{33}\ (2\ C_{16}^2 - \varepsilon\ C_{66})$
b_3	$\varepsilon\ C_{13}\ C_{66} - \varepsilon\ C_{33}\ C_{66} - 2\ C_{16}^2\ (C_{13} - C_{33})$

Table 5.2: Expressions for the parameters used in the equations of the strains as a function of Q and P.

P as

$$e_1(Q,P) = \frac{b_1 Q + b_2 Q^2 + b_3 P}{(2C_{13}^2 - \zeta C_{33})(2C_{16}^2 - \varepsilon C_{66})} \tag{5.23}$$

$$e_2(Q,P) = \frac{-b_1 Q + b_2 Q^2 + b_3 P}{(2C_{13}^2 - \zeta C_{33})(2C_{16}^2 - \varepsilon C_{66})} \tag{5.24}$$

$$e_3(Q,P) = \frac{(\delta\zeta - 2\lambda C_{13})Q^2 + (\zeta - 2C_{13})P}{2C_{13}^2 - \zeta C_{33}} \tag{5.25}$$

$$e_4(Q,P) = 0 \tag{5.26}$$

$$e_5(Q,P) = 0 \tag{5.27}$$

$$e_6(Q,P) = \frac{(2\beta C_{16} - \varepsilon\gamma)Q}{\varepsilon C_{66} - 2C_{16}^2} \tag{5.28}$$

where the parameters ζ, ε, b_1, b_2 and b_3 are given in Table 5.2. From the first two equations, we see that

$$e_1 - e_2 = \frac{2b_1 Q}{(2C_{13}^2 - \zeta C_{33})(2C_{16}^2 - \varepsilon C_{66})} \tag{5.29}$$

is indeed proportional to the order parameter as well as e_6 (see Eq. 5.28). This is consistent with the statement that the order parameter has the same symmetry as $e_1 - e_2$ and e_6. Minimizing the free energy with respect to Q, we obtain that

$$\alpha_2\ Q + \alpha_4\ Q^3 + \beta\ (e_1 - e_2) + \gamma\ e_6 + 2\ \delta\ e_3\ Q + 2\ \lambda\ (e_1 + e_2)\ Q = 0\ . \tag{5.30}$$

Combining equations 5.23-5.28 with Eq. 5.30 and making use the relation $\alpha_2 = a\ (T - T_0)$, it is not difficult to find the critical temperature at which the order parameter vanishes. Since this expression is too long, it is not shown here. However, taking the derivative of T_c with respect to P, we find that the rate at which the critical temperature changes with pressure is given by

$$\frac{dT_c}{dP} = \frac{2\gamma(C_{11} + C_{12} - 2C_{13}) - 4\delta(C_{13} - C_{33})}{a(C_{11} + C_{12})C_{33} - 2aC_{13}^2} \ . \tag{5.31}$$

As the value of dT_c/dP has been measured ($dTc/dP = 19\ K/kbar$), we can use Eq. 5.31 to fix the value of one of the adjustable coefficients. Though the expression for T_c with $P \neq 0$ is complicated, the expression under normal pressure condition is given by

$$T_c = T_0 + \frac{\gamma(4\beta C_{16} - \gamma\varepsilon) - 2C_{66}\beta^2}{a(2C_{16}^2 - \varepsilon C_{66})} \ . \tag{5.32}$$

The equation above shows that due to the coupling between the order parameter and the spontaneous strains, the transition temperature has been shifted from T_0 to T_c. As T_c is already known, this expression can be used to solve for another coefficient.

As shown in section 5.1.2, in the low temperature phase the order parameter depends on temperature. For simplicity, we only consider its temperature dependence at $P = 0\ kbar$. Thus, combining Eq. 5.23-5.28 with Eq. 5.30, we obtain that

$$Q(T) = \sqrt{\frac{a(2C_{13}^2 - \zeta C_{33})(\varepsilon C_{66} - 2C_{16}^2)}{(\varepsilon C_{66} - 2C_{16}^2)[\alpha_4(\zeta C_{33} - 2C_{13}^2) - 2(\zeta\delta^2 - 4C_{13}\delta\lambda + 2C_{33}\lambda^2)]}}\ (T - T_c) \tag{5.33}$$

where we have made use of Eq. 5.10 and Eq. 5.32. Comparing Eq. 5.33 with the second equation in 5.12, we see that the only difference is in their coefficients. Therefore, the temperature dependence of the order parameter in this model is described by a curve similar to that given in Fig. 5.2 and corresponds to a mean field order parameter. Inserting Eq. 5.33 into Eq. 5.23 – 5.28 for $P = 0$, we easily obtain the temperature

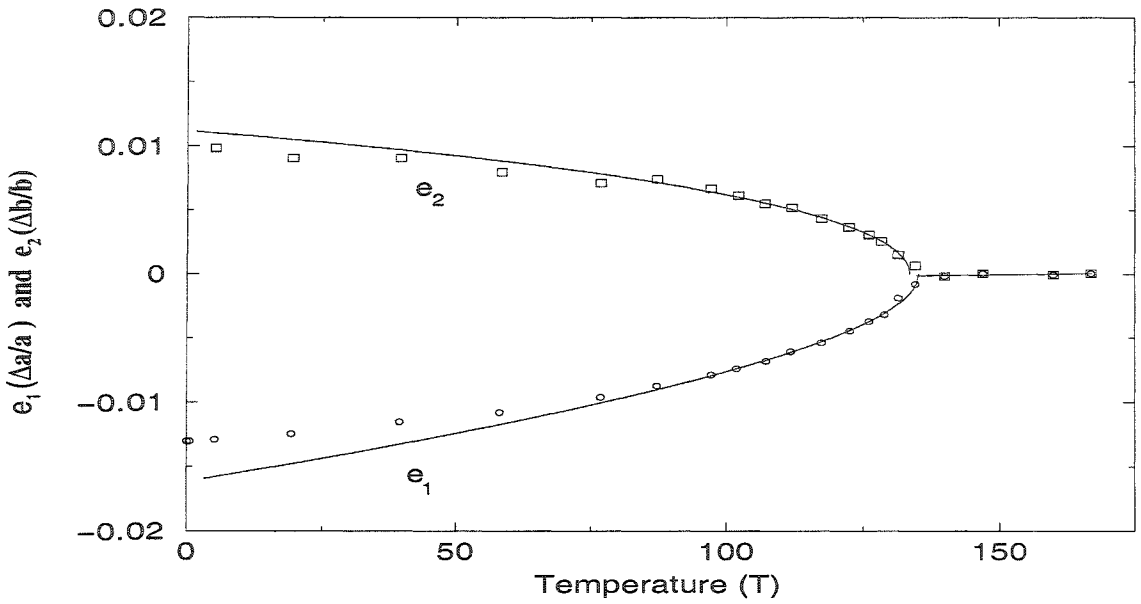

Figure 5.3: Temperature dependence of the strains e_1 and e_2 for $Rb_4LiH_3(SO_4)_4$. The circle and square symbols represent the data obtained by B. Mróz et al. [6], while the solid line are the fits of these data.

dependence of the strains. By fitting the experimental data for the strains using these later relations, all adjustable coefficients can be determined. Our fits and the experimental data reported by B. Mróz et al. [6] are presented in Fig. 5.3–5.4. In the process, we have made use of Eq. 5.31 and Eq. 5.32 as well as the convention that $Q = 1$ at $0\ K$. The coefficients obtained that way are given in Table 5.2. Let add that in the low temperature phase, Landau models are expected to describe the features of a phase transition close to T_c. Therefore, the deviations between theory and experiment at low temperatures ($T/T_c < 0.4$) for e_1 and e_6 are not significant. As for e_3, considering the poor experimental data, no good agreement between theory and experiment is expected.

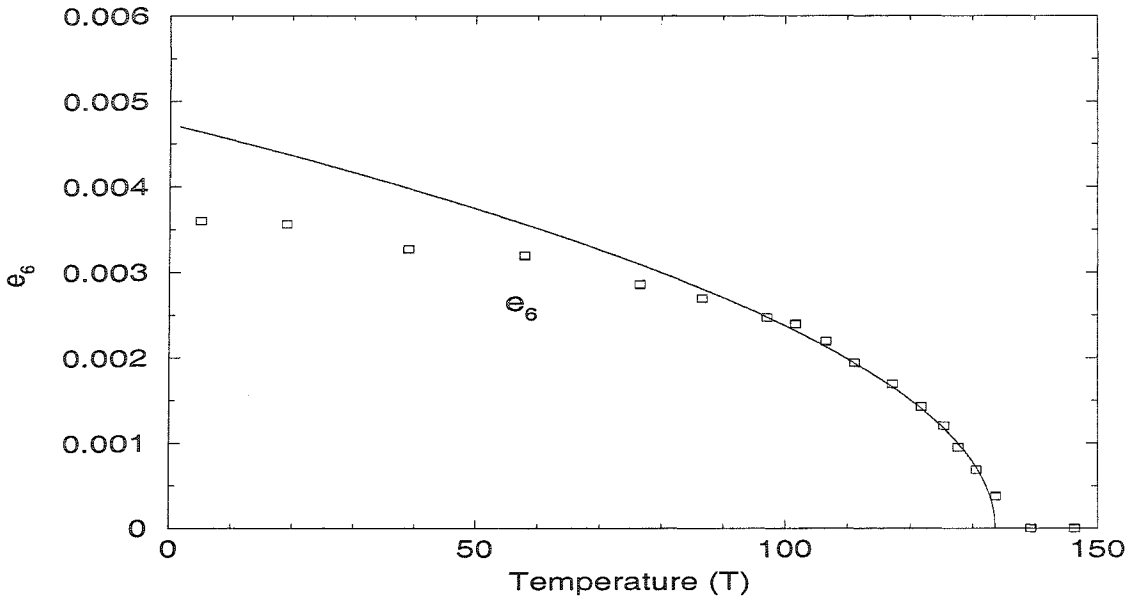

Figure 5.4: Temperature dependence of the strain e_6. Again the symbols and solid lines stand for the experimental data [6] and the fits, respectively.

β	γ	δ	λ	a	α_4
1.8	0.43	0.92	1.5	0.00068	0.11

Table 5.3: The values of the coefficients for this model. Each coefficient shown in this Table should be multiplied by 10^8.

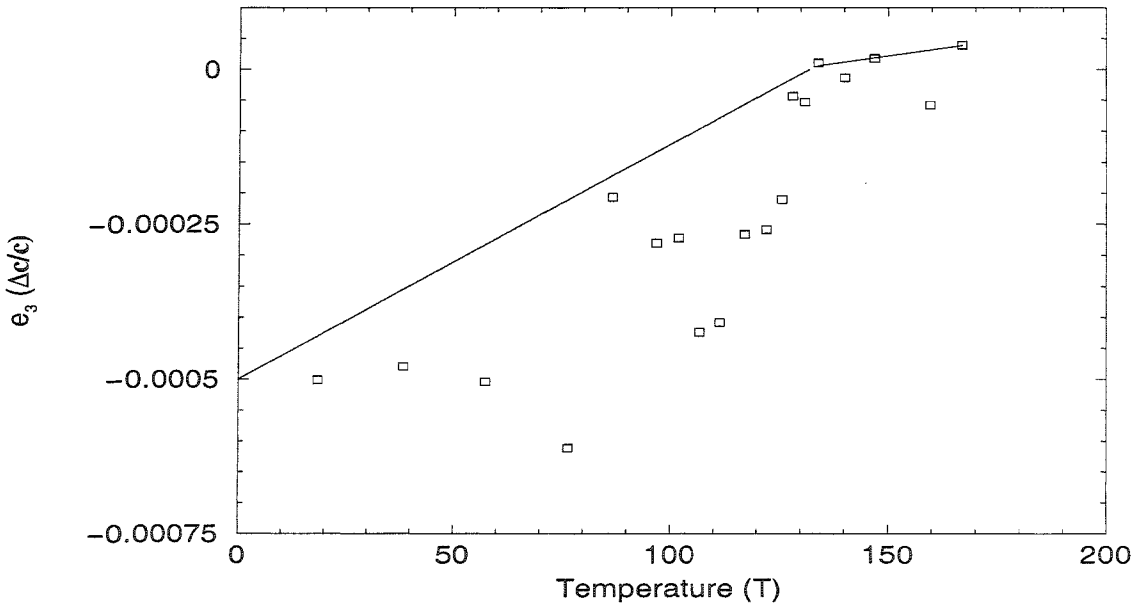

Figure 5.5: The fit of the temperature dependence of the strain e_3. The data is obtained by B.Mróz et al. [6].

C_{11}^0	C_{12}^0	C_{13}^0	C_{16}^0	C_{33}^0	C_{44}^0	C_{66}^0
3.65	2.05	0.50	0.20	4.30	0.68	1.10

Table 5.4: The values of the elastic constants used in this model as that corresponding to temperatures well above T_c. Each coefficient shown in this Table is in unit N/m^2 and its value should be multiplied by 10^{10}.

5.2.1 Soft Mode

Now that the free energy has been totally determined, the elastic constants can be obtained by using Eq. 5.1.3. The calculation is straight forward, but the results are often represented by long expressions. However, at $P = 0$ $kbar$, the elastic tensor corresponding to the tetragonal phase is given by

$$\begin{pmatrix} C_{11}^0 - \frac{\beta^2}{a\,(T-T_k)} & C_{12}^0 + \frac{\beta^2}{a\,(T-T_k)} & C_{13}^0 & 0 & 0 & C_{16}^0 - \frac{\beta\gamma}{a\,(T-T_k)} \\ C_{12}^0 + \frac{\beta^2}{a\,(T-T_k)} & C_{11}^0 - \frac{\beta^2}{a\,(T-T_k)} & C_{13}^0 & 0 & 0 & -C_{16}^0 + \frac{\beta\gamma}{a\,(T-T_k)} \\ C_{13}^0 & C_{13}^0 & C_{33}^0 & 0 & 0 & 0 \\ 0 & 0 & 0 & C_{44}^0 & 0 & 0 \\ 0 & 0 & 0 & 0 & C_{44}^0 & 0 \\ C_{16}^0 - \frac{\beta\gamma}{a\,(T-T_k)} & -C_{16}^0 + \frac{\beta\gamma}{a\,(T-T_k)} & 0 & 0 & 0 & C_{66}^0 - \frac{\gamma^2}{a\,(T-T_k)} \end{pmatrix} \tag{5.34}$$

with $T_k = T_c - (\gamma^2\ (C_{12}^0 - C_{11}^0) + 4\beta\gamma C_{16}^0 - 2\beta^2 C_{66}^0)/a\ (2(C_{16}^0)^2 + (C_{12}^0 - C_{11}^0)\ C_{66}^0)$. Here the elastic constants C_{ij}^0 refer to their values at temperatures well above T_c and are given in Table 5.4. Our model predicts that the elastic constants C_{11}, C_{12}, C_{16} and C_{66} more or less depend on temperature. The expressions for these elements can be used to fit the measured elastic constants presented in Chapter 4. Moreover, they are also used to calculate the temperature dependence of the effective elastic constant associated with the soft mode. The expression for this effective elastic constant can

be obtained by considering the strain components which have the same symmetry as the the order parameter, i.e. $e_1 - e_2$ and e_6. As their corresponding elastic constants are $(C_{11} - C_{12})/2$ and C_{66} respectively, the elastic constant submatrix associated with these strains takes the form

$$\begin{pmatrix} \frac{1}{2}(C_{11} - C_{12}) & C_{16} \\ C_{16} & C_{66} \end{pmatrix} . \tag{5.35}$$

The eigenvalues of this matrix give us the effective elastic constant of the soft mode, which is found to be

$$\rho\, V_s^2 = \frac{1}{2}\left(\frac{C_{11} - C_{12}}{2} + C_{66} - \sqrt{\left(\frac{C_{11} - C_{12}}{2} - C_{66}\right)^2 + 4C_{16}^2}\right) \tag{5.36}$$

where V_s stands for the sound velocity of the soft mode. Comparing with Eq. 4.2,

$$\rho V^2_{T_{[\bar{1}10][110]}} = \frac{1}{2}\left(C_{11} + C_{66} - \sqrt{(C_{12} + C_{66})^2 + 4C_{16}^2}\right) , \tag{5.37}$$

we see that though the transverse waves propagating along [110] and polarized perpendicularly to the z-axis shows the largest variations in velocity above T_c, its effective elastic constant is not equivalent to the soft mode (Eq. 5.36). This explains why the velocity of the transverse waves propagating along the [110] direction and polarized perpendicularly to the z-axis does not decrease to zero at T_c. In order to see if this soft mode does indeed show complete softening at T_c, we calculated its temperature dependence using the relevant elements of the matrix 5.34. The plot of the effective elastic constant of the soft mode as a function of temperature is presented in Fig. 5.6 along with the experimental data. Our calculations clearly show that the effective elastic constant for this soft mode goes to zero at T_c. Extrapolating the data to T_c, we find that the soft effective elastic constant takes the value $0.07 \times 10^{10}\ N/m^2$ at the transition temperature. As the uncertainty of the experimental result for this effective elastic constant is estimated between $0.05 \times 10^{10}\ N/m^2$ and $0.1 \times 10^{10}\ N/m^2$,

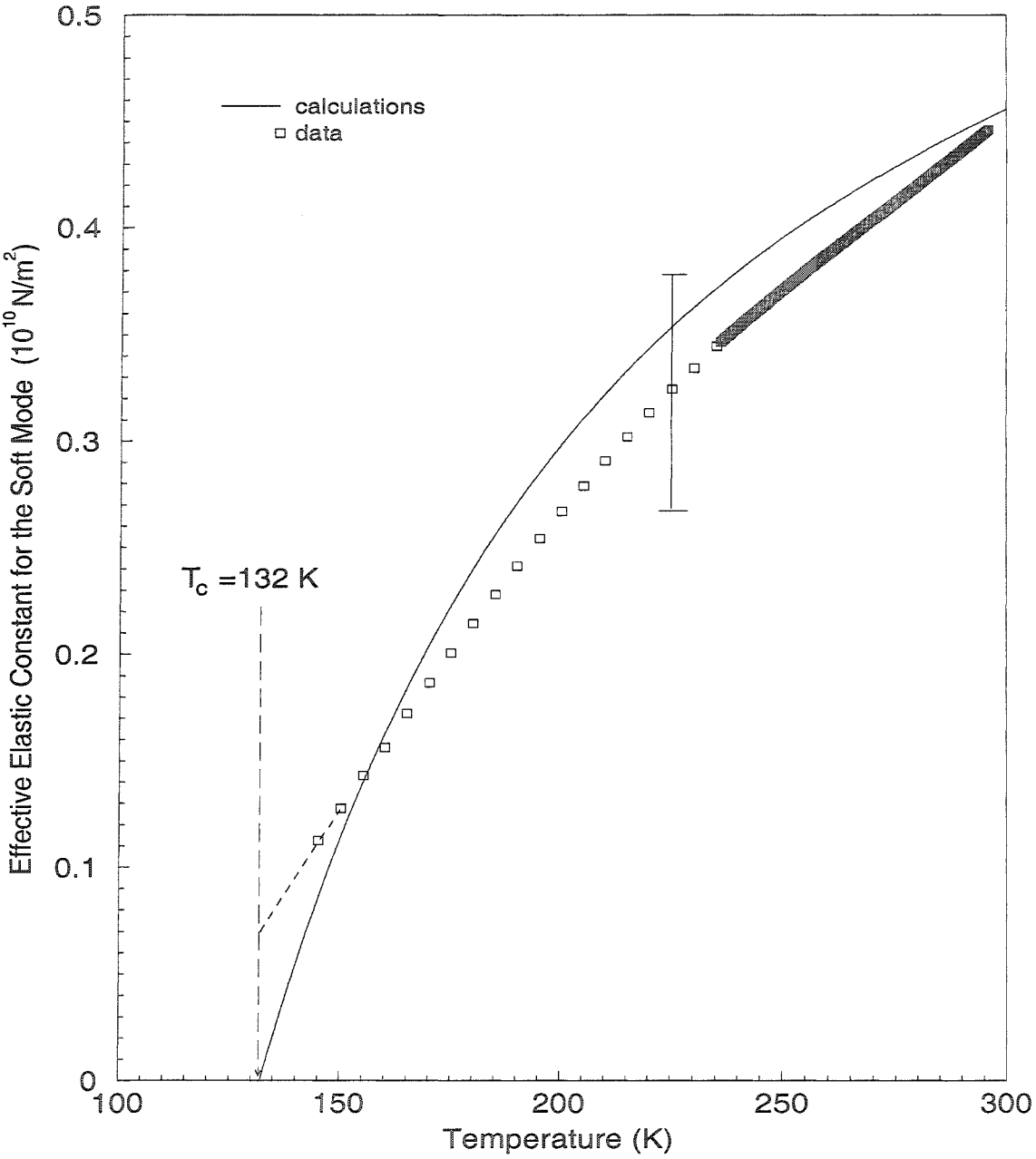

Figure 5.6: The temperature dependence of the effective elastic constant associated with the soft mode. The solid line represents the calculations using our model. The squares represent our experimental data. The vertical line segment represents the error bar.

our data can be considered in agreement with our calculations. However, this result contradicts the calculation given by Mróz et al. [14]. A close inspection reveals that their calculation is based on an inappropriate equation. In their paper, they used an asymmetric elastic constant submatrix

$$\begin{pmatrix} (C_{11} - C_{12}) & C_{16} \\ 2C_{16} & C_{66} \end{pmatrix} \tag{5.38}$$

which is obvious wrong because the elastic constant matrix is always symmetric (see Eq. 2.19). Based on this submatrix, they obtained an expression for the effective elastic constant of the soft mode

$$\rho\, V_s^2 = \frac{1}{2}\left(\frac{C_{11} - C_{12}}{2} + C_{66} - \sqrt{\left(\frac{C_{11} - C_{12}}{2} - C_{66}\right)^2 + 8C_{16}^2}\right) \tag{5.39}$$

which is naturally incorrect. Thus, we believe, that in the case of $Rb_4LiH_3(SO_4)_4$, the soft mode should show complete softening at T_c. According to Dieulesaint [60], for crystals that have the symmetry of point group 4, the propagating direction of the sound waves associated with the soft mode can be found in the (001) plane. Based on the slowness curves in the (001) plane, it is found that this direction can be calculated using equation [60]

$$tan\ 4\phi_0 = \frac{4C_{16}}{C_{11} - C_{12} - 2C_{66}} \tag{5.40}$$

where ϕ_0 refers to the angle between the propagating direction and the [110] direction. Based on our model, ϕ_0 is found to be equal to -5^0 at T_c. In another word, complete softening of the soft mode should be observed only along that direction.

5.2.2 Comparison of the Calculations with Experimental Data

As the elastic constants can be calculated from the Landau free energy, their experimental counterparts presented in Chapter 4 provide an appropriate data set for

testing our model. Due to the fact that the data are obtained using the equations corresponding to the tetragonal phase, the results for the monoclinic phase may not be accurate. For that reason, we focus our attention to the comparison relative to the tetragonal phase. In this section, we analyze only those elastic constants which are significantly affected by the phase transition, i.e. C_{11}, C_{33} and $(C_{11} - C_{12})/2$. The variations in the elastic constant is a consequence of anharmonic effects. Some of the anharmonic effect is associated with the soft mode, the rest is not. As the theoretical model only predicts the variations associated with the soft mode, before conducting the comparison, the variations caused by anharmonic effects (the normal anharmonic effect) not related to the soft mode need to be subtracted from the experimental data.

In the case where the external variable is the temperature, our model predicts that C_{33} is constant above T_c, see Fig. 5.7. That means that, for the tetragonal phase, there is no contribution of the soft mode on C_{33}. Therefore, the linear temperature dependence of C_{33} is obviously a result of the normal anharmonic effect (see Fig. 4.7). Subtracting the linear extrapolation, we obtain the variation associated with the soft mode for C_{33}. For C_{11}, Fig. 4.7 shows that it gets softened at temperatures well above T_c. Thus, in this case, the contribution of the normal anharmonic effect can only be derived from data obtained well above room temperature. Since those data is unavailable, we assume that the contribution of the normal anharmonic effect is the same as the one observed on C_{33}. Thus, we estimate the effect of the soft mode on C_{11} by subtracting a linear extrapolation similar to the one observed for C_{33}. The data obtained this way for C_{33} and C_{11} are shown in Fig. 5.7 along with the calculations based on our theoretical model. Both graphs show that our model agrees well with the experimental results for the high temperature phase. However, in the low temperature phase the predictions of the model deviate from the measurements significantly. The appearance of domains in this phase may explain, at least partially, the disagreement

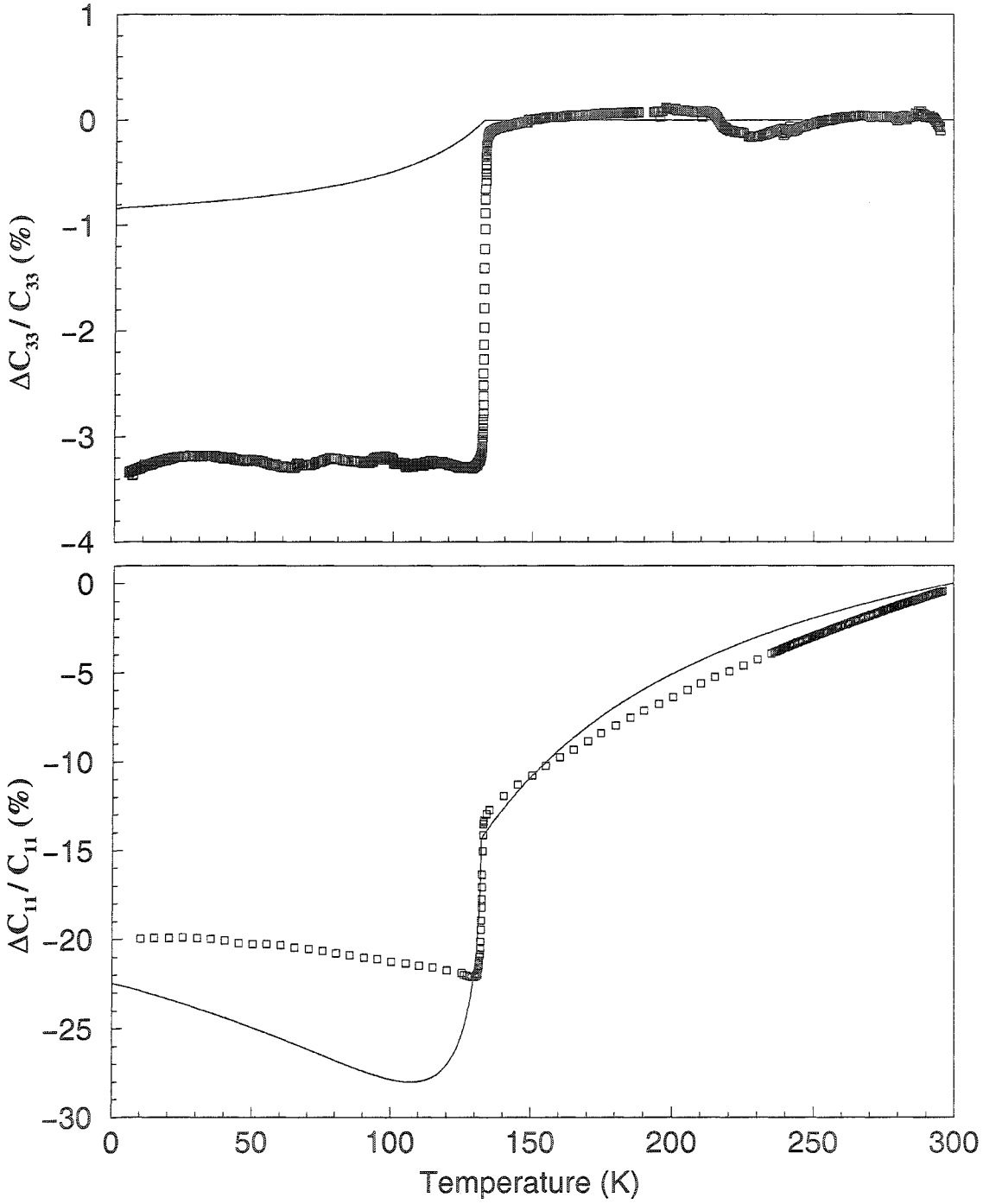

Figure 5.7: Temperature dependence of C_{33} and C_{11} at 0 *kbar*. The solid lines represent the fits obtained using our model. The squares represent data deduced from our measurements.

regarding the magnitude of the variation close to the transition. Besides, we should also keep in mind that the data for C_{11} is not accurate in this phase, so no full agreement is expected for this elastic constant. However, the disagreement for C_{33} may be also due to the fact that only lower coupling terms are considered in this model. As higher coupling terms involving e_3 are included, the fit might be improved.

As stated previously, the elastic constant combination $(C_{11} - C_{12})/2$ shows significant softening above T_c. It shows a nonlinear temperature dependence that convinces us that the observed transition belongs to a pseudoproper ferroelastic phase transition. For this reason, the calculated temperature dependence of $(C_{11} - C_{12})/2$ is compared with the experimental data. Considering that the data for the monoclinic phase is unavailable, the comparison is confined to the tetragonal phase. For this phase, the temperature dependence of $(C_{11} - C_{12})/2$ can be easily calculated using the elements of matrix 5.34, such that

$$\frac{1}{2}(C_{11}(T) - C_{12}(T)) = \frac{1}{2}(C_{11}^0 - C_{12}^0) - \frac{\beta^2}{a\,(T - T_k)}\,. \tag{5.41}$$

The plot of our calculation and the corresponding experimental data are presented in Fig. 5.8. In this case, as the normal anharmonic effect is not significant relative to the strong softening, we do not subtract any linear temperature dependence from the data. The figure shows that the model can roughly describe the temperature dependence of this elastic constant combination in the tetragonal phase. In principle, the fit can be improved by including high order coupling terms in our model. In the meantime, the normal anharmonic effect should be eliminated if we want to obtain a better agreement.

At constant temperature, the pressure dependence of the elastic constants can also be calculated from the free energy using Eq. 5.1.3. Thus, the experimental results of the elastic constants as a function of pressure provide supplementary data for testing

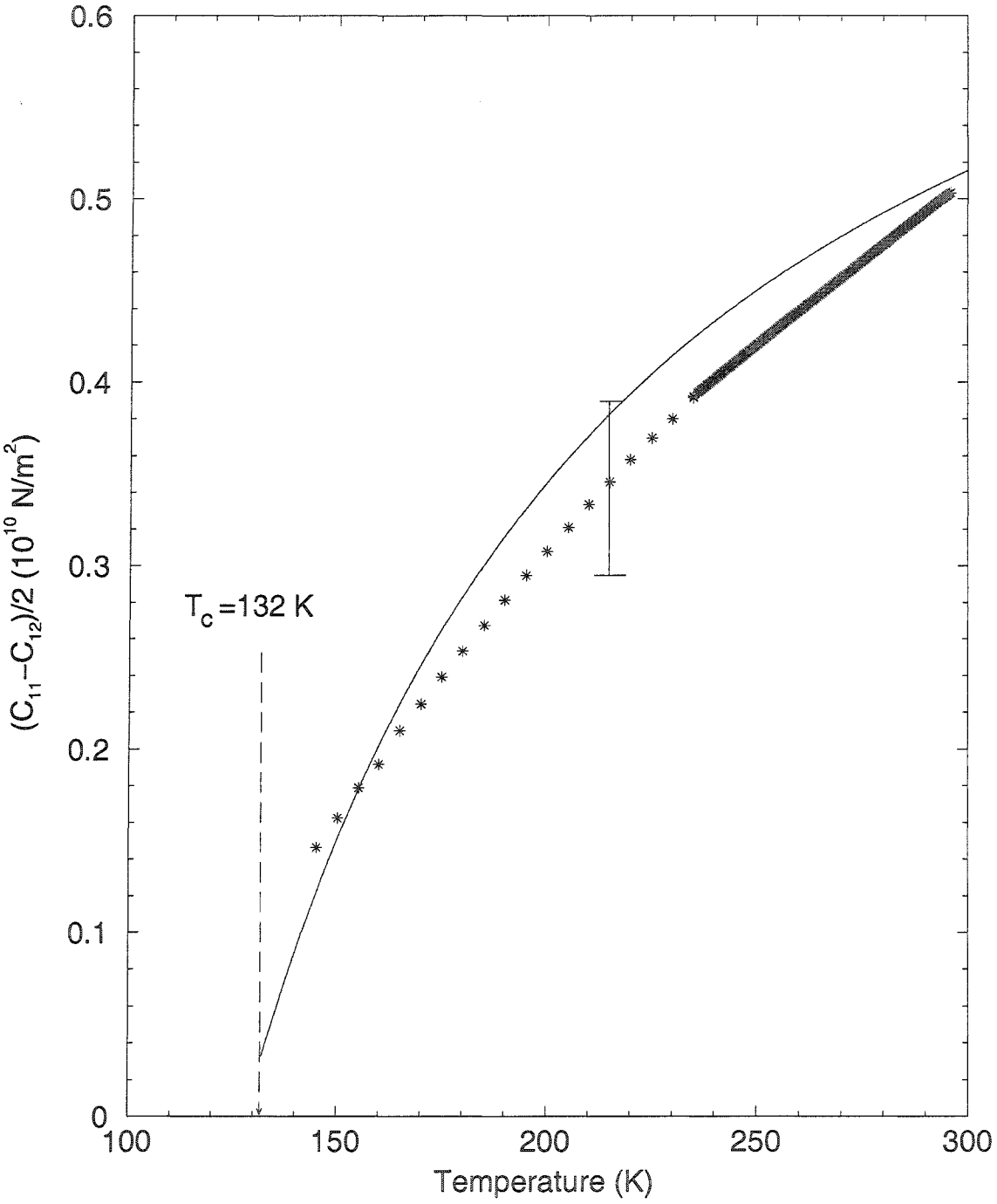

Figure 5.8: Temperature dependence of $(C_{11} - C_{12})/2$ at 0 *kbar*. Again, the solid line represents the fit using Eq. 5.41, while the square symbols represent the experimental data. The vertical line segment represents the error bar.

our model. In this case, the variations associated with the normal anharmonic effect is expected to be linear. Thus, the variations which are strictly associated with the soft mode can be obtained more rigorously by subtracting a proper linear extrapolation. In this sense, these data is more suitable for comparison. Actually, the variations associated with the soft mode for C_{33} and C_{11} have already been derived, see the insets of Fig. 4.9 and Fig. 4.10. Here, in Fig. 5.9, they are reproduced and compared with our calculations. Again, our model can adequately describe the pressure dependence of both C_{33} and C_{11} in the low pressure phase. We also see that in this case the fit for C_{11} agrees fully with the data except at pressures close to P_c. On the other hand, the predictions of our model disagree with the experimental results considerably in the monoclinic phase. The reason may still be that we only consider the lower coupling terms in our model. Besides, the appearance of the domains as well as the modifications of domains patterns with pressure may also account for part of the disagreements in this phase. For C_{11}, we should note that the data for the high pressure phase is not accurate. Thus, no full agreement is expected.

This simple model can explain the pressure behavior of $(C_{11}-C_{12})/2$ considerably well, see Fig. 5.10. Due to the limit of our data, the comparison has not been extended to higher pressure. In this case, we did not subtract any linear pressure dependence. Nevertheless, our calculation agrees fully with the data. This may indicate that the results of the normal anharmonic effect on C_{11} and C_{12} are the same, so they are cancelled out in the combination of $(C_{11}-C_{12})/2$. Our calculation clearly shows that this elastic constant combination exhibits incomplete softening at P_c. At this critical pressure, the calculated value is $0.08 \times 10^{10}\ N/m^2$, which is very close to the value obtained by extrapolating the experimental results obtained as a function of temperature. Our calculation also shows that $(C_{11}-C_{12})/2$ exhibits a nonlinear pressure dependence in the low pressure phase.

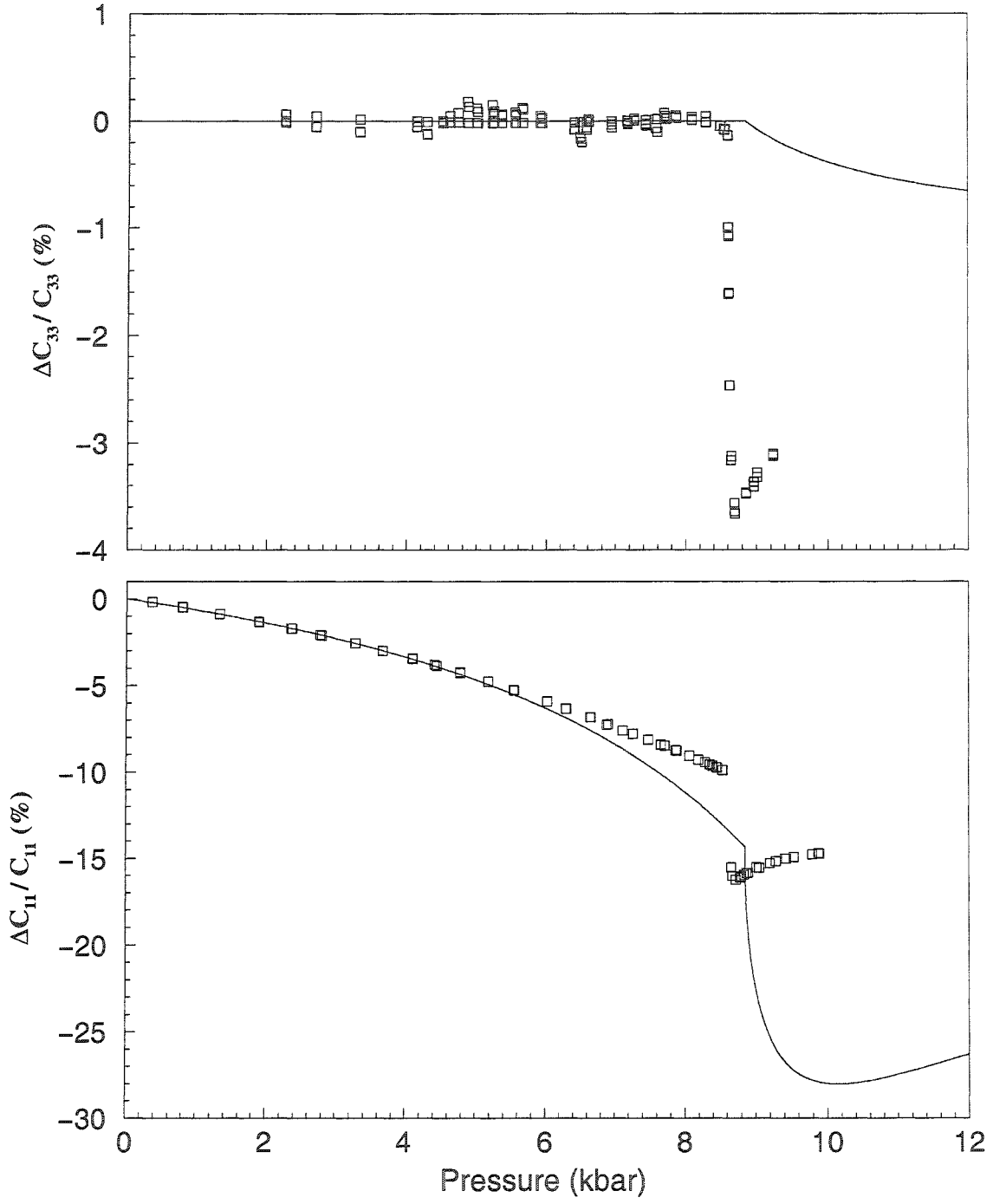

Figure 5.9: Pressure dependence of C_{33} and C_{11} at room temperature. The solid lines represent the fit. The squares represent the data obtained from our measurements.

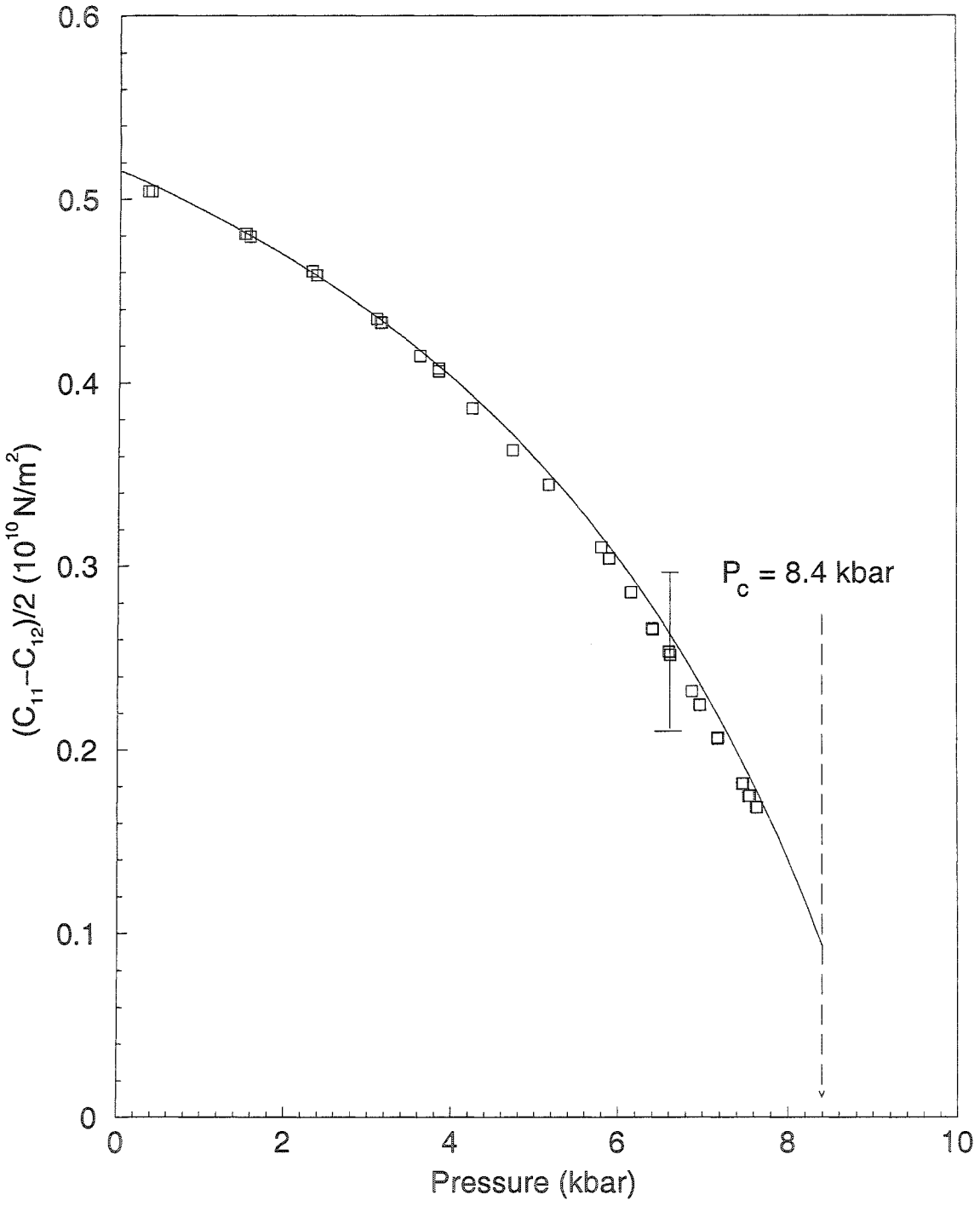

Figure 5.10: Pressure dependence of $(C_{11} - C_{12})/2$ at room temperature. Again, the solid line stands for the fit, while the squares represent the experimental data. The vertical line segment represents the error bar.

All these comparisons show that our model can appropriately describe the properties of $Rb_4LiH_3(SO_4)_4$. As we have seen, it can describe the temperature and pressure dependence of the elastic constants of this crystal though, for the monoclinic phase, due to the appearance of domains, the experimental results deviate from the calculations significantly. Of course, this is just a simple model. For better agreement, we need to elaborate the model a bit more. In particular, higher coupling terms $Q^2e_3^2$, $Q^2(e_1 - e_2)^2$ and $Q^2e_6^2$ can be added to the model. More importantly, we need to extract the intrinsic elastic constants for the monoclinic phase so that the validity of our model can be further tested in this phase.

Chapter 6

Conclusions

In this project, the temperature and pressure effect on the elastic properties of $Rb_4LiH_3(SO_4)_4$ has been investigated using an acoustic interferometer. The temperature and pressure ranges in our investigation were 4 K-300 K and 0 $kbar$-10 $kbar$, respectively. Our high resolution sound velocity measurements show that at ambient pressure $Rb_4LiH_3(SO_4)_4$ undergoes a phase transition at $T_c = 132 \pm 0.3$ K. This phase transition shows no thermal hysteresis on successive heating and cooling processes, confirming that it is a second order phase transition. In addition, at constant temperature $T = 300$ K, the occurrence of a phase transition is observed at a pressure of $P_c = 8.4 \pm 0.2$ $kbar$. Even in the absence of X-ray scattering measurements, in analogy to results obtained as a function of temperature, we can safely assume that the transition observed at P_c corresponds to $4 \rightarrow 2$ symmetry change.

It is well established that the monoclinic phase of $Rb_4LiH_3(SO_4)_4$ is ferroelastic. It is also known that two kinds of birefringent domains separated by mutually perpendicular walls exist in this phase [9]. However, the ratio of these two kinds of domains is not clearly demonstrated. Our results show that in the monoclinic phase the temperature dependence of the velocities of longitudinal waves propagating along x and

y directions are still equivalent. Based on this fact, we believe that the domains are roughly half and half in this phase. In order to derive the elastic constants, we need to measure the sound velocities along the crystal axes. However, if domains exist, the sound waves do not propagate along the same crystal axes in the different domains. In this case, the measured sound velocity cannot be used to accurately determine the elastic constants. Therefore, the elastic constants obtained for the monoclinic phase of $Rb_4LiH_3(SO_4)_4$ cannot be used to test the proposed theoretical model. In order to obtain appropriate data in this phase, we would need to measure the sound velocity using a single domain crystal.

In the range between 4 K and 300 K, we observed only one phase transition. The high and low temperature phase are known to have the tetragonal and monoclinic symmetry, respectively. Using the sound velocity measurements as a function of temperature under different pressures, the temperature-pressure phase diagram of $Rb_4LiH_3(SO_4)_4$ is obtained. The diagram covers the temperature range between 4 K and 300 K for pressures up to 7 $kbar$. The phase boundary is well described by a linear function. It is found that the transition temperature T_c increases rapidly with pressure at a rate of $dT_c/dP = 19 \pm 1\ K/kbar$.

The temperature and pressure dependence of five of the seven independent elastic constants of $Rb_4LiH_3(SO_4)_4$ are obtained. Our results regarding the temperature behavior of the elastic constants agree well with those reported by groups [14, 21]. The pressure dependence of the five elastic constants are obtained using the sound velocity measurements realized as a function of pressure at room temperature. Unfortunately, our sound velocity measurements could not go to high pressure ($P \geq 10\ kbar$), so the pressure dependence of the elastic constants at pressures well above P_c are not well defined. To our knowledge, we are the first to investigate the elastic constants as a function of pressure. It is found that the pressure behavior of the elastic constants

is similar to their temperature behavior. In spite of that, these results provide complementary data that can be used to test the Landau model. The variations in the elastic constant is a consequence of the anharmonic effect. Some of the anharmonic effect is associated with the soft mode, the rest is not. In the case where the external variable is the pressure, the variations associated with the anharmonic effect which is not related to the soft mode is expected to be linear. Therefore, the variations in the elastic constant which are strictly associated with the phase transition can be obtained more rigorously. For this reason, the data as a function of pressure is more useful for testing a model.

So far, experimental results about the properties of the elastic constants associated with the soft mode are not consistent. While some experiments [9, 14, 21] show that the elastic constant associated with the strain $e_1 - e_2$, i.e. $(C_{11} - C_{12})/2$, gets softened, other groups [10, 12] observed that C_{66} (associated with e_6) gets softened. Our results indicate that it is elastic constant $(C_{11} - C_{12})/2$ which exhibits incomplete softening at T_c (or P_c). Above T_c (or below P_c), it shows a nonlinear temperature (or pressure) dependence. In contrast, C_{66} shows a small temperature (or pressure) dependence. These results are consistent with a pseudoproper ferroelastic mechanism for the point group symmetry change $4 \rightarrow 2$. The stronger softening of $(C_{11} - C_{12})/2$ can be explained in terms of a stronger coupling with the order parameter of the $e_1 - e_2$ mode.

In order to explain the experimental features observed in this project, we have presented a Landau model involving both temperature and pressure as external parameters. This model is based on the assumption that the observed phase transition has a pseudoproper character. In another word, we suppose that the order parameter for this phase transition is a physical quantity, but not $e_1 - e_2$ or e_6. Unfortunately, present information about this phase transition does not allow us to identify this

physical quantity. However, as far as the expansion of the Landau free energy is concerned, what is relevant is the symmetry of the order symmetry. A Landau model can be developed as long as the symmetry of the order parameter is known. According to group theory, for a $4 \longrightarrow 2$ phase transition the symmetry of the order parameter should have the same symmetry as the strain components $e_1 - e_2$ or e_6. Our model has been derived using this information. Landau models contain adjustable parameters. It should be emphasized that all the parameters used in our model has been fixed in the process of fitting the temperature dependence of the strains and the shift of the transition temperature dT_c/dP. With the same parameters, our model can consistently accounts not only for the temperature dependence of the strains but also for the temperature and pressure dependence of the elastic constants as well. As we have demonstrated, our model can quantitatively describe both the temperature and the pressure behaviors of the elastic constants for the tetragonal phase of $Rb_4LiH_3(SO_4)_4$. In particular, our model describes quite well the pressure behavior of $(C_{11} - C_{12})/2$. For this elastic combination, due to its strong softening, the variations caused by anharmonic effects not related to the soft mode are insignificant. Therefore, any valid model for this phase transition is expected to be able to explain the behavior of this elastic combination even without subtracting any variations. Thus, the good agreement of our model with the experimental results of $(C_{11} - C_{12})/2$ is a strong argument for our model. For the monoclinic phase, due to the fact that the experimental values of the elastic constants are obtained using the equations corresponding to the tetragonal phase and that domains appear, it is no longer possible for us to carry on a quantitative comparison in the low temperature phase. Therefore, the validity of the model in this phase has not been fully proved. Nevertheless, we still see that our model can qualitatively describe the behavior of the elastic constants in this phase. All these evidences show that our model can appropriately describe the properties of

$Rb_4LiH_3(SO_4)_4$. Considering that only the lowest coupling terms are considered in this model, no better agreement is expected.

According to our sound velocity measurements, the acoustic mode associated with the transverse waves propagating along [110] and polarized perpendicularly to the z-axis shows the largest variations in velocity above T_c. However, this mode is not the actual soft acoustic mode accompanying a $4 \rightarrow 2$ transition. The actual soft acoustic mode does not propagate along one of the investigated directions. According to our model, the actual soft acoustic mode should be observed in a direction corresponding to -5^0 relative to the [110] direction. Moreover, in contradiction with the calculation reported by Mróz et al. [14], our model predicts that the effective elastic constant associated with the soft mode shows complete softening at T_c. Our prediction is consistent with our experimental results. To our knowledge, no one has directly investigated the actual soft acoustic mode of $Rb_4LiH_3(SO_4)_4$ using sound waves propagating along the proper direction. Mróz et al. [14] did measure the velocities of transverse phonon propagating along two directions away from [110] by 5 and 9 degree, respectively. Their results show that the softening becomes less pronounced as the angle of deviation is increased. Based on our calculation, we believe that they investigated along the wrong directions. The actual soft acoustic mode can be observed only by turning the investigation direction the other way around.

As mentioned above, velocity measurements using transverse waves propagating along the direction deviating [110] by -5^0 angle should reveal complete acoustic phonon softening at T_c. Thus, a series of measurements in the xy-plane are needed in order to clarify if the soft acoustic soft mode shows complete softening. For this investigation, Brillouin scattering technique is recommended. Using that technique, measurements along different directions can be easily realized.

In order to obtain accurate elastic constants in the monoclinic phase, measure-

ments using single domain crystal are needed. According to Wolejko et al. [9], the single domain crystal can be obtained by applying normal stress along [100] or [010] directions. With the appropriate velocity measurements, the elastic constants in this ferroelastic phase can be derived using Christoffel equations corresponding to the monoclinic phase. Subsequently, the validity of the proposed Landau model could be tested further.

According to group theory, for a $4 \rightarrow 2$ phase transition, the driving mechanism may be the instability of the B symmetry optic mode in the prototype phase 4. In order to determine whether the order parameter for the phase transition observed in this project is identified with a soft Raman mode, further Raman scattering investigations are recommended.

Bibliography

[1] K. Aizu, J. Phys. Soc. Japan **27**, 387 (1969); Ibid. **31**, 802 (1971).

[2] D. L. Fox, J. F. Scott, P. M. Bridenbaugh, Solid State Commun. **18**, 111 (1976).

[3] S. W. Meeks, B. A. Auld, Appli. Phys. Lett. **47**, 102 (1985).

[4] V. K. Wadhawan, Phase Transit. **3**, 3 (1982).

[5] B. Hilczer, M. Polomska, A. Pawlowski, J. Wolak, Ferroelectrics **155**, 177 (1994).

[6] B. Mróz, S. M. Kim, M. Powell, H. Kiefte, R. L. Donaberger, Phys. Rev. B **55**, 11174 (1997).

[7] B. Mróz, R. Laiho, Phys. Stat. sol. (a) **115**, 575 (1989).

[8] J. Minge, T. Krajewski, Phys. Stat. Sol. (a) **109**, 193 (1988).

[9] T. Wolejko, G. Pakulski, Z. Tylczynski, Ferroelectrics **81**, 179 (1988).

[10] B. Mróz, J. A. Tuszyński, H. Kiefte, M. J. Clouter, J. Phys.: Condens. Matter **1**, 4425 (1989).

[11] F. J. ZúŤildeniga, J. Etxebarria, G. Madariaga, T. Breczewski, Acta Cryst. **C 46**, 1199 (1990).

[12] H. Hempel, H. Maack, G. Sorge, Phys. Stat. sol. (a) **110**, 459 (1988).

[13] M. Polomska, F. Smutný, Phys.Stat.Sol. (b) **154**, K103 (1989).

[14] B. Mróz, H. Kiefte, M. J. Clouter, and J. A. Tuszyński, J. Phys.: Condens. Matter **3**, 5673 (1991).

[15] B. Mróz, M. Kaczmarski, H. Kiefte, M. J. Clouter, J. Phys.: Condens. Matter **4**, 7515 (1992).

[16] B. Mróz, H. Kiefte, M. J. Clouter, and J. A. Tuszyński, J. Phys.: Condens. Matter **5**, 6377 (1993).

[17] B. Mróz, H. Kiefte, M. J. Clouter, Ferroelectrics **88**, 105 (1988).

[18] T. Wolejko, P. Piskunowicz, T. Breczewski, T. Krajewski, Ferroelectrics **81**, 175 (1988).

[19] P. Piskunowicz, T. Breczewski, T. Wolejko, Phys. Stat. sol. (a) **114**, 505 (1989).

[20] M. Maeda, H. Tachi, I. Suzuki, Ferroelectrics **155**, 195 (1994).

[21] T. Breczewski, A. Gomez-Cuevas, J. M. Perez-Mato, E. H. Bocanegra, Solid State Commun. **76**, 639 (1990).

[22] S. Mielcarek, Z. Tylczyñski, P. Piskunowicz, B. Mróz, Ferroelectrics **172**, 287 (1995).

[23] A. Pietraszko, K. Lukaszewicz, Z. Krystallogr. **185**, 564 (1988).

[24] P. Tolédano, M. M. Fejer, B. A. Auld, Phys. Rev. B **27**, 5717 (1983).

[25] J. C. Tolédano, P. Tolédano, Phys. Rev. B **21**, 1139 (1980).

[26] J. Sapriel, Phys. Rev. B **12**, 5128 (1975).

[27] R. A. Cowley, Phys. Rev. B **13**, 4877 (1976).

[28] A. M. Balagurov, N. C. Popa, B. N. Savenko, Phys. Stat. Sol. (b) **134**, 457 (1986).

[29] J. Baran, M. K. Marchewska, H. Ratajczak, Z. Czapla, J. Mol. Struct. **436-437**, 281 (1997).

[30] G. Errandonea, Phys. Rev. B **21**, 5221 (1980).

[31] W. I. F. David, Mater. Res. Bull. **18**, 809 (1983).

[32] N. Boccara, Ann. Phys. **47**, 40 (1968).

[33] G. Quirion, M. Abu-Kharma, I. A. Sergienko, M. Bromberek, M. J. Clouter, B. Mr'oz, J. Phy.: Condens. Matter **15**, 4979 (2003).

[34] Yu. M. Gufan, I. A. Sergienko, O. V. Krivitskii, L. A. Shuvalov, Crystallography Reports **42**, 525 (1997).

[35] J. Baran, T. LIS, P. Starynowicz, J. Mol. Struct. **213**, 51 (1989).

[36] A. Sawada, M. Udagawa, T. Nakamura, Phys. Rev. lett. **39**, 829 (1977).

[37] J. L. Birman, Phys. Rev. lett. **17**, 1216 (1966).

[38] M. Wada, Y. Nakayama, A. Sawada, J. Phys. Soc. Japan **47**, 1575 (1979).

[39] T. Sekine, M. Takayama, K. Uchinokura, E. Matsuura, J. Phys. Soc. Japan **55**, 3903 (1986).

[40] A. Pinczuk, G. Burns, F. H. Dacol, Solid State Commun. **24**, 163 (1977).

[41] E. Sarantopoulou, Y. S. Raptis, E. Zouboulis, C. Raptis, Phys. Rev. B **59**, 4154 (1999).

[42] B. Mróz, H. Kiefte, M. J. Clouter, J. A. Tuszyński, Phys. Rev. B **36**, 3745 (1987).

[43] C. Raptis, R. L. McGreevy, Phys. Rev. B **43**, 12668 (1991).

[44] B. Lorenz, A. P. Litvinchuk, M. M. Grospodinav, C. W. Chu, Phys. Rev. Lett. **92**, 087204-1 (2004).

[45] Ch. Hahn, H.-G. Unruh, Phys. Rev. B **43**, 12665 (1991).

[46] C. Raptis, R. L. McGreevy, D. G. Seguier, Phys. Rev. B **39**, 7996 (1989).

[47] M. Hidaka, H. Fujii, S. Yamashita, Phase Transit. **58**, 247 (1996).

[48] S. Tsunekawa, A. Kasuya, Y. Nishina, T. Fukuda, Materials Transactions, JIM **37**, 650 (1996).

[49] L. Jian, C.M. Wayman, J. Am. Ceram. Soc. **80**, 803 (1997).

[50] S. Tsunekawa, A. Kasuya, Y. Nishina, Materials Science and Engineering A **217**, 215 (1996).

[51] O. N. Fedorova, V. I. Strakhov, Russian Journal of Inorganic Chemistry **41**, 808 (1996).

[52] F. Willis, R. G. Leisure, T. Kanashiro, Phys. Rev. B **54**, 9077 (1996).

[53] J. Witting, A. Eichler, and Z. Angew, Physica **25**, 319 (1968).

[54] G. Errandonea and H. Savary, Phys. Rev. B **24**, 1292 (1981).

[55] S. Dorfman, D. Fuks, A. Gordon, A. V. Postnikov, G. Borstel, Phys. Rev. B **52**, 7135 (1995).

[56] A. Gordon, S. Dorfman, Phys. Rev. B **50**, 13132 (1994).

[57] M. M. Marchewka, J. Baran, Spectrochimica Acta Part A **60**, 201 (2004).

[58] M. Polomska, B. Hilczer, J. Wolak, Acta Physica Polonica **85**, 825 (1994).

[59] V. K. Wadhawan, *Introduction to Ferroic Materials* (Gordon and Breach Science Publishers, 2000).

[60] E. Dieulesaint, D. Royer, *Elastic Waves in Solids* (John Wiley and Sons Ltd., Chechister, 1980).

[61] C. Kittel, *Introduction to Solid State Physics* (John Wiley and Sons, New York, 1996).

[62] M. Tinkham, *Group Theory and Quantum Mechanics* (McGraw-Hill Book Company, 1964).

[63] C. N. Rao and K. J. Rao, *Phase Transition in Solids* (Mc Graw-Hill, New York, 1978).

[64] A. D. Bruce and R. A. Cowley, *Structural Phase Transition* (Taylor and Francis Ltd, London, 1981).

[65] J. C. Tolédanno, P. Tolédano, *The Landau Theory of Phase Transition* (World Scientific Publishing Co. Pte. Ltd., 1987).

[66] L. E. Reichl, *A Modern Course in Statistical Physics* (Jhon Wiley and Sons, Inc., 1998).

[67] M. Abu-Kharma, *Investigation of the Elastic Properties of $LiKSO_4$ Single Crystals as a Function of Temperature and Pressure* (M.Sc thesis, Physics Depart. of MUN, 2002).